SPATIAL ANALYSIS OF CHANNEL-BELT STACKING PATTERNS: METRICS TO DISCRIMINATE BETWEEN LOCAL AND REGIONAL CONTROLS ON DEPOSITION IN THE FLUVIAL JOHN HENRY MEMBER OF THE STRAIGHT CLIFFS FORMATION, SOUTHERN UTAH

by

Wassim Benhallam

A thesis submitted to the faculty of
The University of Utah
in partial fulfillment of the requirements for the degree of

Master of Science

in

Geology

Department of Geology and Geophysics

The University of Utah

August 2015

The University of Utah Graduate School

STATEMENT OF THESIS APPROVAL

The thesis of **Wassim Benhallam**

has been approved by the following supervisory committee members:

Lisa Stright	, Chair	**4/27/2015** Date Approved
Cari Johnson	, Member	**4/27/2015** Date Approved
Lauren Birgenheier	, Member	**4/27/2015** Date Approved

and by **John M. Bartley** , Chair/Dean of

the Department/College/School of **Geology and Geophysics**

and by David B. Kieda, Dean of The Graduate School.

ABSTRACT

The John Henry Member (JHM) of the Straight Cliffs Formation exposed along the Kaiparowits Plateau provides a record of ~5 my of coastal plain to marginal marine deposition. To better understand the mechanisms influencing the alluvial architecture of the fluvial JHM, a detailed quantitative characterization of the stratigraphic organization and stacking patterns of fluvial channel-belt sandstone bodies is performed. To this end, point pattern analysis techniques were applied on three datasets consisting of 136, 228, and 55 channel-belts collected from two fluvial outcrops in Bull Canyon and one fluvial outcrop in Rock House Cove, located 18 km to the west of Bull Canyon.

The results reveal two major trends in the spatial organization of channel-belts through time starting with (1) a trend of decreasing clustering and increasing regularity from the lower to middle stratigraphic interval followed by (2) a trend of increasing channel-belt clustering in the upper interval. Furthermore, up-section changes in channel-belt clustering exhibit strong similarities across the three outcrops as indicated by a correlation analysis based on dynamic time warping. Changes in channel-belt stacking patterns are interpreted to be primarily the product of changing basin boundary conditions given the existence of consistent clustering trends in Bull Canyon and Rock House Cove.

Correlation of clustering trends with previously measured architectural parameters and reconstructed paleo-hydraulic conditions suggest significant channel-belt clustering likely reflects the combined influence of three major factors. These include low

aggradation rates driven by reduced accommodation, high avulsion frequency where channels are influenced by backwater hydraulics, and deposition downstream of a nodal avulsion point.

A scale-dependent clustering analysis using the K-function indicates channel-belts are clustered at small length scales, and uniform at larger length scales. The existence of different patterns at different length scales suggests the governing depositional processes operated at different scales. Small-scale clustering is interpreted to be the product of autogenic avulsion reoccupation, where abandoned channels that are preserved as topographic lows served as attractors to new avulsion paths and led to channel persistence. Conversely, the large-scale uniformity reflects periodic large-scale shifts in the local depo-center as a result of subsidence-controlled compensational stacking.

TABLE OF CONTENTS

INTRODUCTION

In its most basic form, fluvial architecture refers to the spatial interplay between channel deposits and floodplain fines. Architectural parameters such as density, connectivity, and overall stacking patterns of channel sandstone bodies are of particular importance to reservoir geologists and hydrologists because they impact fluid flow in subsurface fluvial deposits (Miall, 2014). Alluvial architecture is generally understood to be the product of a combination of allogenic and autogenic processes. Allogenic variables such as sea level, tectonics, and climate have long been viewed as primary controls on alluvial architecture through alterations of the depositional mass balance (i.e., distribution of deposits) within the fluvial system (Shanley and McCabe, 1994; Paola, 2005; Postma, 2014). The interplay of these processes also controls the aggradation rate, which has a major impact on sand body connectivity and stacking patterns according to numerical models (Leeder, 1979). Conversely, more recent research on the role that autogenic processes play in controlling alluvial architecture highlight the importance of internal fluvial processes like avulsion, channel reoccupation, lateral migration, and bifurcation (Jones and Schumm, 1999; Jerolmack and Paola, 2007; Hajek et al., 2010). Many of these autogenic processes can create self-organized patterns that are not mandated by any changing external controls (Jerolmack and Paola, 2007; Hajek et al., 2010).

Due to limitations inherent to studying ancient successions or observing modern processes, workers often rely on numerical and experimental modeling in order to infer

the autogenic fluvial processes responsible for these patterns. For example, although we can observe avulsion processes in modern rivers, avulsions have characteristic recurrence intervals ranging from 10s to 1000s of years, thereby limiting the amount of knowledge we can obtain from direct observation (Rannie et al., 1989; Tornqvist, 1994; van Gelder et al., 1994; Mohrig et al., 2000). Conversely, ancient successions are valuable in displaying patterns generated by autogenic processes over long time scales but often lack detailed information about flow dynamics. These limitations reinforce the role of numerical and experimental models as alternative means of understanding the internal dynamics of autogenic processes like avulsion, their interaction with changing basin boundary conditions, and the combined influence of autogenic and allogenic processes on alluvial architecture (Hooke and Rohrer, 1979; Mohrig et al., 2000).

Many of these modelling efforts focus on the major autogenic and allogenic variables controlling alluvial architecture. These efforts started with the Leeder-Allen-Bridge (LAB) quantitative models of alluvial stratigraphy with the goal of understanding the geometry of channel-belt sandstone bodies and their spatial distribution (Allen, 1978; Leeder, 1978; Bridge and Leeder, 1979). These models suggest that the spatial distribution of channel-belt sandstone bodies in a fluvial succession is primarily controlled by avulsion frequency and sedimentation rate. The models also highlight the architectural influence of other factors such as channel dimensions, compaction, avulsion style, and width of the channel-belt relative to the width of the alluvial plain (Leeder, 1978; Heller and Paola, 1996). The most consequential result of these models is the inverse relationship between sedimentation rate and stacking density (Leeder, 1978; Allen, 1979; Bridge and Leeder, 1979). In other words, periods of low

sedimentation/aggradation allow avulsing channel deposits to stack more densely while higher sedimentation rates tend to isolate sandstone bodies from each other due to thicker intervening floodplain deposits (Heller and Paola, 1996). This relationship was later incorporated into many continental sequence stratigraphic models in which channel-belt stacking patterns are either governed by valley-incision and filling due to base level fluctuations (Shanley and McCabe, 1993; Wright and Marriott, 1993) or by changes in the balance of accommodation to sediment supply due to hinterland tectonics (Little, 1997).

However, one major shortcoming of the early LAB models is the decoupling between avulsion frequency and sedimentation rates, i.e., the assumption that avulsion frequency is a constant that is not affected by changes in sedimentation rates. Observations from modern rivers indicate that avulsion is triggered by the local super-elevation of a channel complex above its floodplain (Wells and Dorr, 1987; Richards et al., 1993). This local super-elevation takes place when sedimentation rates are higher in the active channel than farther within the floodplain, which suggests an intrinsic relationship between avulsion frequency and sedimentation. Experimental models have shown that the rate at which avulsion frequency increases with aggradation rate can occasionally result in a positive relationship between channel-belt stacking density and aggradation rate, contrary to predictions of the early LAB models (Bryant et al., 1995; Heller and Paola, 1996). Data from ancient sedimentary successions have also shown that aggradation rates are not always negatively related to channel-belt stacking patterns (Colombera et al., 2015).

Beyond avulsion frequency, the position of the newly relocated channel-belt in

the floodplain (i.e., following avulsion) can also impact the distribution of channel sandstone bodies. The early LAB models assumed avulsion paths are always confined to topographically low areas of the floodplain away from alluvial ridges created by former channels (Allen, 1978; Bridge and Leeder, 1979; Mackey and Bridge, 1995). These ridges act as barriers to flow until they are buried by floodplain sedimentation. This tendency for channelized systems to preferentially fill topographic lows is often termed compensational stacking. Statistical analysis of stratigraphy generated by numerical models simulating compensational stacking reveals sandstone bodies are regularly spaced/distributed (Flood and Hampson, in review).

However, observations of modern avulsions suggest that recently-abandoned channels do not necessarily form alluvial ridges, but can also act as attractors – instead of barriers – to new river flows (Aslan and Blum, 1999; Morozova and Smith, 2000; Hofmann et al., 2011). Theoretical and experimental work suggests abandoned channels favor avulsion reoccupation because their beds are preserved as lows on the floodplain (Jerolmack and Paola, 2007; Mohrig et al., 2000). Numerical models have also shown that channel reoccupation can influence the alluvial architecture over both small and large scales. Over small scales, cellular models where abandoned channels serve as attractors favor the development of multistory sandstone bodies. Over longer time scales, multiple avulsion-reoccupation events can result in a clustered distribution of channel sandstone bodies (Jerolmack and Paola, 2007).

One key result from all of these models is that pre-existing topography exercises far more influence on channel stacking patterns than traditionally appreciated. To better understand this influence, many workers focused on characterizing these patterns by

quantifying the degree of clustering, compensation, or randomness in the spatial distribution of channel sandstone bodies both in outcrop and synthetic stratigraphy. Hajek et al. (2010) were among the first to use statistical algorithms to assess the degree of clustering of channel sandstone bodies in a fluvial succession. This study extends Hajek et al. (2010) by using a comprehensive and customized suite of statistical algorithms and techniques to characterize the distribution, proportion, and geometry of alluvial deposits as well as the 2D arrangement of architectural elements within the fluvial John Henry Member (JHM) of the Straight Cliffs Formation (SCF). The fluvial JHM is particularly well suited for a detailed quantitative characterization of alluvial architecture due to nearly continuous exposures of fluvial strata along the southern edge of the Kaiparowits Plateau.

Previous work performed in the fluvial JHM includes a quantitative characterization of the alluvial architecture. This includes measurements of channel-belt dimensions, channel-belt vertical and lateral amalgamation, net-to-gross (NTG), grain size, and D50 bedload (Gooley, 2010; Pettinga, 2012). These measurements, together with facies descriptions, were used to define seven depositional units with distinct alluvial architecture. These units were also grouped into two stratigraphic intervals representing large scale trends in alluvial architecture. The lower to middle interval is characterized by a fining-upward trend associated with decreasing NTG, channel-belt width, thickness, and amalgamation. The middle JHM shows laterally restricted and isolated channel-belts embedded in thick floodplain deposits. Finally, the middle to upper interval shows increasing grain size, NTG, channel-belt dimensions and amalgamation. Changes in alluvial architecture have qualitatively been attributed to changing basin

boundary conditions, primarily driven by the interaction of accommodation and sediment supply due to tectonic activity (Gooley, 2010; Pettinga, 2012; Szwarc et al., 2014).

While previously documented channel-belt parameters are useful in identifying some of the large-scale trends in alluvial architecture, they do not reflect the true distribution and stratigraphic arrangement of channel-belts. This can lead to over-simplified trends in alluvial architecture that may fail to describe the real dynamic processes that are at work in these fluvial fan systems. To address this limitation, we use customized point pattern analysis to analyze the stacking patterns of channel-belts observed in three different outcrops (Bull Canyon West, Bull Canyon East, and Rock House Cove) within the proximal fluvial John Henry Member (Figure 1). The study also sets out to analyze whether there are any persistent up-section trends in the stratigraphic arrangement of channel-belts and whether these trends are consistent with previously identified qualitative large-scale trends of alluvial architecture (Gooley, 2010; Pettinga, 2012; Turner, 2014). The presence of consistent architectural trends in these three outcrops – or lack thereof – can provide valuable insights into the scales of processes controlling deposition and hence help constrain their nature (i.e., autogenic vs allogenic).

Figure 1 – Map of Kaiparowits Plateau in southern Utah. Exposures of the Straight Cliffs Formation are shown in shaded gray. Black squares indicate locations of the three outcrops selected for the analysis. Two outcrops (Bull Canyon west and east) are located in Bull Canyon and one outcrop (Rock House Cove west) is located in Rock House Cove. Black dots show locations of previous studies (modified from Szwarc et al., 2014).

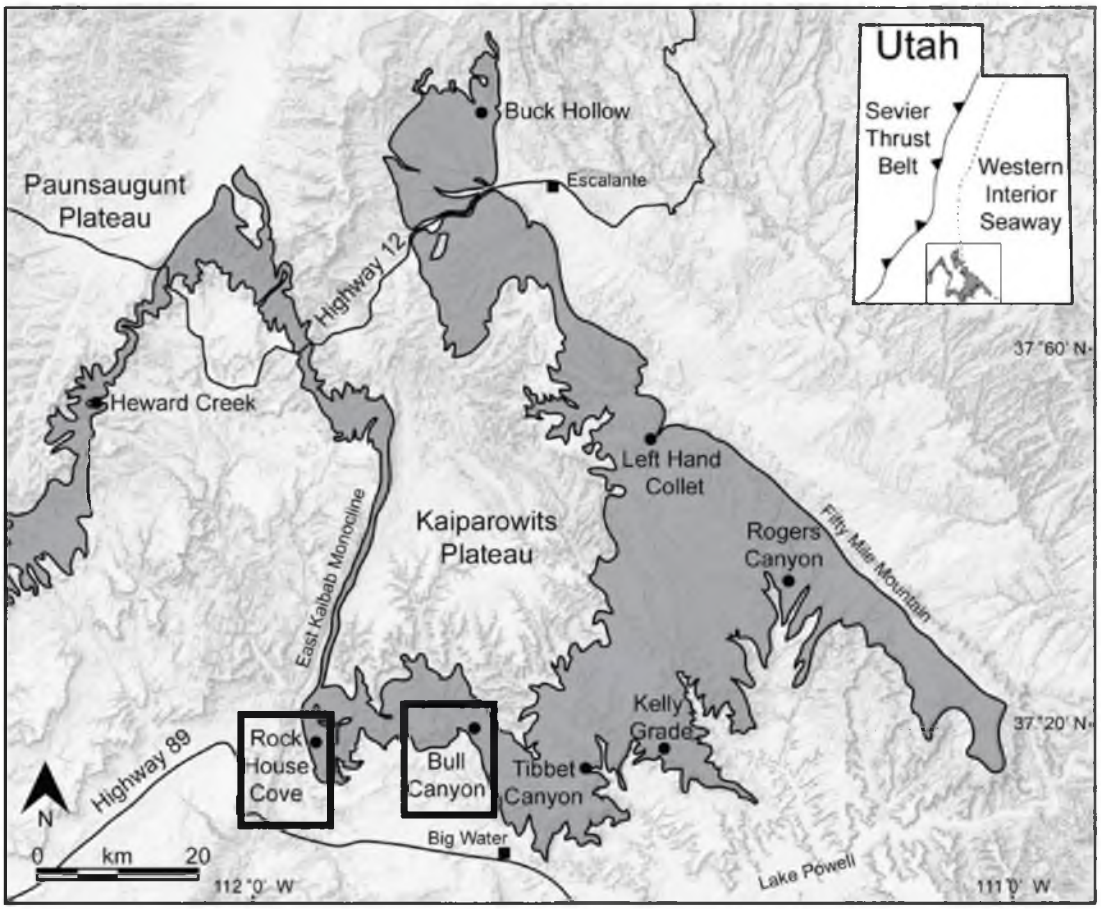
Utah
Sevier Thrust Belt
Western Interior Seaway
Buck Hollow
Escalante
Paunsaugunt Plateau
Highway 12
Heward Creek
Left Hand Collet
Kaiparowits Plateau
East Kaibab Monocline
Rogers Canyon
Fifty Mile Mountain
Kelly Grade
Rock House Cove
Bull Canyon
Tibbet Canyon
Highway 89
Big Water
Lake Powell
N
0 km 20
112 °0' W
111 °0' W
37 °60' N
37 °20' N

REGIONAL GEOLOGY

Straight Cliffs Formation

The Straight Cliffs Formation was deposited during Late Cretaceous time in a retro-arc foreland basin setting along the western margin of the Western Interior Seaway. The foreland basin developed in response to flexural subsidence due to crustal loading by the Sevier fold-thrust belt as well as dynamic mantle-driven subsidence (Jordan, 1981; Liu et al., 2014). The thrust belt formed as a result of east-west crustal shortening driven by the subduction of the Farallon plate beneath the western margin of the North American plate from Jurassic to Eocene time (Armstrong, 1968; Coney, 1972; Dickinson, 1974; DeCelles and Coogan, 2006). During the mid- to Late Cretaceous, high eustatic sea levels associated with greenhouse conditions allowed waters from the Arctic Ocean and the Gulf of Mexico to flood the basin and form the Cretaceous Western Interior Seaway (Kauffman, 1977; Hancock and Kauffman, 1979; Haq et al., 1987; Miller et al., 2005).

The Straight Cliffs Formation is 300 to 500 m thick and is well exposed throughout the Kaiparowits Plateau, which is located in the Grand Staircase-Escalante National Monument of south-central Utah (Figure 1). Early stratigraphic work divided the formation into four members (Figure 2) which are – from oldest to youngest – Tibbet Canyon Member, Smoky Hollow Member, John Henry Member, and lastly, the Drip Tank Member (Peterson, 1969b). Initially known as the lower sandstone member of the Straight Cliffs Formation, the Tibbet Canyon Member consists of about ~30 m of shallow

marine sandstone and siltstone deposits that record the earliest northeastward regression of the Western Interior Seaway. This member is overlain by about ~30 m of interbedded sandstone beds, mudstone beds, and coals of the Smoky Hollow Member that record coastal plain deposition (Peterson, 1969b). The Smoky Hollow Member is capped by the Calico bed, a coarse-grained white braided gravel sheet that records deposition in reduced accommodation. Overlying the Smoky Hollow Member is the John Henry Member which consists of about ~300 m of cliff-forming sandstone beds interbedded with slope-forming mudstone beds and coals. The John Henry Member also displays great lateral variability as it records a transition from continental deposits in the southern and western Kaiparowits Plateau to marginal marine deposits in the eastern plateau (Peterson, 1969a; McCabe et al., 1988; Shanley, 1991; Shanley and McCabe, 1991, 1993, 1994, 1995; Shanley et al., 1992; Hettinger et al., 1993; Gallin et al., 2010; Gooley, 2010; Pettinga, 2012; Turner, 2014). Finally, the uppermost Drip Tank Member consists of about 30 to 100 m of cliff-forming coarse-grained fluvial sandstones (Peterson, 1969b).

Regional Sediment Provenance

Recent results of sediment provenance studies using detrital zircon U-Pb geochronologic data suggest fluvial strata of the Straight Cliffs Formation were deposited by a northeast-flowing axial fluvial system (Figure 3) fed by transverse distributive fluvial systems draining three main source areas: (1) the Mogollon highlands to the southwest, (2) the Sevier fold-thrust belt to the west, and (3) the Cordilleran magmatic arc to the southwest (Eaton, 1991; Hettinger et al., 1993; Lawton et al., 2003; Szwarc et al., 2014). These findings are also consistent with the NNE-trending shoreline-parallel compound incised valley system interpreted in the lower JHM in Main Canyon (Chentnik

et al., in press). Additionally, stratigraphic thickening of the John Henry Member in Buck Hollow – located north of Main Canyon (Figure 1) – also supports the interpretation of an axial north-east flowing fluvial system (Mulhern et al., 2014).

Fluvial Architectural Trends

The stratigraphic architecture of the proximal fluvial JHM was primarily investigated in Rock House Cove and Bull Canyon with the goal of identifying controls on deposition (Gooley, 2010; Pettinga, 2012). Gooley (2010) and Pettinga (2012) divided the fluvial JHM into seven depositional units, named DU-0 through DU-6, based on lithofacies descriptions and measurements of channel-belt dimensions, amalgamation and NTG (Figure 4). The resulting depositional units reflect regional intervals comprised of a distinctive arrangement of facies associations.

The lowermost depositional unit, DU-0, is 10 to 20 m thick and forms a prominent cliff that overlies the coarse-grained sandstones or the floodplain fines of the Calico Bed of the Smoky Hollow Member. The unit contains thick and laterally extensive channel-belts consisting of coarse grain sandstones with many macroform accretion sets indicating both downstream and lateral accretion (Gooley, 2010; Pettinga, 2012). Channel-belts of this unit are also highly laterally and vertically amalgamated. Overbank fines are generally not preserved in this unit as indicated by the high NTG (0.9) (Figure 4).

DU-1 is 10 to 30 m thick and consists of laterally isolated single story fluvial channels. Channel-belts are thin (<2 m) and show little vertical and lateral amalgamation. Overbank fines are commonly interbedded with coal mire facies. The unit is also characterized by the presence of numerous indicators of flow fluctuations including

rhythmically laminated flaser, wavy, and lenticular bedding (Gooley, 2010; Pettinga, 2012).

DU-2 is 15 to 20 m thick, has a medium NTG (0.58), and consists of a number of back-stepping 6m thick ledges separated by slope forming overbank deposits. Channel-belts are isolated and laterally restricted with low vertical and lateral amalgamation and generally consist of planar, trough, and ripple cross-laminated sandstone (Gooley, 2010; Pettinga, 2012).

DU-3 is 40 m thick and is characterized by the lowest NTG (0.3), least degree of channel amalgamation, and highest proportion of coal deposits of any depositional unit in the succession. Channel-belts are thin (<2 m), single story, laterally isolated, and consist of trough-cross stratified medium-grained sandstone (Gooley, 2010; Pettinga, 2012).

DU-4 varies in thickness from 40 m in Rock House Cove to 70 m in Bull Canyon and has a medium NTG (0.42). Channel-belts are on average 3 to 4 m thick, can be laterally restricted or laterally extensive, and are moderately amalgamated. Channel-belts consist of trough-cross stratified, ripple laminated, and planar laminated sandstone (Gooley, 2010; Pettinga, 2012).

DU-5 is 30 to 50 m thick and has a medium NTG (0.5). Floodplain deposits consist of yellow to light olive gray massive siltstones. Channel-belts consist of coarse sandstones that increase vertically in grain size and in abundance of gravel lags. Channel-belts are laterally and vertically amalgamated into channel-belt complexes, and contain accretion sets that indicate dominant lateral accretion (Gooley, 2010; Pettinga, 2012).

Finally, DU-6 consists of a 10 to 25 m thick cliff-forming sandstone that is composed of medium grains through gravel-sized clasts. Sandstone bodies show trough

cross-stratification and low-angle bedding. Very high lateral and vertical amalgamation produced a sheet-like appearance to this unit, which is also characterized by the presence of numerous internal scour surfaces that crosscut each other (Gooley, 2010; Pettinga, 2012).

In both study areas (Bull Canyon and Rock House Cove), two large-scale trends were identified: (1) an upward-decrease in grain size, NTG, channel-belt dimensions and amalgamation from DU-0 to DU-3, and (2) a reversed trend of increasing grain size, NTG, channel-belt dimensions and amalgamation from DU-4 to DU-6 (Figure 4). A paleomorphodynamic workflow was also employed to estimate several morphological parameters such as bankfull depth and sinuosity, as well as formative hydraulic conditions including bankfull discharge and slope (Turner, 2014). In particular, the architecture and geometry of channel-belts in the lower JHM of Bull Canyon was related to the influence of backwater hydraulic effects (Turner, 2014).

Controls on Depositional Architecture

To understand the controls on these different architectural patterns, Shanley and McCabe (1993) attempted to correlate sequence stratigraphic surfaces they observed in marginal marine deposits to terrestrial strata. This correlation led to the development of a frequently-cited sequence stratigraphic framework for strata in the Kaiparowits Plateau that links changes in alluvial architecture to valley incision and filling driven by base level fluctuations. However, more recent correlations of fluvial to paralic to marginal marine strata have exposed numerous practical limitations to this model, the most important of which is the lack of evidence for an incised valley in many locations spanning the fluvial, paralic, and marginal marine JHM (Allen and Johnson, 2010; Gallin

et al., 2010; Pettinga, 2012).

Given the limitations of the eustatic model, other authors suggested that changes in accommodation relative to sediment supply due to tectonic activity in the hinterland were primary drivers of alluvial architecture (Little, 1997). More recent studies in the proximal fluvial JHM also stress the importance of episodic tectonic activity in controlling alluvial architecture but still acknowledge the potential influence of base level change (Allen and Johnson, 2011; Pettinga, 2012; Szwarc et al., 2014).

Despite differences regarding the exact combination of processes controlling architecture, previous studies overwhelmingly favor changing basin boundary conditions as drivers of architecture and pay little attention to how these conditions interact with autogenic variability. To correct this bias, this study investigates the role of autogenic processes in shaping alluvial architecture and explores how formative autogenic dynamics (i.e., compensation, avulsion reoccupation) interact with externally-controlled signals to impact architecture.

Figure 2 – Regional stratigraphic framework of the Straight Cliffs Formation showing previously documented architectural trends in fluvial strata (Rock House Cove and Bull Canyon), paralic strata (Kelly Grade), and marginal marine strata (Rogers Canyon and Left Hand Collet) (modified from Szwarc et al., 2014).

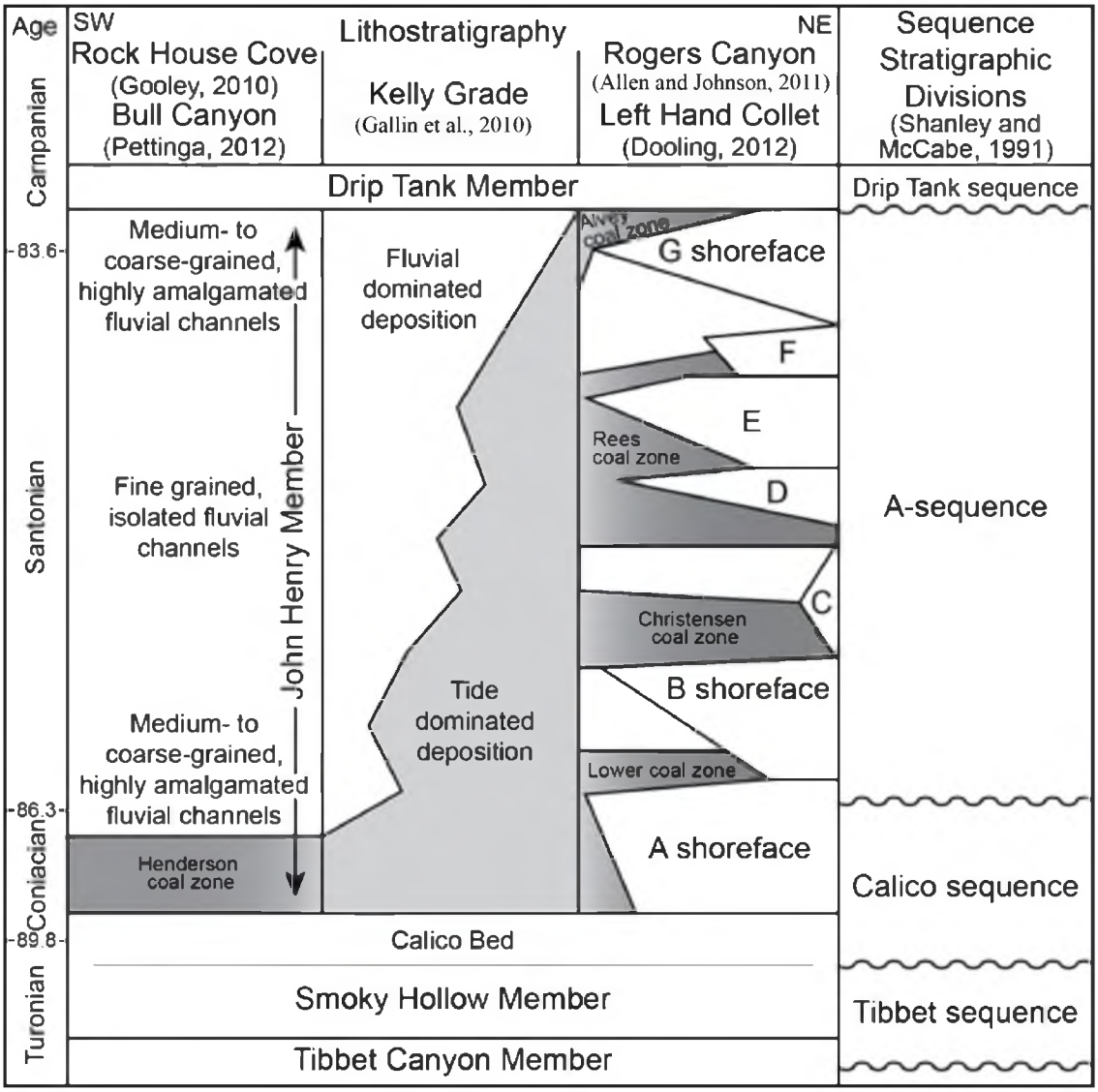
Age
SW
Rock House Cove
(Gooley, 2010)
Bull Canyon
(Pettinga, 2012)
Lithostratigraphy
Kelly Grade
(Gallin et al., 2010)
NE
Rogers Canyon
(Allen and Johnson, 2011)
Left Hand Collet
(Dooling, 2012)
Sequence Stratigraphic Divisions
(Shanley and McCabe, 1991)
Campanian
Drip Tank Member
Drip Tank sequence
-83.6-
Santonian
Medium- to coarse-grained, highly amalgamated fluvial channels
Fine grained, isolated fluvial channels
Medium- to coarse-grained, highly amalgamated fluvial channels
John Henry Member
Fluvial dominated deposition
Tide dominated deposition
Allen coal zone
G shoreface
F
E
Rees coal zone
D
C
Christensen coal zone
B shoreface
Lower coal zone
A shoreface
A-sequence
-86.3-
Coniacian
Henderson coal zone
Calico sequence
-89.8-
Turonian
Calico Bed
Smoky Hollow Member
Tibbet sequence
Tibbet Canyon Member

Figure 3 – Paleogeographic reconstruction of the axial fluvial system flowing northeast through the Kaiparowits basin during Santonian time. The axial system is fed by distributive fluvial systems draining three source areas: (1) MH: Mogollon highlands, (2) STB: Sevier thrust belt, and (3) CMA: Cordilleran magmatic arc (modified from Szwarc et al., 2014).

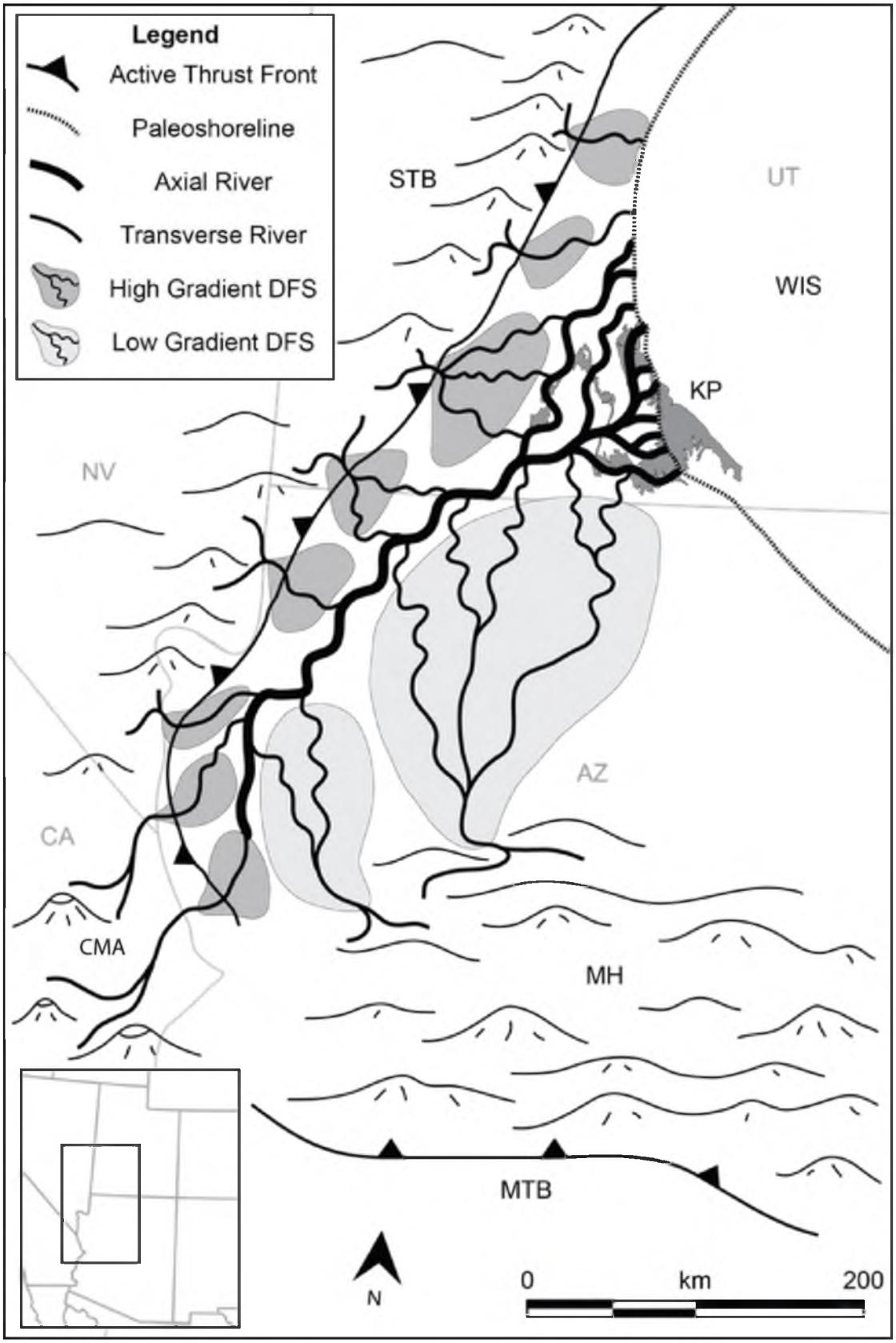
Legend
Active Thrust Front
Paleoshoreline
Axial River
Transverse River
High Gradient DFS
Low Gradient DFS
STB
UT
WIS
KP
NV
AZ
CA
CMA
MH
MTB
N
0
km
200

Figure 4 – Trends in several previously documented architectural parameters including NTG, D50 bedload, channel-belt dimensions, and lateral amalgamation of channel-belt (data from Pettinga, 2012).

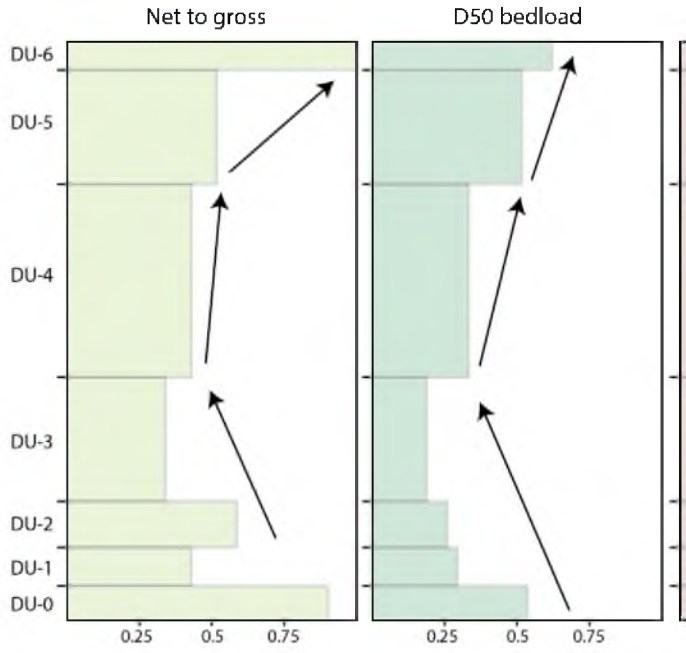
Net to gross
D50 bedload
DU-6
DU-5
DU-4
DU-3
DU-2
DU-1
DU-0
0.25
0.5
0.75
0.25
0.5
0.75

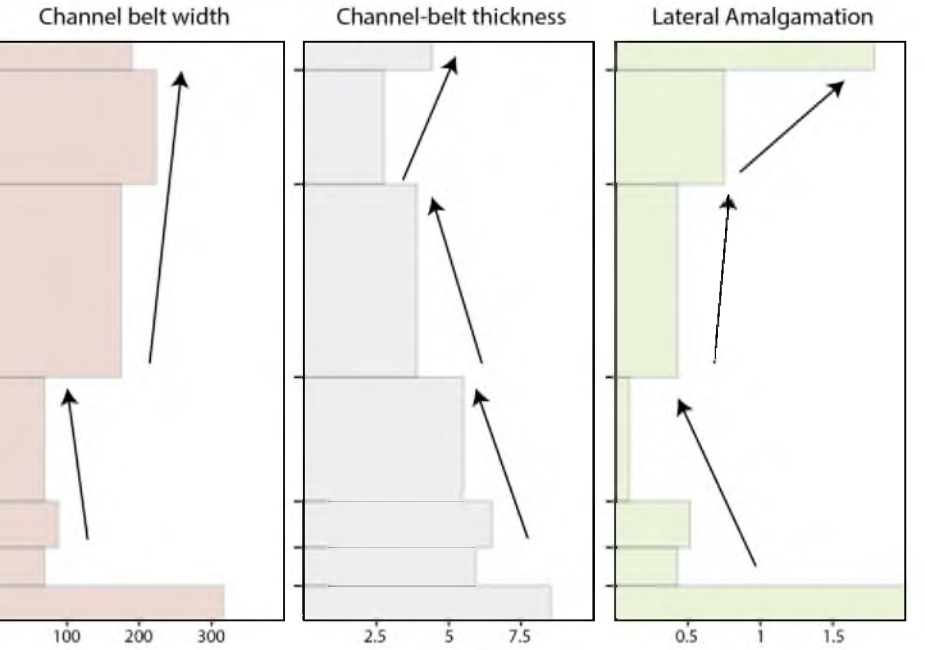
Channel belt width
Channel-belt thickness
Lateral Amalgamation
100
200
300
2.5
5
7.5
0.5
1
1.5

METHODS

Three different point pattern analysis techniques were used to characterize the 2D arrangement of channel-belts within the fluvial John Henry Member of the Straight Cliffs Formation. These techniques are applied on three different outcrops: (1) northwest Rock House Cove, (2) east Bull Canyon, and (3) west Bull Canyon. Each dataset consists of 2D coordinates of channel-belt center points. The data collection and processing methods are discussed below.

Data Collection

A differential GPS receiver paired with a laser ranger finder was used to document the geometry, dimensions, and distribution of channel-belts observed in outcrop guided by interpreted gigapans (Figure 5 and Figure 6). The receiver (Trimble GeoExplorer 6000 GPS unit equipped with a Tempest antenna) was moved parallel to the outcrop face to maximize visibility and cover the full lateral extent of the sandstone bodies, ensuring it was no farther than 700-800m from the outcrop at each scanning location. GPS points were recorded as offsets from the receiver using a TruPulse 306b range finder. Two GPS points were collected at the furthest lateral extents of each channel-belt to document its apparent width while a pair of vertically-aligned GPS points (i.e., base and top of sand body) was collected to document its maximum thickness. In some cases, more than one pair of vertically-aligned GPS points were collected to capture thickness variations.

Postprocessing Corrections

To improve the accuracy of the collected GPS positions, a base station located in Page, Arizona was used to determine GPS measurement errors and compute corrections to these errors. This correction was performed during post-processing using the GPS Pathfinder Office software suite. The corrected GPS points were then loaded into Petrel and corrected for minor structural dip. Apparent channel-belt widths were also corrected to true channel-belt widths because outcrop orientation is often oblique to paleocurrent direction. An average paleocurrent per depositional unit was used together with the outcrop orientation to solve for the true channel-belt width using the approach described by Fabuel-Rerez et al. (2009).

Channel-belt Projections

Point pattern analysis techniques quantify the spatial distribution of points. Therefore, the irregular 2D shapes of outcropping channel-belt sandstone bodies were reduced to 1D by interpreting channel-belts centerpoints. A centerpoint is calculated for each channel-belt by averaging the coordinates of its lateral GPS points (Figure 7). Finally, these channel-belt center points are projected on a plane perpendicular to the average overall paleocurrent direction to characterize their spatial organization as seen in a cross-section normal to the down-valley direction (Figure 7). The center points are also projected on a plane parallel to outcrop orientation to understand how plane orientation affects the resulting spatial classification. The projected center points are then used as the input dataset to the different point pattern analysis techniques.

Point Pattern Analysis Techniques

Point pattern analysis (PPA) is a branch of spatial statistics concerned with characterizing the spatial organization of a point pattern, usually in 2D space. A point pattern simply refers to the locations (i.e., x-z coordinates) of a set of points within a finite sample region. In our case, the points represent the channel-belt center points while the sample region refers to the outcrop face. The spatial organization of the channel-belt point pattern (PP) is analyzed by quantifying its departure from spatial randomness and is classified as one of three general patterns (Figure 8):

- Random: all points have an equal probability to be located anywhere within the domain area, and the location of every point is independent from the locations of neighboring points.
- Uniform: every point is regularly spaced from neighboring points.
- Clustered: consists of several dense congregations of points separated from one another by large areas with few, if any, points.

To classify a point pattern, PPA techniques rely on a statistical model of randomness against which a point pattern is compared. A point pattern is therefore said to be random if it satisfies the fundamental hypothesis of complete spatial randomness (CSR hypothesis). The CSR hypothesis is defined by two basic principles (Diggle, 2003):

- Given a randomly generated point process with a known intensity parameter, the number of events (i.e., points) within region A is Poisson distributed. This means that the number of points within subregions {A1, A2, …, Ak} of A are independent random variables
- The expected number of points within region A only depends on its area and the

intensity of the point process, not on the specific shape or location of region A.

Quadrat Method

Given a pattern of channel-belt centerpoints confined within a region R (i.e., outcrop face), the quadrat method partitions the region R into m congruent and equal-sized subregions $Qi: i = 1, \dots, m$, called quadrats (Cressie, 1993; Diggle, 2003; Figure 8). Under the CSR hypothesis, the point-count distribution for a region R follows a Poisson distribution with an expected point density:

$$D = \frac{n}{area(R)} \tag{1}$$

where D is the expected point density in region R, n is the total number of points in region R, and $area(R)$ is the total area of region R.

The CSR hypothesis asserts that the point-counts (PC) within all quadrats of region R $PC(Qi), i = 1, \dots, m$ are independent random samples from the Poisson distribution. To test this prediction, the quadrat method uses the Pearson X^2 goodness-of-fit to test whether point-counts are truly Poisson distributed (Smith, 2014). Appendix B illustrates how the X^2 statistic reduces to the ratio $\frac{s^2}{\bar{n}}$ where s^2 is the variance in quadrat point-counts and $\bar{n}$ is the mean quadrat point-count. Hence, the ratio of variance over mean can be used to discriminate between clustering and dispersion (Figure 8) as follows:

- $\frac{s^2}{\bar{n}} = 1$. Under CSR, the variance of a Poisson distribution is exactly its mean, thus a ratio of 1 indicates the point pattern is random.
- $\frac{s^2}{\bar{n}} > 1$. There is more variation in quadrat point-counts than is expected from a random pattern, suggesting the pattern is clustered.

- $\frac{s^2}{\bar{n}} < 1$. There is too little variation in quadrat point-counts compared to what is expected from a random pattern, suggesting the pattern is uniform (i.e., regular or dispersed).

Nearest-Neighbor Method

Unlike the quadrat method, nearest-neighbor methods do not rely on an artificial partitioning scheme but instead use the relative magnitude of nearest-neighbor (NN) distances as a natural test statistic of CSR. The NN distance simply refers to the distance between a point and its closest/nearest other point within the point pattern. The basic idea is that average nearest-neighbor distances tend to be smaller when a pattern is clustered and larger when a pattern is uniform (Figure 8). The significance of clustering or uniformity is measured by comparison to the expected magnitude of NN distances under CSR (Cressie, 1993; derivation in Appendix B).

Two-Tailed CSR Test

Given the standardized normal distribution of the sample mean of NN distances under CSR, $\text{Std}(\overline{N})$ (Eq. B.12 in Appendix B), the goal of the Clark-Evans test is to evaluate where the standardized mean NN distance, $Std(\overline{dm})$ (Eq. B.15 in Appendix B), of a point pattern falls within that distribution (Clark and Evans, 1954). In this case, we use a two-tailed test to assess whether the $Std(\overline{dm})$ is sufficiently small to infer clustering, or sufficiently large to infer uniformity. The two-tailed test involves calculating the probability that a random NN-distance from $Std(\overline{N})$ is larger or smaller than a given Z-score Z_α associated with a level of significance α (Figure 8) such that (Smith, 2014):

$$Pr(|Std(\bar{N})| \geq Z_\alpha) = Pr\big((Std(\bar{N}) \leq -Z_\alpha) \; or \; (Std(\bar{N}) \geq Z_\alpha)\big) = \alpha \qquad (2)$$

where $\alpha = 0.01$ is the level of significance, and $Z_\alpha = 2.58$ is the Z-score associated with the level of significance α. Therefore, the standardized mean of NN distances $Std(\overline{dm})$ is compared to Z_α to evaluate the spatial organization of a point pattern as follows (Figure 8):

- If $Std(\overline{dm}) > Z_\alpha$, the mean NN-distance is larger than what is predicted by the CSR hypothesis, and the pattern is considered strongly uniform.
- If $Std(\overline{dm}) < -Z_\alpha$, the mean NN-distance is smaller than what is predicted by the CSR hypothesis and the pattern is considered strongly clustered.
- If $|Std(\overline{dm})| < Z_\alpha$, the mean NN distance is within the range predicted by the CSR hypothesis, and the pattern is considered random.

K-function Method

Unlike previous methods, the K-function quantifies the scale of observed patterns and is able to detect multiple patterns at multiple scales. Unlike the quadrat method where scale (i.e., of quadrats) is fixed, the K-function allows scale to vary and incorporates its effects in the analysis. In addition, the K-function is not biased towards small-scale structures as is the case with traditional NN methods (Ripley, 1996). The K-function is therefore particularly suitable for patterns that display multiple structures at multiple scales. The K-function is given by (Ripley, 1976):

$$K(h) = \frac{1}{D}\left[\frac{1}{n}\sum_{i=1}^{n}\left(\sum_{i \neq j} I_h(d_{ij})\right)\right] \qquad (3)$$

where h is the scale, d_{ij} is the Euclidean distance between points s_i and s_j, $I_h(d_{ij})$ is the

indicator function such that $I_h(d_{ij}) = 1\ if\ d_{ij} < h$ and $I_h(d_{ij}) = 0\ if\ d_{ij} > h$, $\sum_{i \neq j} I_h(d_{ij}))$ gives the total number of points s_j within distance h of s_i, n is the total number of points inside the study region, and D is the point density. The expression in brackets can be understood as the average point count within distance h of all points within the point pattern. (See Appendix B for the K-function derivation under CSR.)

Anisotropic K-function

As discussed above, the k-function uses the scale variable h to calculate the point counts. Inherently, this means that the underlying point process is assumed to be isotropic: direction is not important. However, channel-belts exhibit very clear horizontal directionality given their inherent anisotropic shapes (i.e., width larger than thickness). Therefore, the goal now is to modify the K-function to suit anisotropic point processes such as channel-belt center points.

Expressing Directionality

To express the horizontal directionality of the data, directional ellipses with the horizontal axis as the major axis were used. The K-function uses the Euclidean distance to calculate the point count inside a circle of radius h. Instead, we use weighted Euclidean distances to define horizontal ellipses:

$$d(s_i, s_j) = \sqrt{w_1.(si_x - sj_x)^2 + w_2.(si_y - sj_y)^2} \tag{4}$$

where w_1 and w_2 reflect relative sensitivities of point counts to movements in the horizontal and vertical direction, respectively, and are defined as follow:

- $w_1 = \frac{b}{a}$, where a is the major radius

- $w_2 = 1$, where b is the minor radius

For example, given an ellipse with $a = 2h \; and \; b = h$, the corresponding weights are $w_1 = \frac{1}{2} \; and \; w_2 = 1$. In this case, the ellipse's horizontal axis is twice as large as the vertical axis.

CSR Test

Given an isotropic process, the K-function reduces to the area of a circle under CSR. In an anisotropic process, the K-function reduces to the area of the ellipse under CSR such that:

$$K(h) = \; area = \; \pi ab = \frac{\pi h^2}{w_1} \tag{5}$$

The K-function is then standardized to an L-function as follows:

$$L(h) = \sqrt{\frac{K(h).w_1}{\pi}} - h \tag{6}$$

Tests of CSR are constructed as follows:

- When $L(h) > 0$, the pattern is clustered at scale h
- When $L(h) < 0$, the pattern is dispersed at scale h

Monte Carlo Simulations

To measure the uncertainty related to the K-function values of the channel-belt point-pattern PP, K-function values are calculated for a large number of randomly generated point patterns of the same size and density. The goal is to compare the K-function values from the channel-belt point pattern to the statistical population of K-function values produced by 99 random Monte Carlo (MC) simulations given by

$R_n^{(i)}: i = 1, \ldots, 99$. L-function values are calculated for all random patterns over the same range of scales used for PP. The range of resulting L-function values $L_i(h)$ is then used to construct a random simulation envelope (Figure 9C). The simulation envelope is bounded by its lower-boundary $LB(h)$ and upper-boundary $UB(h)$, which are defined as follows (Smith, 2014):

$$LB(h): \min\{L_i(h): i = 1, \ldots, 99\} \quad (7)$$

$$UB(h): \max\{L_i(h): i = 1, \ldots, 99\} \quad (8)$$

The resulting random simulation envelope is then used to test for CSR as follows (Figure 9C):

- $L(h) > UB(h)$, the L-function value for PP is larger than the range of L-function values produced by 99 random MC simulations. This indicates significant clustering at scale h.
- $L(h) < LB(h)$, the L-function value for PP is smaller than the range of L-function values produced by 99 random MC simulations. This indicates significant uniformity at scale h
- $L(h) < UB(h)\ and\ L(h) > LB(h)$, the L-function value for PP falls within the range of L-function values produced by 99 random MC simulations. This indicates randomness at scale h.

Depositional Units Analysis

The three point-pattern analysis techniques were run on three datasets corresponding to the three different outcrops. For each outcrop, the analysis is performed locally on a depositional unit basis. This allows us to observe how the spatial organization of channel-belts varies as we move up-section through the seven previously identified depositional

units in Bull Canyon and Rock House Cove (Gooley, 2010; Pettinga, 2012). Also, for each outcrop, point-pattern analysis is performed on two versions of the channel-belt center-points dataset:

- *Perpendicular Projections*: these represent the coordinates of channel-belt center points when projected on a plane perpendicular to paleocurrent direction.
- *Parallel Projections*: these represent the coordinates of channel-belt center points when projected on a plane parallel to outcrop orientation.

Moving Window Analysis

Since architectural change between successive depositional units is gradational over several meters, confining the analysis to depositional intervals separated by discrete boundaries may bias the resulting interpretation. Therefore, a moving window analysis is performed to minimize this bias and to capture the continuous evolution of spatial organization of channel-belts over time (i.e., between depositional units). The moving window analysis can also provide a benchmark that can help validate or reject the existing depositional unit scheme. The moving window analysis is performed using the quadrat method and the K-function.

Quadrat-based Moving Window Analysis

The window is set to move vertically at 1m increments from the base (where exposed) to the top of the John Henry Member. For each window position, the window's width is constrained by the maximum and minimum x coordinates of channel-belt center points while its height is defined as two times the quadrat length. The analysis is run five times with each run using a different quadrat length (15 m, 20 m, 25 m, 30 m, and 35 m) in order to reduce bias associated with quadrat size.

K-function-based Moving Window Analysis

The K-function moving window also moves in 1m increments and has a variable width that is constrained by the maximum and minimum x coordinates of channel-belt center points within the window. However, the window has a fixed height of 150 m which sets an upper scale limit of 150 m. For each position of the window, the pattern's K-function is computed and compared against K-function values from 99 random Monte Carlo simulations generated using the same point density observed within the pattern. To measure the statistical significance of the pattern's clustering, p-values were calculated for each window position and scale. A p-value describes the probability of obtaining an observed K-function value from a random point pattern (i.e., when the CSR hypothesis is true) and is given by:

$$Pvalue = \frac{S_L}{S_T} \tag{9}$$

where S_L is the number of simulations with K-values larger than the pattern's K-value and S_T is the total number of simulations.

Correlation Analysis Using Dynamic Time Warping

To evaluate whether up-section clustering trends (i.e., obtained using the quadrat-based moving window) in the three outcrops are related, dynamic time warping (DTW) is used to quantify the degree of similarity between clustering curves (Sakoe and Chiba, 1978). While many other measures of similarity are available, dynamic time warping algorithm is selected based on its ability to find the optimal alignment between two time series that are locally out of phase while taking into account size and format differences between two vectors. To align the two time series V and W of sizes n and m,

respectively, DTW relies on constructing an n-by-m cost matrix M where each cell contains a cost value calculated as follows:

$$M(i,j) = Distance(V_i, W_j)^2 \quad (10)$$

The optimal alignment between the two vectors corresponds to the shortest path through the matrix that minimizes the total warping cost between the two vectors.

Figure 5 – Interpreted gigapans of the fluvial John Henry Member in (A) east Bull Canyon (modified from Pettinga, 2012), and (B) west Bull Canyon (modified from Turner, 2014). Yellow polygons outline channel-belt sandstone bodies while green lines indicate boundaries between different depositional units.

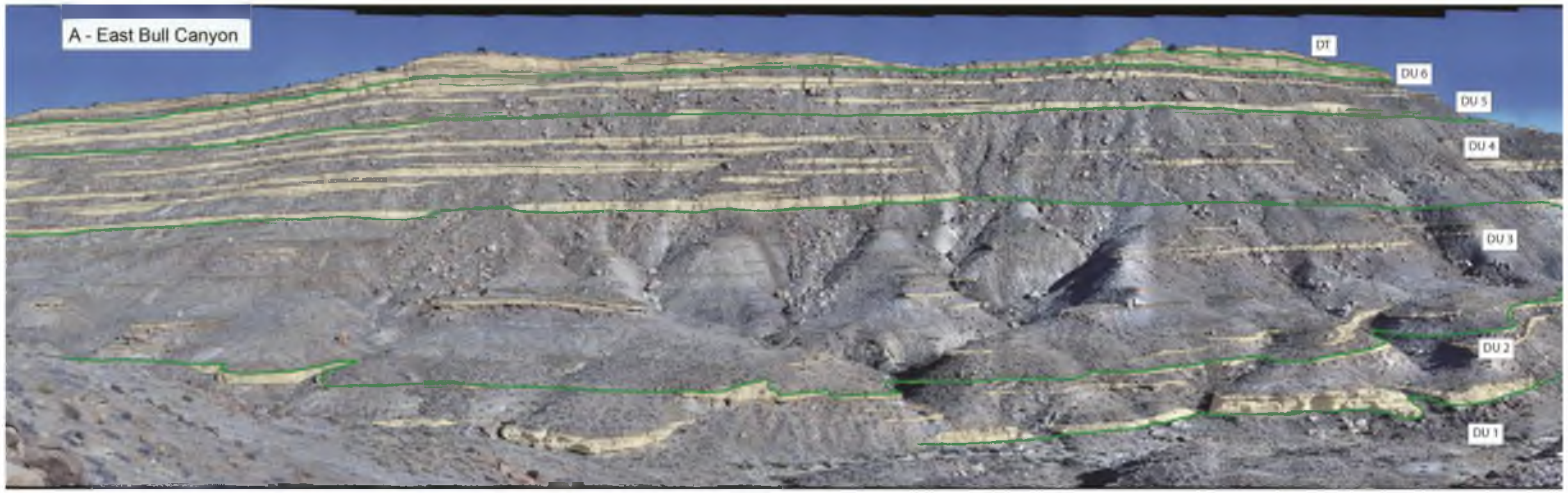
A - East Bull Canyon
DT
DU 6
DU 5
DU 4
DU 3
DU 2
DU 1

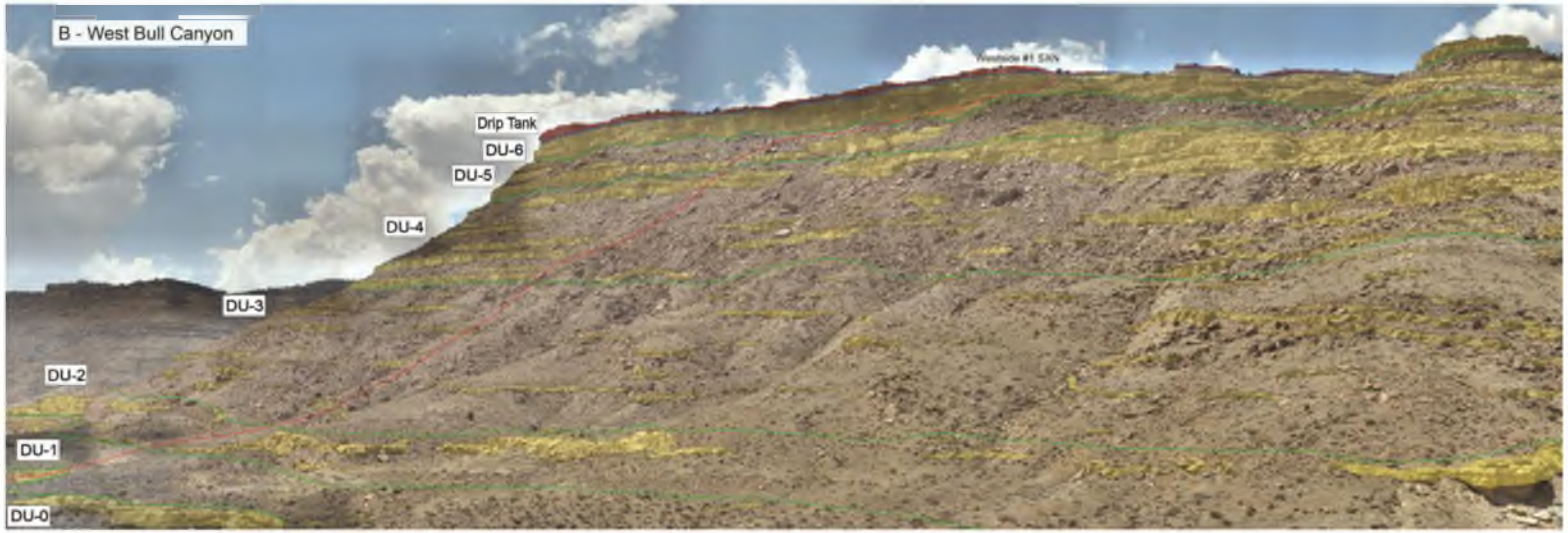
B - West Bull Canyon
Drip Tank
DU-6
DU-5
DU-4
DU-3
DU-2
DU-1
DU-0

Figure 6 – Interpreted gigapan of the fluvial John Henry Member in northwest Rock House Cove. Yellow polygons outline channel-belt sandstone bodies while green lines indicate boundaries between different depositional units (modified from Gooley, 2010).

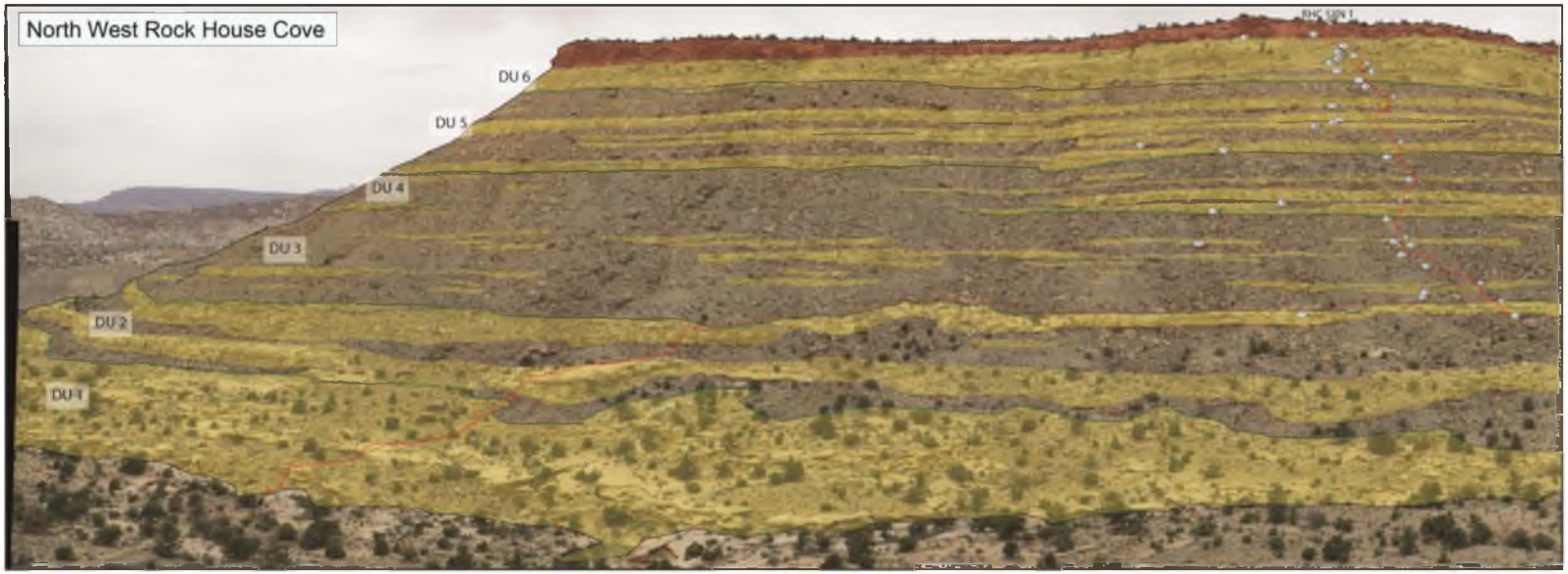
North West Rock House Cove
DU 6
DU 5
DU 4
DU 3
DU 2
DU 1

Figure 7 – Digital elevation model (DEM) of (A) west Bull Canyon (4x vertical exaggeration) and (B) northwest Rock House Cove (no vertical exaggeration). Spheres represent GPS points of channel-belts and are colored based on the depositional unit they belong to. Blue planes are projection planes oriented perpendicular to average paleocurrent direction. Light-gray horizontal surfaces represent depositional unit boundaries.

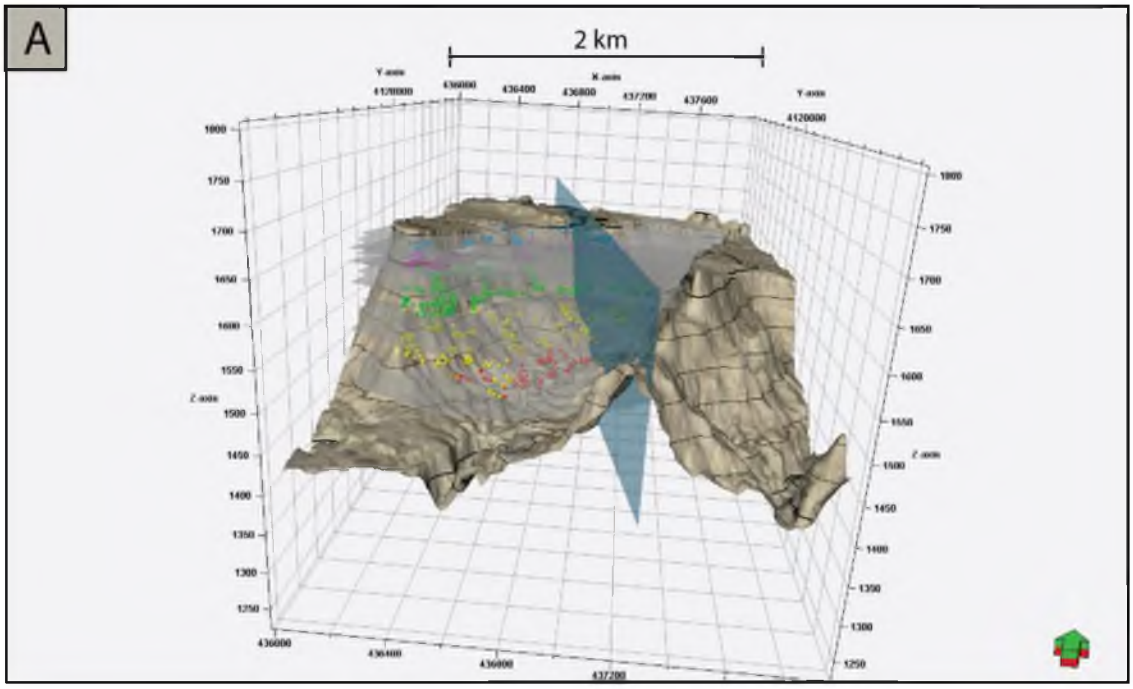
A
2 km
Y-axis
X-axis
Z-axis

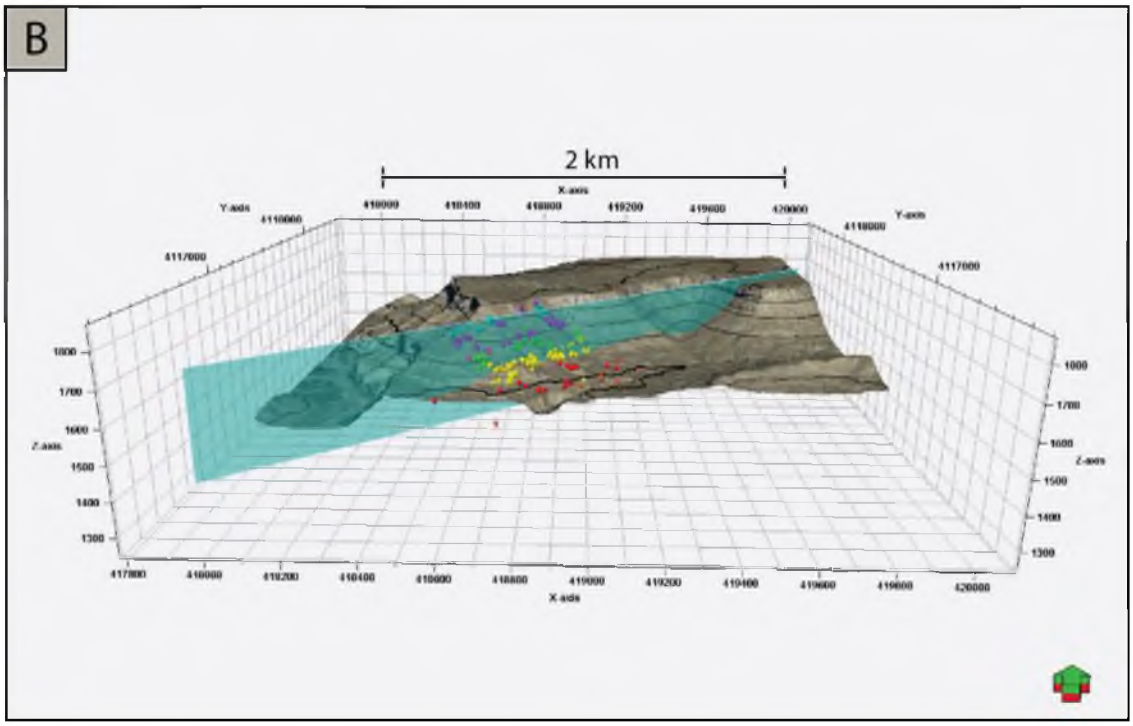
B
2 km
X-axis
Y-axis
Z-axis

Figure 8 – Schematic illustrations of various types of point patterns and various tests of the CSR condition. (A) Illustrations of three general types of point patterns: uniform, random, and clustered. (B) The quadrat method uses the ratio of variance/mean as a predictor of point pattern type. (C) The nearest-neighbor method uses the standardized mean nearest-neighbor distance $Std(d)$ as a test statistic of clustering vs uniformity. The two tails of the standardized normal distribution of NN-distances are defined based on Z-scores associated with the level of significance α.

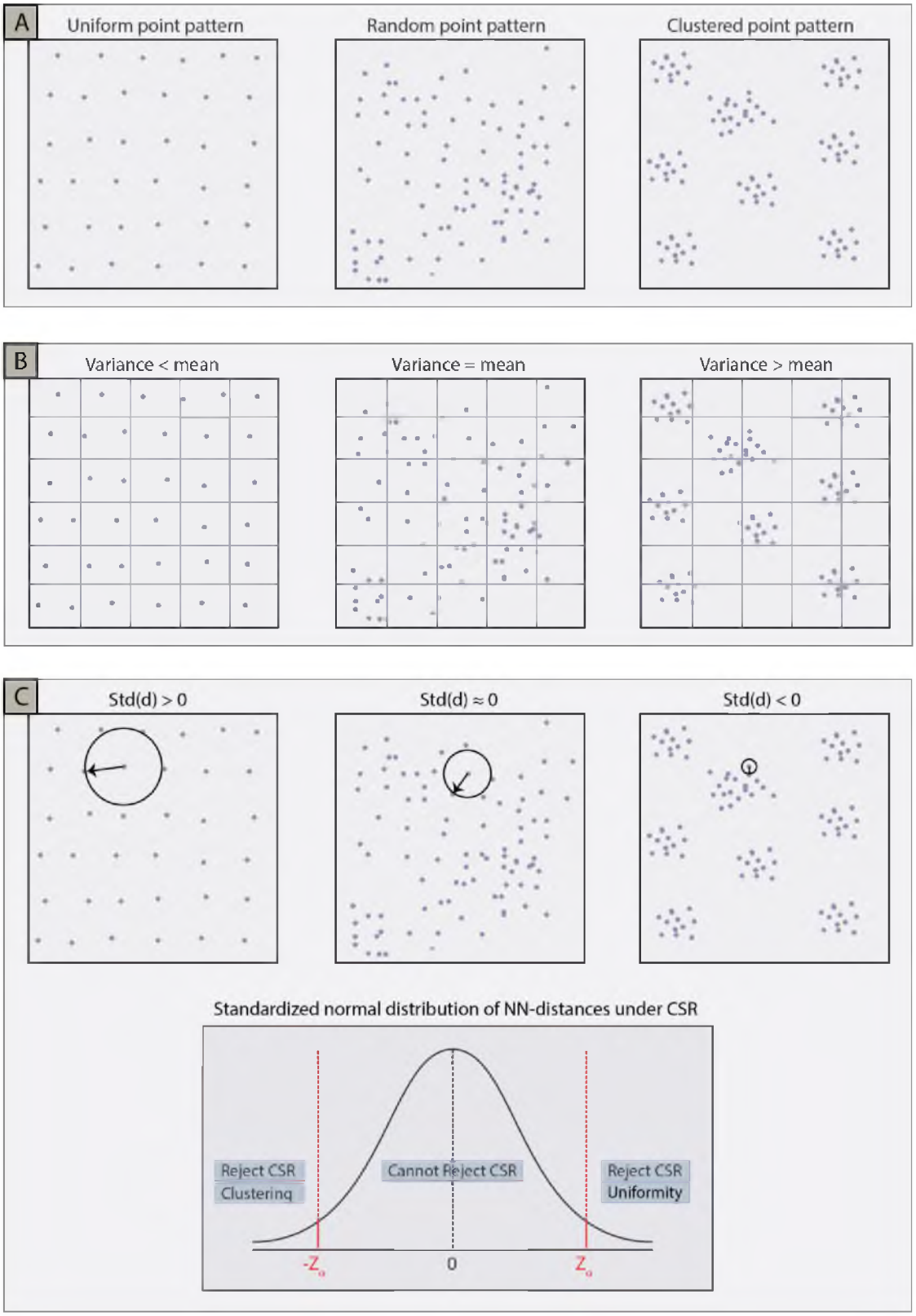
A
Uniform point pattern
Random point pattern
Clustered point pattern
B
Variance < mean
Variance = mean
Variance > mean
C
Std(d) > 0
Std(d) ≈ 0
Std(d) < 0
Standardized normal distribution of NN-distances under CSR
Reject CSR
Clustering
Cannot Reject CSR
Reject CSR
Uniformity
-Z0
0
Z0

Figure 9 – Schematic illustrations of edge effects and K-function plots. (A) Illustration of the edge effect problem of the K-function. (B) Edge effect correction suggested by Ripley (1979). (C) K-function plots for various point patterns where the x-axis is the scale and the y-axis if the K-function value. The green envelope represents the range of K-function values corresponding to a given number of random Monte Carlo simulations and is bound by the upper boundary (UB) and the lower boundary (LB). The bold black line shows the K-function values for the test pattern.

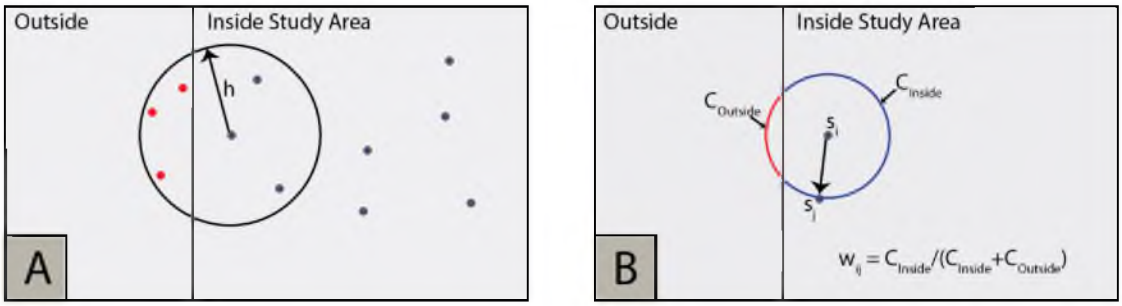
Outside
Inside Study Area
h
A
Outside
Inside Study Area
$C_{Outside}$
C_{Inside}
s_i
s_j
B
$w_{ij} = C_{Inside}/(C_{Inside}+C_{Outside})$

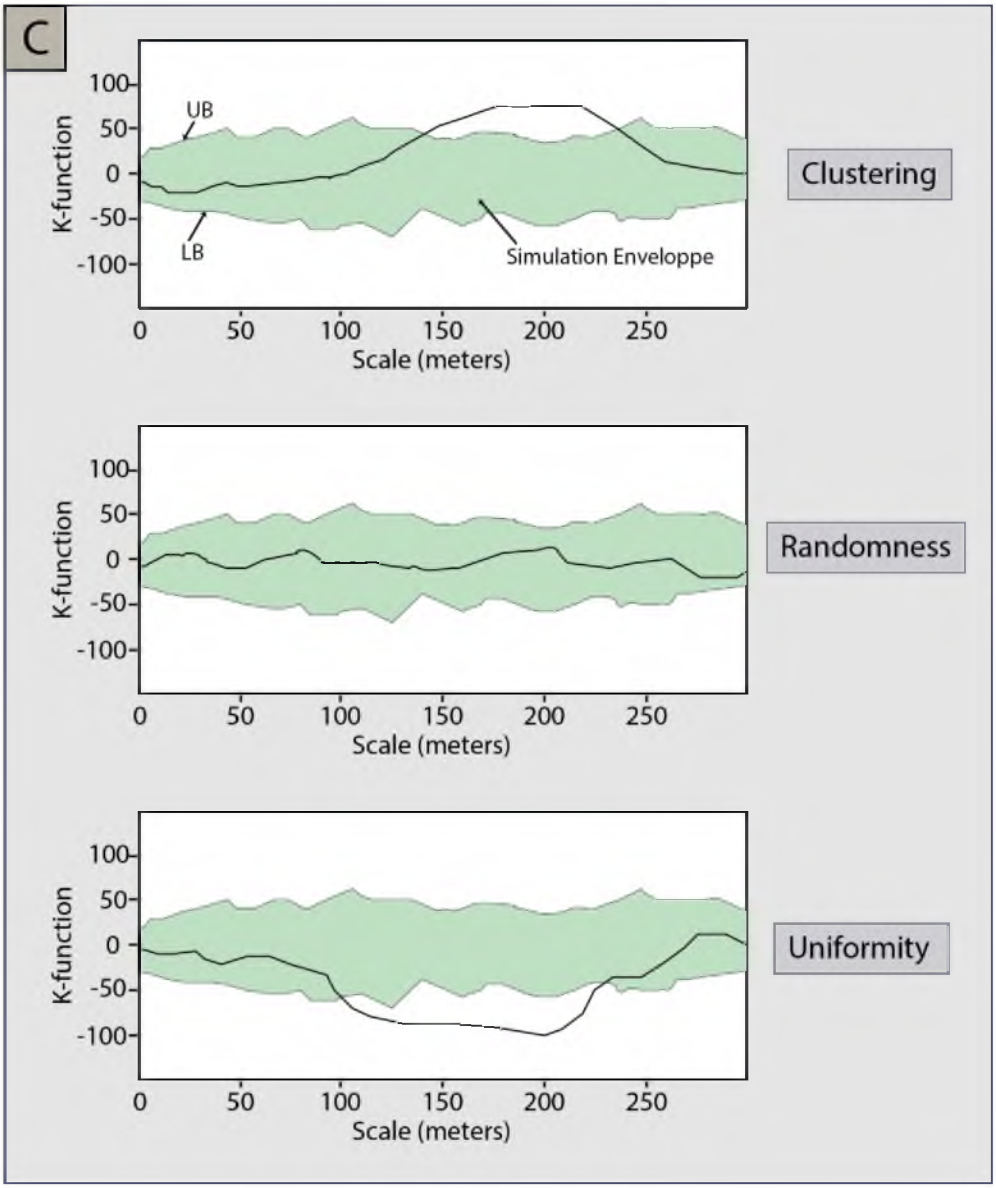
C
K-function
100
50
0
-50
-100
UB
LB
Simulation Enveloppe
0
50
100
150
200
250
Scale (meters)
Clustering
Randomness
Uniformity

RESULTS

Depositional Unit Analysis

The results of the depositional unit analysis are presented for each outcrop separately. Unlike the Bull Canyon East dataset, DU-0 and DU-1 in Bull Canyon West and Rock House Cove were discarded from the analysis to avoid uncertainty linked to low point-counts or because of limited outcrop exposure.

Bull Canyon East

Quadrat Method Results

Using a quadrat size of 25m, the quadrat analysis classifies the perpendicular projections in DU-0, DU-1, and DU-5 as uniform; DU-2, DU-3, and DU-4 as clustered; and DU-6 as random (Figure 10). Clustering trends observed in the perpendicular projections closely resemble those observed in parallel projections indicating the orientation of projections has little influence on the results of the quadrat method. Maximum clustering of channel-belts, as indicated by largest variance/mean ratio, occurs in DU-2 while minimum clustering occurs in DU-1.

Nearest-Neighbor Method Results

The Clark-Evans two-tailed test classifies the perpendicular projections in DU-0 and DU-1 as random, and all other units as clustered (Figure 10). While this classification is in disagreement with the quadrat method, the relative clustering trends between successive units are very similar in the two methods (Figure 10). Clustering trends of

parallel projections correlate with those of the perpendicular projections, indicating that the orientation of projections has little effect on the results of the nearest-neighbor method. As with the quadrat method, maximum clustering, as indicated by smallest mean nearest-neighbor distance, occurs in DU-2 while maximum uniformity occurs in DU-0 and DU-1.

K-function Method Results

The K-function value was calculated for a number of scales at 1m increments up to a maximum 200m limit – this upper limit is set in order to reduce edge effects associated with outcrop thickness. DU-0 and DU-1 were not classified given the incompatibility of this method with the low point counts within these units.

Isotropic K-function

The isotropic K-function classifies the perpendicular projections of DU-3 and DU-5 as random at all scales, while DU-2, DU-4, and DU-6 are classified as clustered at different scales (Figure 10). In DU-2, all K-function values for scales lower than 190 m plot within the random simulation envelope while values above the 190 m scale plot above the envelope. This indicates the pattern is random at all scales up to 190 m but is clustered at scales larger than 190 m. This classification is in agreement with results from previous methods. In DU-4, channel-belts are clustered at the 40 m scale and around the 100 m scale mark. Outside these intervals, the pattern is random. Finally, the channel-belts of DU-6 are clustered from small to medium scales (10 m to 120 m) but are random outside this interval.

Anisotropic K-function

To understand the effect of channel-belt anisotropy on the resulting classification, the perpendicular projections were reclassified using the anisotropic K-function (Figure 10). In DU-2, channel-belts are found to be clustered at scales of 100 m and larger. The point pattern of DU-3 shows clustering at the 40 m and 200 m scales, which was not identified with the isotropic K-function. In DU-4, clustering is also observed from 50 m to 80 m scales and from 150 m to 200 m scales. The large-scale clustering was not identified with the isotropic K-function. As with the isotropic K-function, the point pattern of DU-5 is classified as random at all scales while the pattern of DU-6 shows clustering from small to medium scales (10 to 110 m). It is worth noting that in some DUs, K-function values that barely exceed the maximum random K-function values have been used to interpret clustering. Ideally, cases like these would need a much larger number of Monte Carlo simulations to assert for certain the presence of the pattern.

Bull Canyon West

Quadrat Method Results

Using the same quadrat method settings, the perpendicular projections of DU-5 are classified as uniform and those of the remaining units as clustered (Figure 11). Classification of the parallel projections shows overall similar trends except in DU-6 where channel-belt center points are classified as uniform instead of clustered. Maximum clustering occurs in DU-3 while maximum uniformity occurs in DU-5.

Nearest-Neighbor Method Results

The two-tailed test classifies the perpendicular projections of DU-6 as random, and all other units as clustered (Figure 11). For the parallel projections, DU-5 and DU-6

are classified as random and all other units as clustered. The clustering trends observed in parallel and perpendicular projections are also very similar (Figure 11). As with the quadrat method, maximum clustering is observed in DU-3 while minimum clustering occurs in DU-5 and DU-6.

K-function

Isotropic K-function

The isotropic K-function classifies the perpendicular projections of DU-5 as random, and all other units as clustered at different scales (Figure 11). In DU-2, channel-belts are clustered at large scales (>190 m). In DU-3, clustering occurs at small to medium scales (10 to 150 m). DU-4 shows clustering at almost all scales (20 to 200 m) while DU-5 shows randomness at all scales. Finally, the point pattern in DU-6 is clustered at small scales (20 to 60 m) and large scales (150 to 170 m).

Anisotropic K-function

The anisotropic K-function results are in agreement with those of the isotropic K-function in terms of the types of patterns identified in different units. However, there are differences associated with the scales of these patterns (Figure 11). Unlike the isotropic K-function classification, clustering in DU-2 is now recognized over both medium (80 to 100 m) and large scales (160 to 200 m) while clustering in DU-3 and DU-4 is restricted to small and medium scales (<100 m). Finally, channel-belts in DU-6 are clustered at small (20 to 40 m) and medium scales (70 to 90 m) and uniform at large scales (>195 m).

Rock House Cove

Quadrat Method Results

Using the same settings again, the perpendicular projections of DU-2, DU-5, and DU-6 are classified as uniform, while those of DU-3 and DU-4 are classified as clustered (Figure 12). Two general trends are identified: a trend of increasing clustering from DU-2 to DU-3, followed by decreasing clustering from DU-3 to DU-6. Similar trends are identified in the parallel projections but with a turnaround point located in DU-5 as opposed to DU-3 in the perpendicular projections. Maximum clustering for perpendicular projections is observed in DU-3.

Nearest-Neighbor Method Results

Using the two-tailed test, the perpendicular projections in DU-2 are classified as random, while those of the remaining units are classified as clustered (Figure 12). As with the quadrat method, two general trends are observed: a trend of increasing clustering from DU-2 to DU-3 followed by a trend of decreasing clustering from DU-3 to DU-6. These same trends are also observed in the parallel projections. This result adds support and validates the trends observed in the perpendicular projections with the quadrat method. Maximum clustering occurs in DU-3.

K-function

Isotropic K-function

Perpendicular projections of DU-2, DU-3, and DU-5 are classified as clustered over different scales, while those of DU-4 and DU-6 are classified as random over all scales (Figure 11). In DU-2 and DU-3, clustering occurs at medium to large scales (>150 m scale). In DU-5, channel-belts are clustered at small (30 to 50 m) and large scales

(>160 m).

Anisotropic K-function

Unlike the isotropic K-function, the anisotropic K-function recognizes patterns of uniformity in addition to patterns of clustering in DU-3, DU-4, and DU-5. In DU-3, clustering occurs at small scales (30 m) while uniformity is identified at larger scales (>160 m). In DU-4, clustering occurs at large scales (130 to 150 m) while uniformity is observed at medium scales (70 to 90 m). Finally, channel-belts of DU-5 are clustered at small (10 to 20 m) and medium scales (80 to 100 m) and are uniform at large scales (>160 m).

Moving Window Analysis

Quadrat-based Moving Window Analysis

Figure 13 shows the results of the quadrat-based moving window analysis for each dataset; the x-axis represents the clustering index (i.e., variance/mean) while the y-axis shows the vertical position of the window as a vertical offset from the top of the John Henry Member. Each data point is the average of five clustering indices that correspond to the five different quadrat lengths. The analysis identifies two general trends in all outcrops: (1) a trend of decreasing channel-belt clustering from DU-2 to DU-4, and (2) a trend of increasing clustering from DU-5 to DU-6 (Figure 13).

K-function-based Moving Window Analysis

Figure 14 shows the results of the K-function moving window analysis for each dataset; the white surface shows the pattern's K-function values for each scale and window position while the blue and red surfaces represent, respectively, the minimum

and maximum K-function values associated with the random Monte Carlo simulations. The 3D K-function plots show that scales of patterns of clustering and randomness are overall constant across different window positions (i.e., scales do not change as the window moves up-section). This observation is also highlighted in the p-value plots, which show the presence of two types of patterns at different scales that are consistent across the three outcrops: (1) a pattern of small-scale clustering indicated by the low p-value plateau and (2) a pattern of larger scale uniformity indicated by the rugged surface of high p-values (Figure 14).

Similarity Analysis using Dynamic Time Warping

To evaluate whether up-section clustering trends (e.g., obtained using the quadrat-based moving window) in the three outcrops are related, dynamic time warping (DTW) is used to quantify the degree of similarity between clustering curves (Sakoe and Chiba, 1978). DTW is also used to find a nonlinear time mapping between the three clustering curves when they are locally out of phase. This is useful when dealing with fluvial strata in different outcrops with no regional time markers. Figure 15 shows the resulting DTW alignment along with the underlying cost-matrix. Calculated correlation coefficients between different clustering curves increase significantly after the DTW alignment. The warped clustering curves of Bull Canyon east and west have a correlation coefficient of 0.6 compared to a coefficient of 0.33 before the alignment. Similarly, the warped clustering curves of Bull Canyon east and Rock House Cove have a correlation coefficient of 0.7 compared to a coefficient of 0.3 before the alignment (Figure 15).

Figure 10 – Classification of the spatial organization of channel-belts in each depositional unit in east Bull Canyon using (A) the quadrat method, (B) nearest-neighbor method, and (C) the K-function. Gray boxes in K-function plots highlight the scales over which clustering is observed.

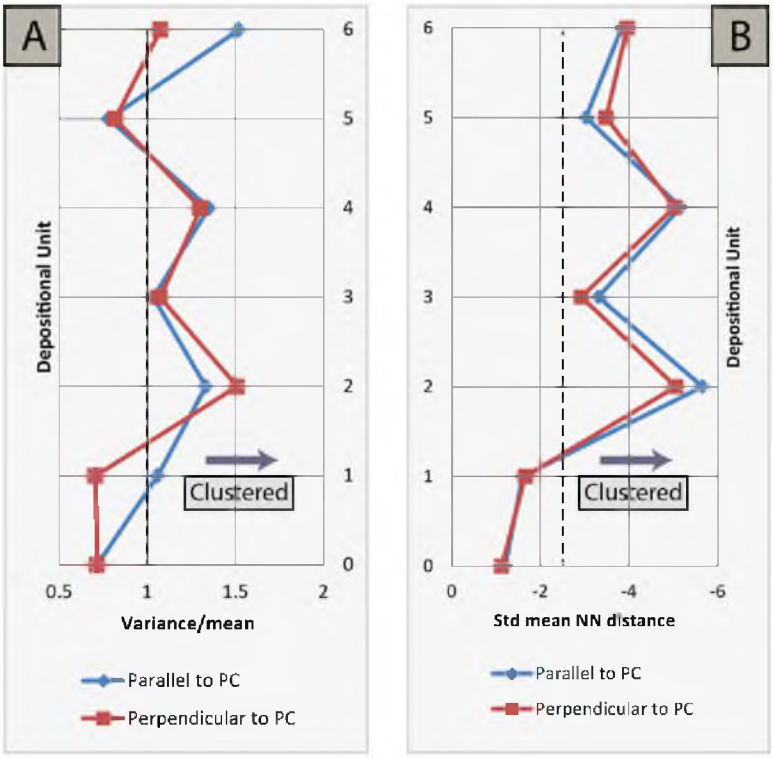
A
B
Depositional Unit
Clustered
Variance/mean
Std mean NN distance
Parallel to PC
Perpendicular to PC

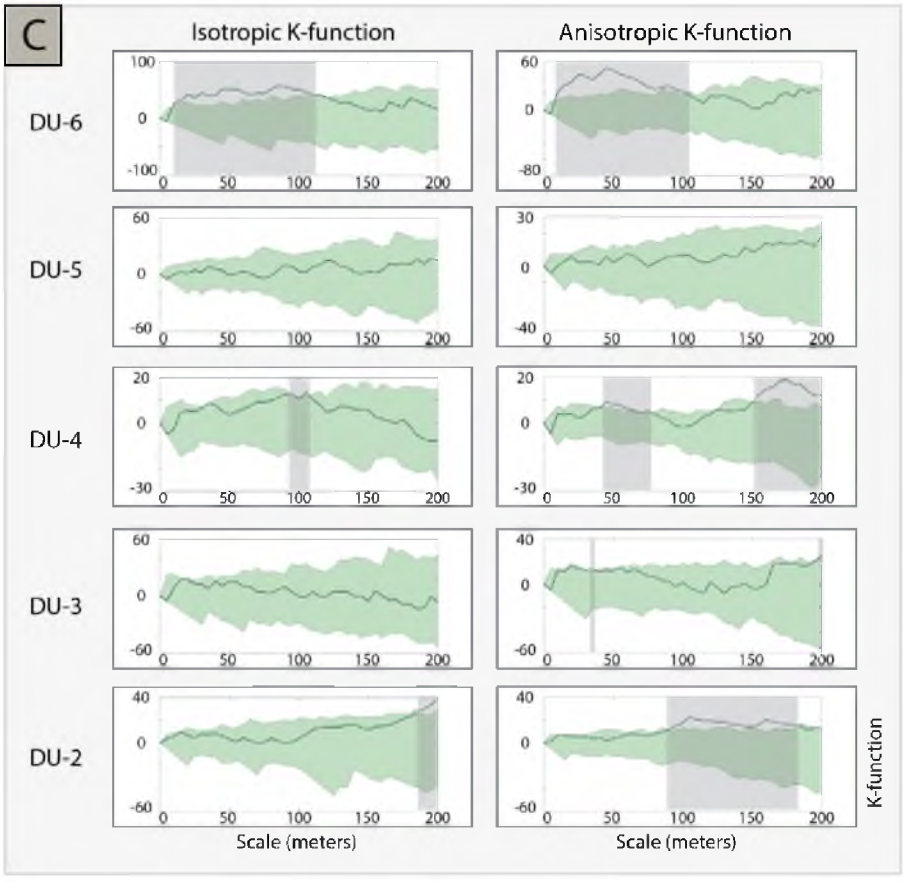
C
Isotropic K-function
Anisotropic K-function
DU-6
DU-5
DU-4
DU-3
DU-2
Scale (meters)
K-function

Figure 11 – Classification of the spatial organization of channel-belts in each depositional unit in west Bull Canyon using (A) the quadrat method, (B) nearest-neighbor method, and (C) the K-function.

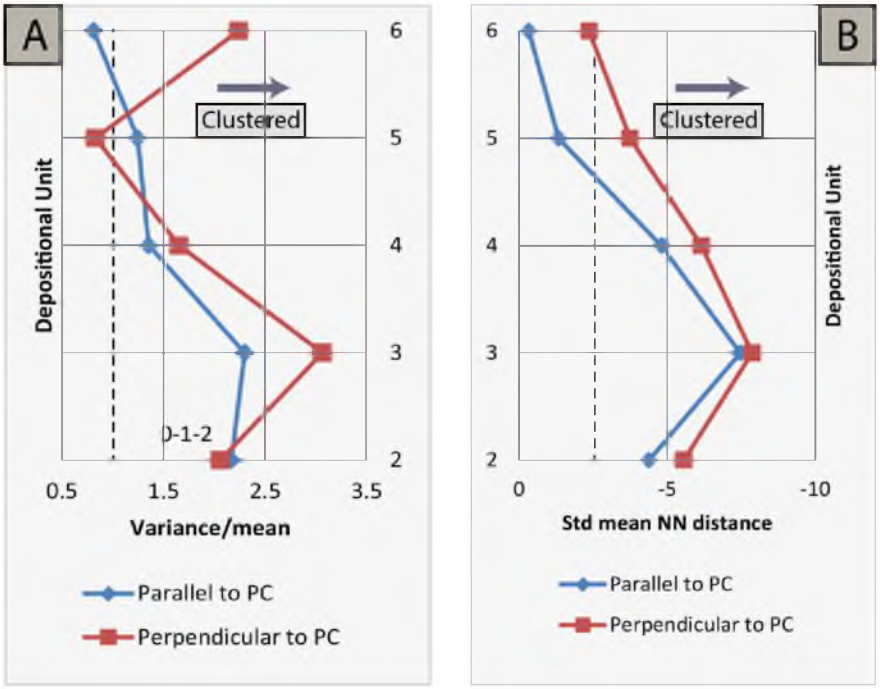
A
Clustered
Depositional Unit
6
5
4
3
2
0-1-2
0.5
1.5
2.5
3.5
Variance/mean
Parallel to PC
Perpendicular to PC
B
Clustered
Depositional Unit
0
-5
-10
Std mean NN distance
Parallel to PC
Perpendicular to PC

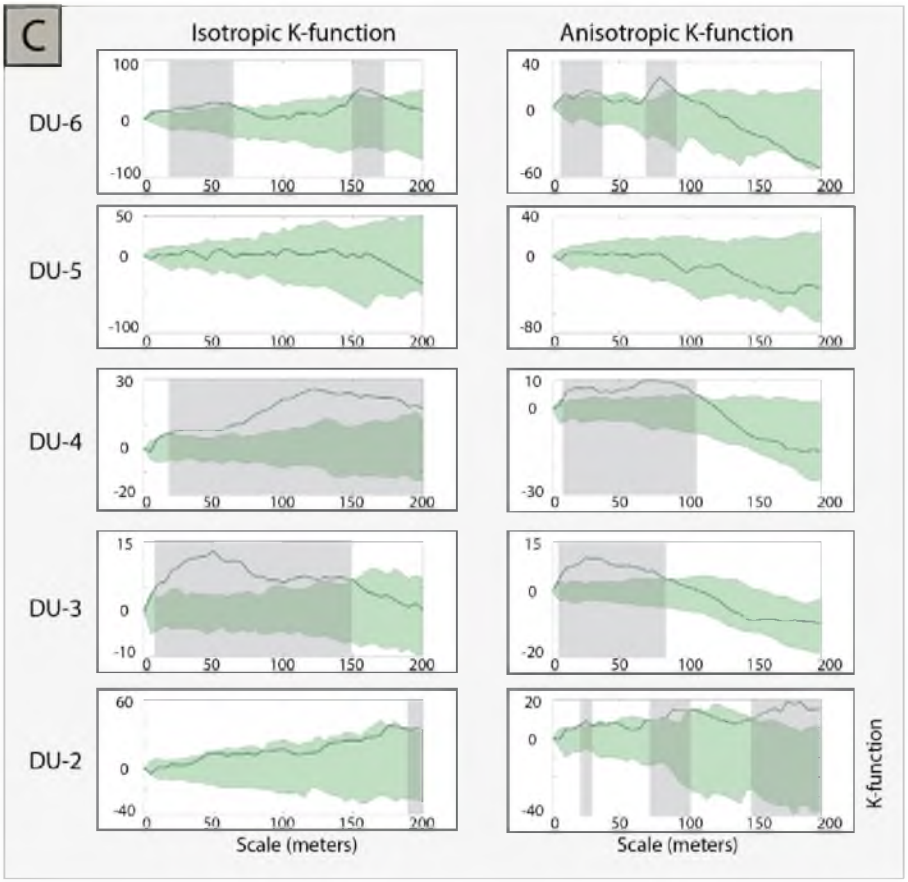
C
Isotropic K-function
Anisotropic K-function
DU-6
DU-5
DU-4
DU-3
DU-2
Scale (meters)
Scale (meters)
K-function

Figure 12 – Classification of the spatial organization of channel-belts in each depositional unit in northwest Rock House Cove using (A) the quadrat method, (B) nearest-neighbor method, and (C) the K-function.

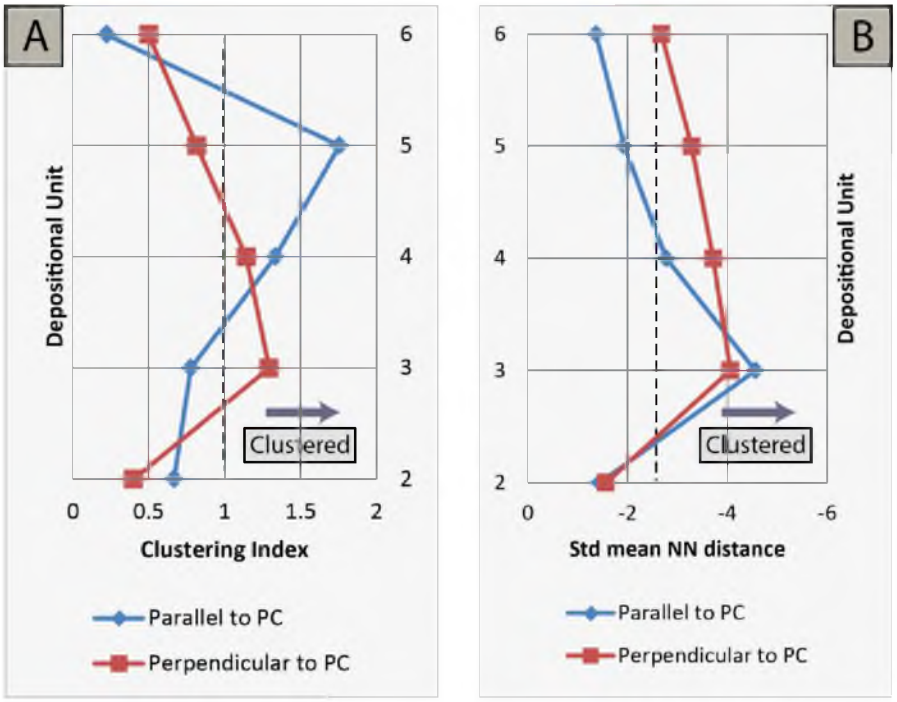
A
Depositional Unit
Clustered
Clustering Index
Parallel to PC
Perpendicular to PC
B
Depositional Unit
Clustered
Std mean NN distance
Parallel to PC
Perpendicular to PC

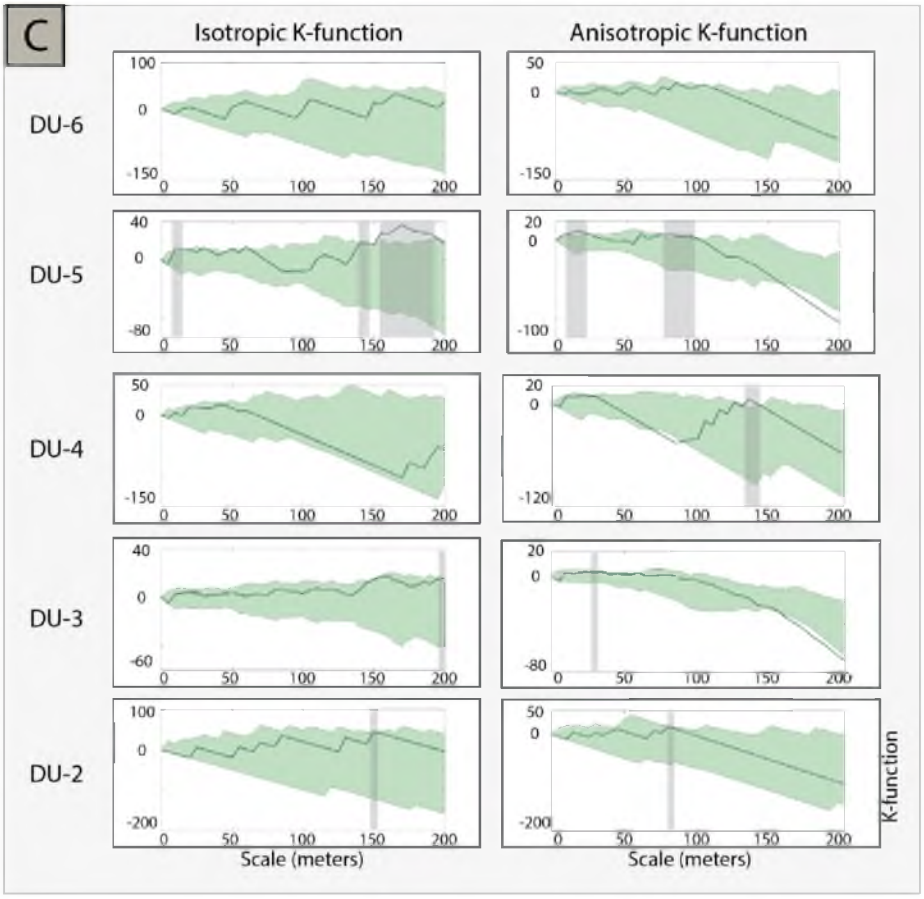
C
Isotropic K-function
Anisotropic K-function
DU-6
DU-5
DU-4
DU-3
DU-2
Scale (meters)
Scale (meters)
K-function

Figure 13 – Quadrat-based moving window analysis of the spatial organization of channel-belt center-points in the three outcrops. Two overall trends are identified: (1) a trend of increasing uniformity from DU-2 to DU-4 and (2) a trend of increasing clustering in the upper stratigraphic interval from DU-5 to DU-6. Colored boxes show the average clustering index per depositional unit.

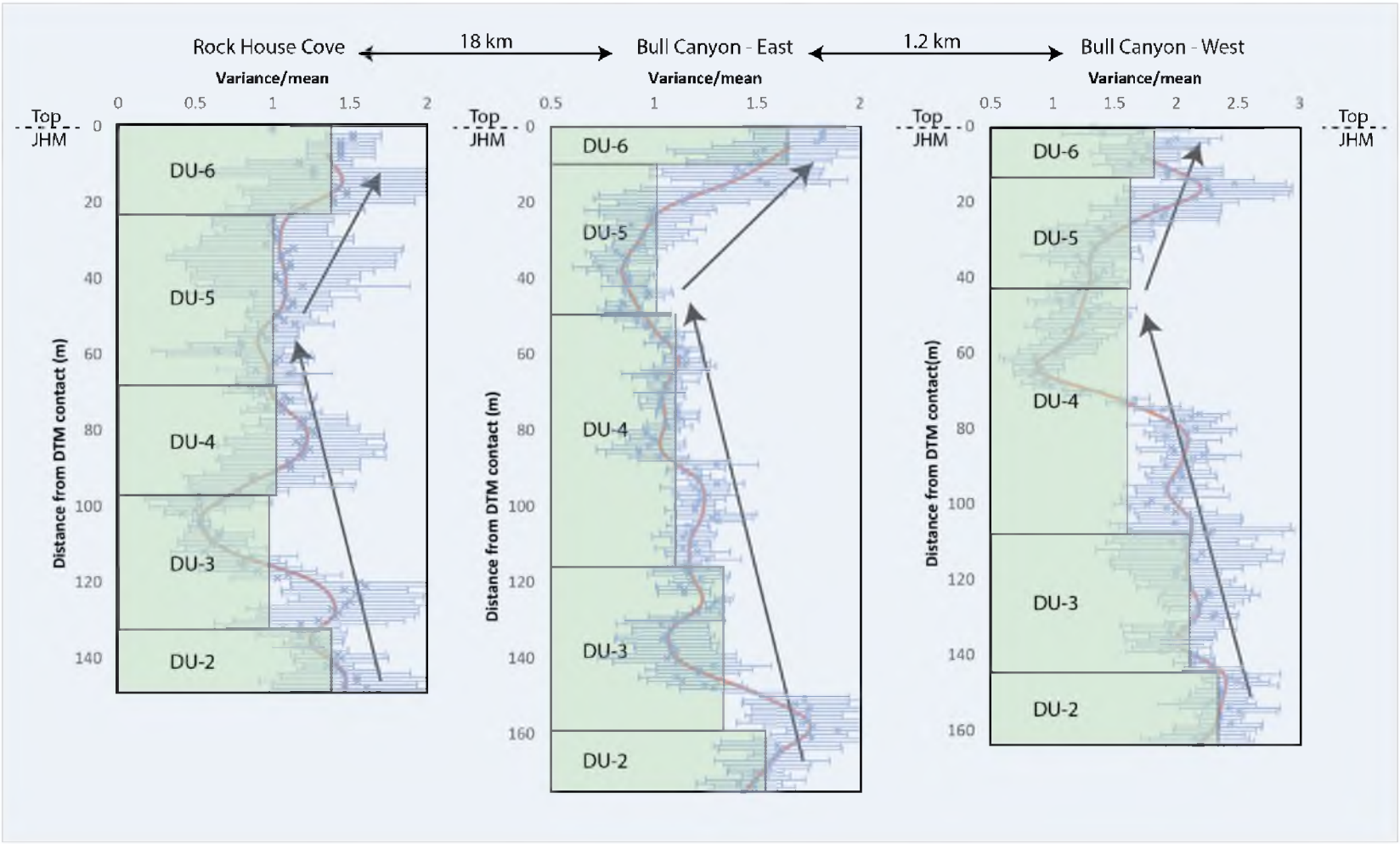
Rock House Cove
18 km
Bull Canyon - East
1.2 km
Bull Canyon - West
Variance/mean
Top JHM
DU-6
DU-5
DU-4
DU-3
DU-2
Distance from DTM contact (m)
Distance from DTM contact(m)

Figure 14 – K-function-based moving window analysis of the spatial organization of channel-belt center-points in the three outcrops. In the 3D K-function plots, the blue and red surfaces represent, respectively, the minimum and maximum K-function values produced by 99 random Monte Carlo simulations for every scale and window position. The white surface represents the K-function values produced by our channel-belt pattern. The P-value 3D plots suggest two types of patterns are present at different scales in all outcrops; (1) small-scale clustering as indicated by low p-values at small and medium scales and (2) medium to large-scale uniformity as indicated by high p-values at larger scales.

Rock House Cove

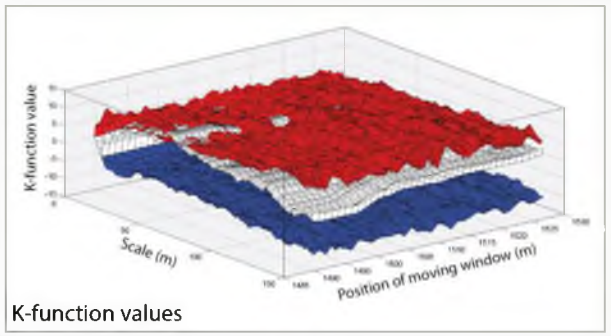

K-function values

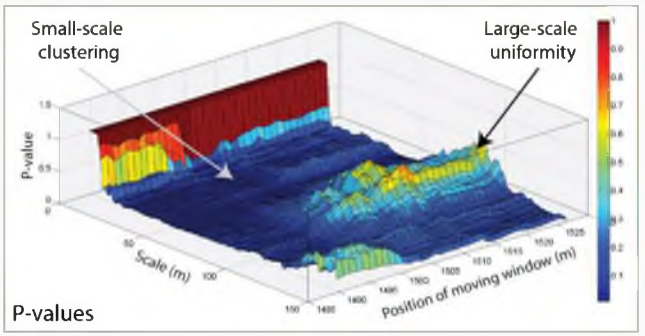

P-values

Bull Canyon - East

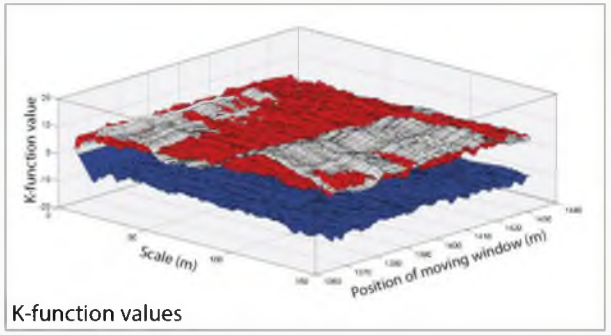

K-function values

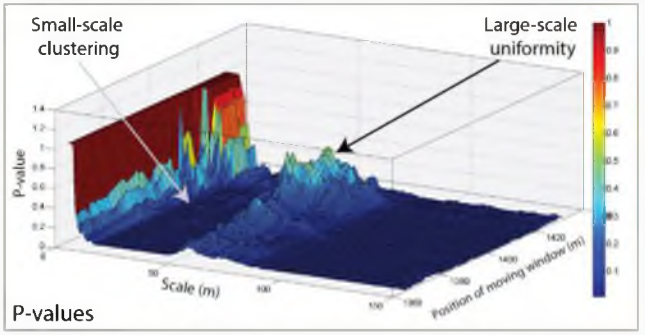

P-values

Bull Canyon - West

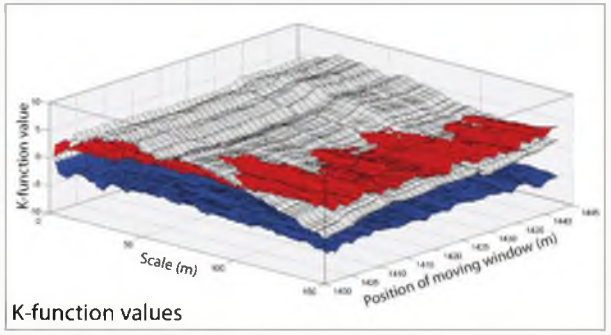

K-function values

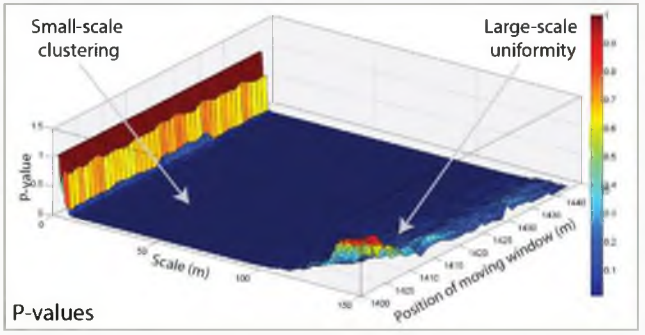

P-values

Figure 15 – Correlation analysis of moving window clustering curves using dynamic time warping. The figure shows the optimal alignment between clustering curves of (A) Bull Canyon east and west, and (B) Bull Canyon east and Rock House Cove. The figure also shows the corresponding cost matrices and correlation coefficients for both cases.

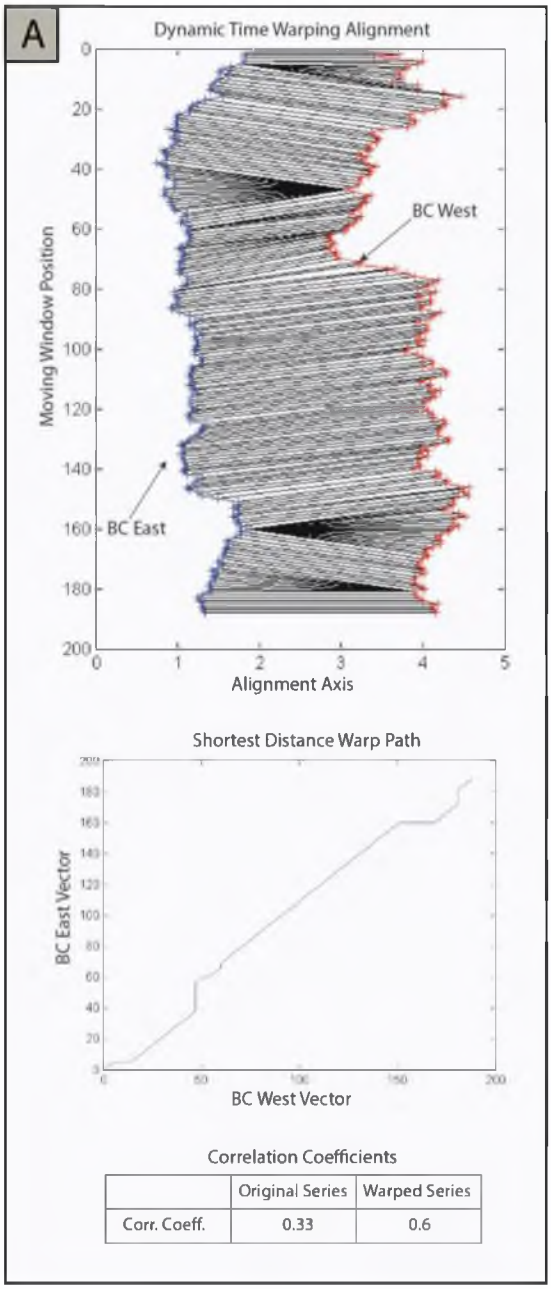

Correlation Coefficients

	Original Series	Warped Series
Corr. Coeff.	0.33	0.6

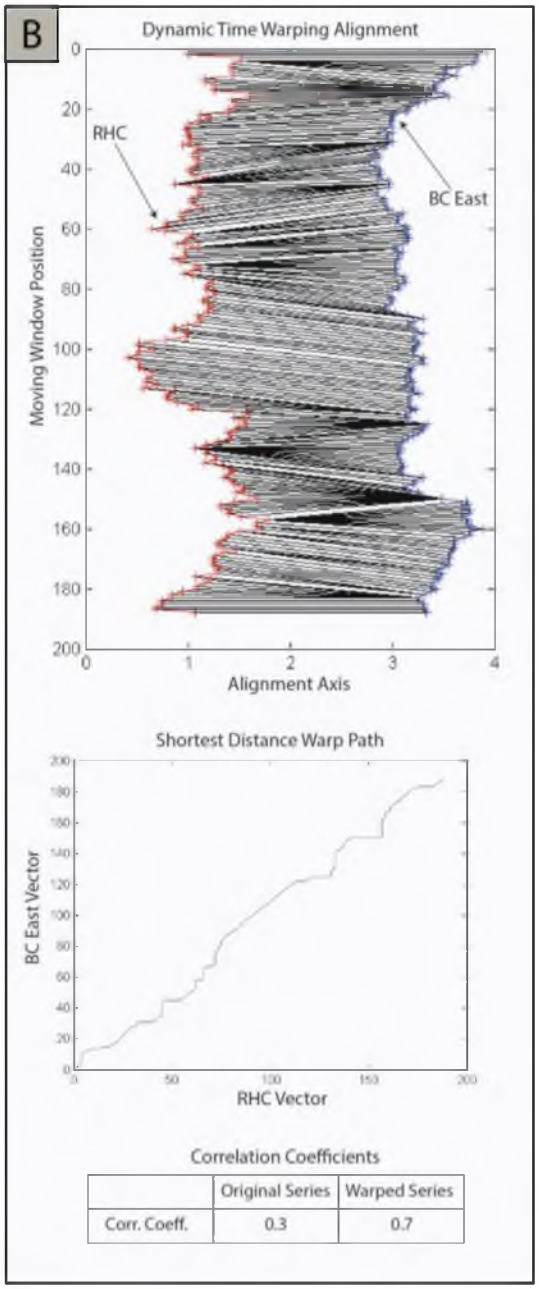

Correlation Coefficients

	Original Series	Warped Series
Corr. Coeff.	0.3	0.7

DISCUSSION

The quadrat-based moving window analysis reveals two general trends in the stratigraphic arrangement and spatial organization of channel-belts throughout deposition of the fluvial JHM. These trends are qualitatively observed in all three datasets. This suggests that channel-belt stacking patterns were controlled by similar processes in these three outcrops. The moderate to strong correlation coefficients of the DTW-aligned clustering curves confirm the consistency of spatial patterns observed in the three outcrops. Furthermore, given the 18 km of distance separating Rock House Cove from Bull Canyon, the overall clustering patterns are interpreted to reflect changing regional allogenic conditions.

To understand the specific processes controlling the observed channel-belt stacking patterns, we compare the results of our analysis to predictions of five widely-cited numerical and experimental models of alluvial architecture (Bridge and Leeder, 1979; Bryant et al., 1995; Mackey and Bridge, 1995; Jerolmack and Paola, 2007; Straub et al., 2009). This is possible because the synthetic stratigraphy generated by these models can be directly linked to unique input parameters, boundary conditions, and fluvial processes.

Controls on Spatial Organization of Channel-belts

The strength and significance of channel-belt clustering throughout deposition of the JHM was found to be positively correlated with previously documented architectural

parameters (Gooley, 2012; Pettinga, 2012; Turner, 2014). For instance, the upward trend of decreasing clustering in the middle stratigraphic interval in Bull Canyon East is associated with vertical trends of decreasing channel-belt width and thickness, NTG, amalgamation, and median bedload sediment size (D50 bedload). Similarly, the trend of upward increasing clustering in the upper stratigraphic interval is associated with increases in these same parameters (Figure 16). Given that this positive correlation exists in the three studied outcrops, changes in channel-belt stacking patterns are interpreted to be a product of the same processes responsible for changes in other architectural parameters. Previous authors have attributed changes in various architectural parameters to changes in the balance of accommodation and sediment supply due to tectonic activity and base level fluctuations (Pettinga, 2012; Swzarc, 2014). Specifically, the transition from the lower to middle stratigraphic interval was interpreted to record increasing accommodation, whereas the transition from the middle to upper interval was interpreted to record decreasing accommodation relative to sediment supply.

2D LAB Models: Constant Avulsion Frequency

Early numerical models of alluvial architecture predict that, during periods of low accommodation, the combination of reduced aggradation rates with comparatively higher rates of lateral migration allows channels to cannibalize much of their coeval fine-grained floodplain deposits, thereby increasing NTG, grain size, and channel amalgamation/clustering (Bridge and Leeder, 1979). Conversely, higher aggradation rates (i.e., driven by increased accommodation) coupled with reduced stream gradients increase the preservation potential of fine-grained overbank deposits. This preservation reduces NTG, grain size, and isolates channel sandstone bodies.

Given the influence of accommodation and sediment supply on the magnitude of the aggradation rate, changes in stacking patterns of channel-belts may have been controlled by changes in the aggradation rate assuming constant avulsion frequency, as predicted by early numerical models of alluvial architecture (Bridge and Leeder, 1979). Therefore, trends of decreasing channel-belt clustering from the lower to middle depositional units (i.e., DU-2 to DU-4) may reflect increasing aggradation rates as indicated by corresponding decreases in NTG, grain size, and channel-belt width (Figure 16). Conversely, increasing channel-belt clustering in the upper depositional units (i.e., DU-5 to DU-6) is interpreted to reflect decreasing aggradation rates as indicated by corresponding increases in NTG and grain size (Figure 16).

Experimental and 2D Models: Variable Avulsion Frequency

Experimental and numerical models of alluvial architecture published after the LAB models have shown that the relationship between sand body density/clustering and aggradation rate is not always negative, as it can significantly depend on avulsion frequency (Bryant et al., 1995; Heller and Paola, 1996). High avulsion frequencies force channels to switch faster leading to more efficient cannibalization of overbank deposits and a higher stacking density. Unlike the LAB models where avulsion frequency is held constant, later experimental and numerical models suggest three regimes are possible where avulsion frequency can increase linearly, slower than linearly, or faster than linearly with aggradation rate (Bryant et al., 1995; Heller and Paola, 1996). Depending on the operating regime, aggradation rate and sand body density may be negatively related, positively related (i.e., exact opposite of LAB model predictions), or completely independent (Figure 17). The additional complexity introduced by these models is also

apparent in many ancient fluvial successions where temporal variations in aggradation rate do not always relate to changes in channel-body density (Colombera et al., 2015). Therefore, temporal changes in avulsion frequency have to be taken into account including those induced by changes in variables like backwater hydraulics and bed-slope.

To this end, clustering trends in west Bull Canyon are compared to trends in different hydraulic and morphological parameters (Figure 18) that were estimated for depositional units in west Bull Canyon using a series of empirical equations derived from laboratory flume studies and observations from modern river systems (Turner, 2014). One of the reconstructed parameters, the backwater length, can help determine whether fluvial strata in west Bull Canyon were deposited within the backwater zone. The backwater zone is a zone that extends some distance upstream from the shoreline within which rivers behave differently because of the effect of static water in the receiving basin (Chow, 1959). Rivers entering the backwater zone decelerate and straighten as stream power and bank erodibility decrease (Chatanantavet et al., 2012). Flow deceleration (coupled with slope decrease) near the upstream extent of the backwater zone also increases aggradation rates and shortens the time period required to super-elevate channels above their floodplains which translates into a higher avulsion frequency (Chatanantavet et al., 2012).

Therefore, the backwater length is used as a predictor of changes in avulsion frequency. Hence, decreasing channel-belt clustering from DU-2 to DU-4 may reflect decreasing avulsion frequency associated with the trend of decreasing backwater length during this interval (Figure 18). The shortening of the backwater length is also evidenced by increases in paleo-slope and channel sinuosity during deposition of these units in west

Bull Canyon (Figure 18). Similarly, widening of the backwater zone in the upper interval (DU-5 to DU-6) brings channels closer to backwater hydraulic conditions as evidenced by decreased average channel slope and sinuosity. Therefore, this transition may have increased aggradation rates, and hence avulsion frequency, as suggested by increasing levels of channel-belt clustering in the upper interval (Figure 18). While high aggradation rates are expected to produce isolated channel-belt deposits in the LAB models, increased levels of clustering in this interval suggests a regime where avulsion frequency increases faster than linearly with backwater-mediated increases in aggradation rate (Figure 17, case 3).

3D Model: Autogenic Avulsion Sequence

Cyclic variations in stacking density and connectivity of channel-belt sandstone bodies can also be related to their distance from nodal avulsion points, as predicted by the avulsion sequence model (Mackey and Bridge, 1995). Upstream of nodal avulsion points, channel-belt deposits are isolated, have low width-to-thickness ratios, and are produced by a single aggrading channel. Downstream of nodal avulsion points, channel-belts diverge, have larger width-to-thickness ratios, and result in densely stacked and more connected sandstone bodies (Mackey and Bridge, 1995). This model therefore predicts that an autogenic upstream migration of a nodal avulsion point can produce an autogenic avulsion sequence consisting of isolated channel-belt deposits at the base overlain by progressively thinner and laterally amalgamated deposits towards the top of the succession (Figure 19). Changes in channel-belt stacking patterns in this model are solely dependent on the intrinsic movement of nodal avulsion points and do not invoke any changes in external controls. Modern observations suggest that the lengths of avulsive

distributary channels scale with the backwater length indicating nodal avulsion points can be backwater mediated (Jerolmack and Swenson, 2007; Ganti et. al., 2014).

We use changes in the reconstructed backwater length as a proxy variable for changes in the position of the nodal avulsion point. Hence, decreased backwater length in the lower to middle interval (from DU-2 to DU-4) reflects the downstream migration of the nodal avulsion point which reduces the stacking density and connectivity of channel-belt sandstone bodies. This is suggested by decreasing levels of channel-belt clustering throughout this interval (Figure 18). Conversely, increased backwater length in the upper interval reflects the upstream migration of the nodal avulsion point and its increasing distance from channels downstream. This results in the progressive lateral dispersion of channel-belt deposits and higher stacking densities as suggested by increasing levels of channel-belt clustering in the upper interval (Figure 18).

Models of Compensational Stacking and Channel Persistence

Experimental and numerical models of compensational stacking showed that depositional geometries tend to be controlled by the local configuration of the transport system over the short-term and shift towards subsidence-controlled compensation stacking above the compensational time scale (Straub et al., 2009; Wang et al., 2011). This scale is set by the time required for the transport system to visit every spot in the basin repeatedly thereby reducing the variability in the ratio of sedimentation to subsidence across the basin (Straub et al., 2009). Hence, over long enough time scales, compensational stacking moves the active depocenter uniformly across the basin. Over short time scales, autogenic processes like avulsion reoccupation can lead to anticompensation and channel persistence. Cellular models of avulsion showed that

channel reoccupation generates clustered multistory sandstone bodies as abandoned river channels are preserved as topographic lows (Jerolmack and Paola, 2007). These lows serve as attractors for future avulsion paths until they are buried with sediment, or until a large scale avulsion moves the system to a new location within the basin (Jerolmack and Paola, 2007; Straub et al., 2009; Hajek et al, 2010).

The K-function based moving window shows that channel-belt sandstone bodies shift from being clustered at small scales to being uniformly distributed at larger scales (Figure 14). This transition is observed in all depositional units of all studied outcrops and occurs over scales ranging from 50 to 130 m. Therefore, we interpret the observed small-scale clustering to reflect short-term channel reoccupation and persistence (i.e., anticompensation) within a topographic low while the larger scale pattern of uniformity is attributed to major shifts in the basin depocenter as a result of externally-forced compensational stacking. This interpretation suggests that the spatial distribution of channel-belts can record both autogenic and allogenic signals when their spatial and temporal scales do not overlap.

Limitations of Point Pattern Analysis

Point pattern analysis techniques have been used to characterize the spatial organization of channel-belts in the fluvial JHM and infer the processes underlying these patterns. For instance, processes that result in clustered channel-belts are expected to be different from those that generate uniform or random patterns. To make that distinction, channel-belt stacking patterns are measured using different techniques and contrasted with null models derived from specific assumptions about spatial randomness. However, since random patterns (i.e., patterns that confirm the null hypothesis) are patterns with no

predictable correlation in time and space, they cannot be tied to any specific underlying physical process. In addition, a random process can and will occasionally produce patterns that resemble those produced by deterministic processes. For instance, deposits produced from random processes will occasionally occur in topographic lows and will therefore appear to be driven by compensation (Straub et al., 2009). While observed patterns can be used to infer underlying processes, our approach does not guarantee a perfect one-to-one relationship between process and product.

The use of point pattern analysis techniques also incurs a significant loss of information associated with the transformation of complex 2D architectural elements (e.g., channel-belts) into individual points (e.g., channel-belts center points). This loss of information can occasionally cause misleading results when the dimensions of channel-belts are large in comparison to the investigated spatial scales. This is especially true in our case given the large lateral extent of channel-belts relative to the dimensions of target outcrops (Figure 20).

Figure 16 – Summary of up-section trends in different architectural parameters in east Bull Canyon. These include a trend of decreasing net to gross, D50 bedload, and average channel-belt from DU-2 to DU-3 and a trend reversal from DU-5 to DU-6. Similar trends are observed in channel-belt clustering (data from Pettinga, 2012).

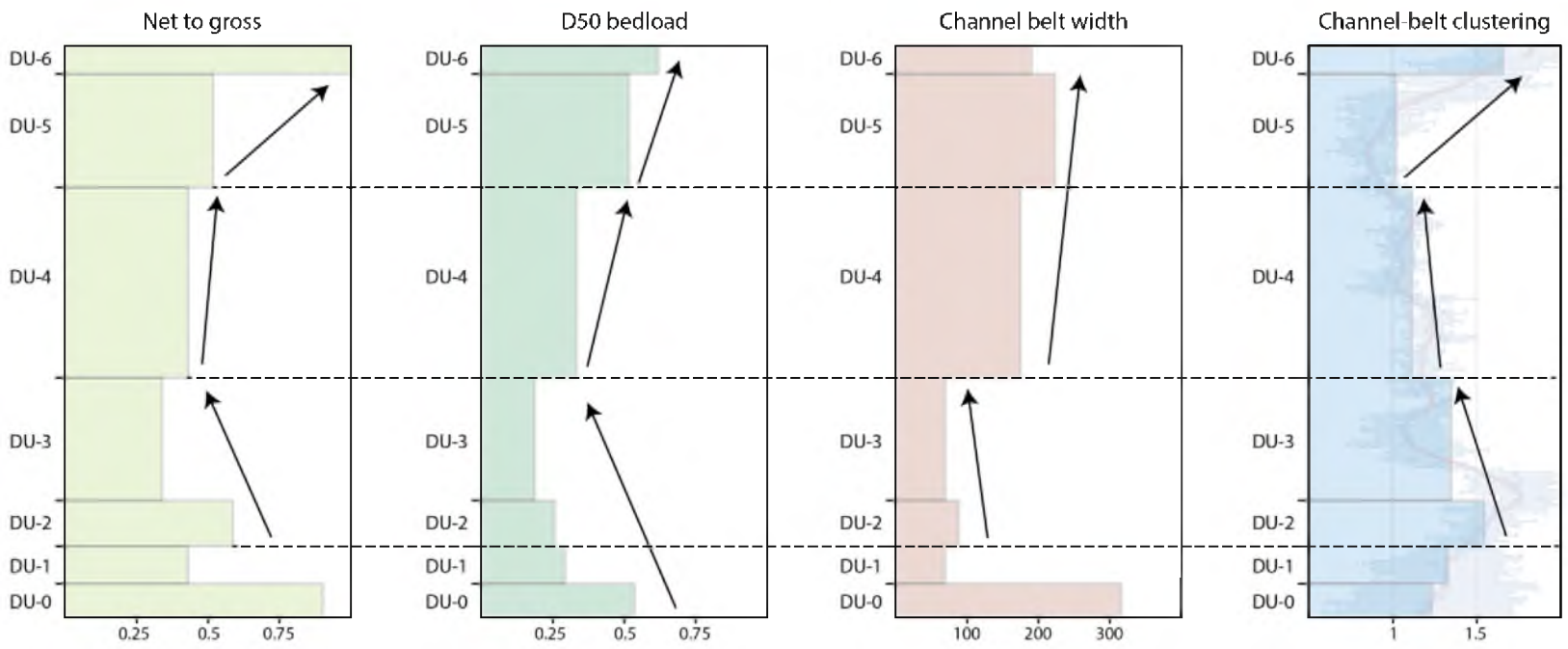
Net to gross
D50 bedload
Channel belt width
Channel-belt clustering
DU-6
DU-5
DU-4
DU-3
DU-2
DU-1
DU-0
0.25
0.5
0.75
100
200
300
1
1.5

Figure 17 – Diagrams showing how the relationship between channel-belt stacking density and aggradation rate varies depending on the exponent Beta (modified from Bryant et al., 1995). The exponent Beta governs the power law relation between avulsion frequency and aggradation rate. (1) When Beta < 1, avulsion frequency increases slower than linearly with aggradation rate indicating an inverse relationship between aggradation rate and channel-belt stacking density (original LAB relationship). (2) When Beta = 1, aggradation rate is linearly related to avulsion frequency indicating stacking density is independent of aggradation rate. (3) When Beta > 1, avulsion frequency increases faster than linearly with aggradation rate indicating a positive relationship between aggradation rate and channel-belt stacking density.

3
2
CASE 3 (β >1)
CASE 2 (β = 1)
increasing
aggradation rate
increasing
aggradation rate

Avulsion Frequency = Aggradation rate$^{\beta}$

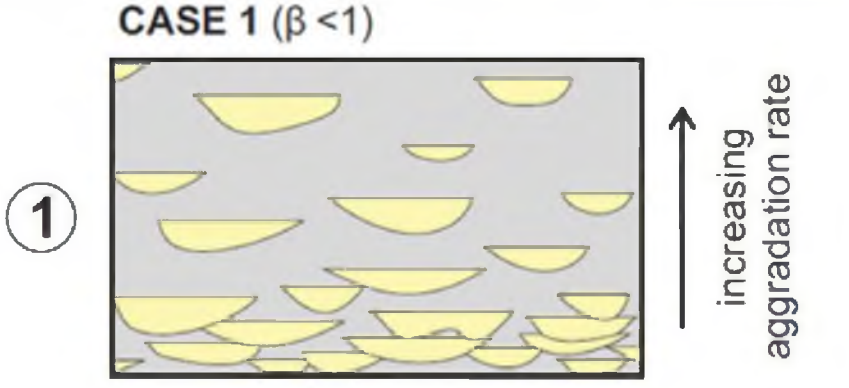

Figure 18 – Correlation of channel-belt clustering with different reconstructed paleo-hydraulic parameters. Trends of decreasing backwater length from DU-2 to DU-3 are associated with trends decreasing channel-belt clustering and increasing paleo-slope and sinuosity. Similarly, increasing backwater length from DU-5 to DU-6 is associated with increasing channel-belt clustering and decreasing sinuosity and paleo-slope. These trends indicate backwater influence is positively correlated with channel-belt clustering (data from Turner, 2014).

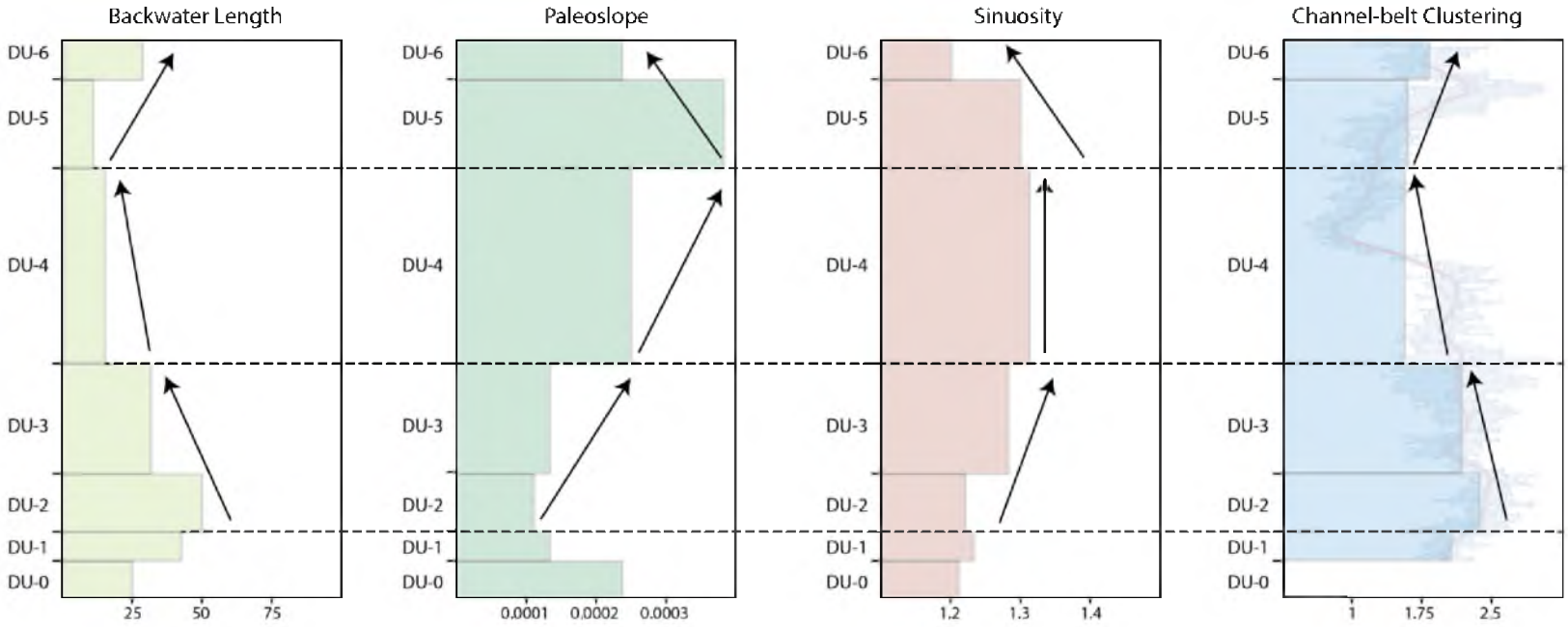
Backwater Length
Paleoslope
Sinuosity
Channel-belt Clustering
DU-6
DU-5
DU-4
DU-3
DU-2
DU-1
DU-0
25
50
75
0.0001
0.0002
0.0003
1.2
1.3
1.4
1
1.75
2.5

Figure 19 – Schematic cross section showing an avulsion succession composed of many avulsion sequences, as predicted by Mackey and Bridge (1995). Each avulsion sequence consists of thick and restricted channel-belt deposits at the base that grade upward into thinner and more dispersed channel-belt deposits. This avulsion sequence is the result of the gradual up-valley migration of a nodal avulsion point, as shown in simulations of a 3D model of alluvial stratigraphy (modified from Mackey and Bridge, 1995).

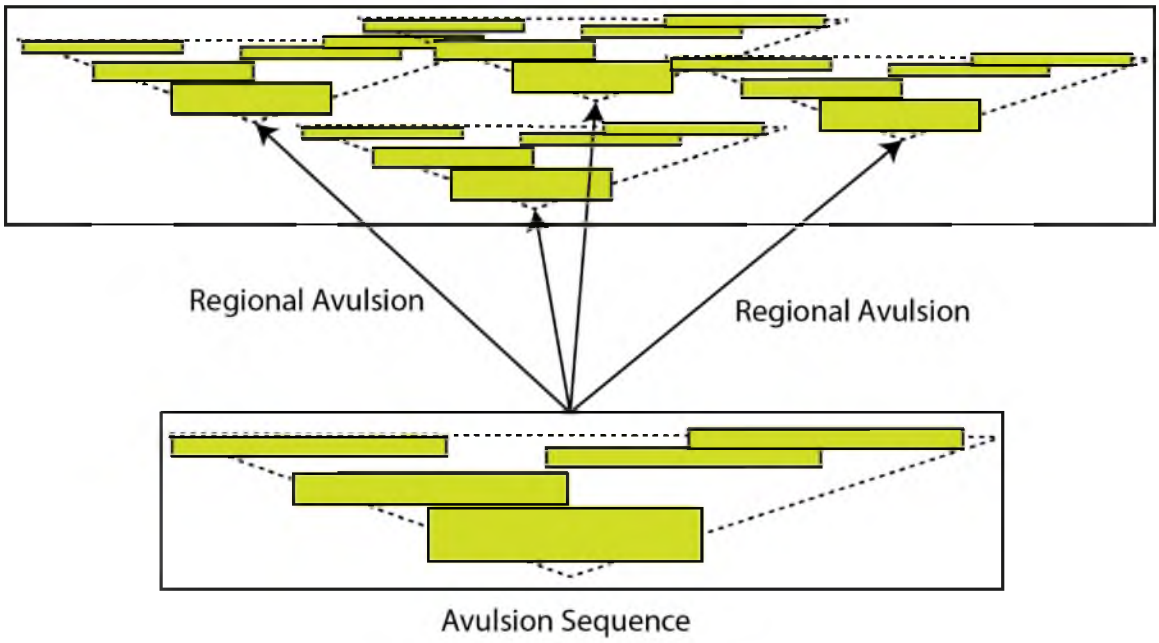

Avulsion Sequence

Figure 20 – Loss of information associated with the use of point pattern analysis techniques can lead to misleading results. In the figure, originally amalgamated and clustered channel-belts might be interpreted as uniform channel-belts after the transformation.

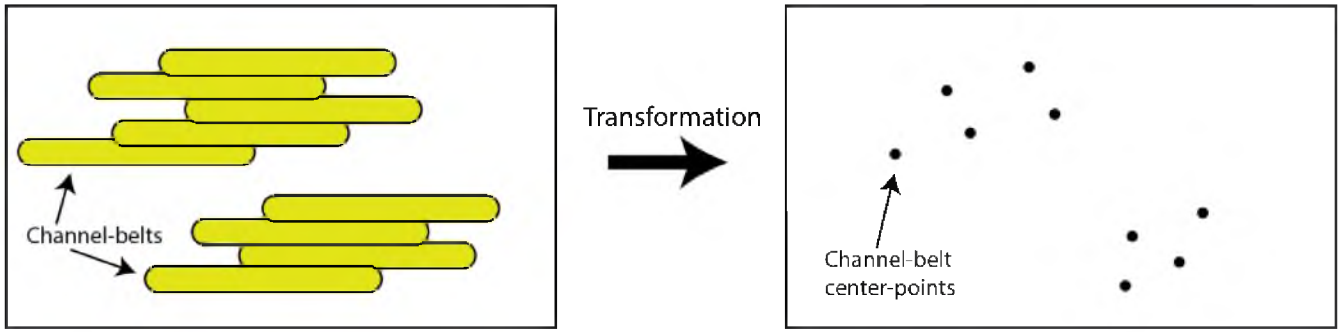
Channel-belts
Transformation
Channel-belt
center-points

CONCLUSION

Point pattern analysis techniques were used to perform a quantitative characterization of the stacking patterns and stratigraphic arrangement of channel-belt sandstone bodies in the fluvial John Henry Member of the Straight Cliffs Formation. The analysis was based on GPS coordinates of channel-belt center-points collected from three different outcrops of the fluvial JHM: (1) northwest Rock House Cove, (2) east Bull Canyon, and (3) west Bull Canyon. The analysis reveals two general trends in channel-belt stacking patterns starting with: (1) a trend of decreasing channel-belt clustering from DU-2 to DU-4, and (2) a trend of increasing clustering from DU-5 to DU-6. In addition, a correlation analysis based on dynamic time warping suggests clustering trends measured in the three outcrops exhibit strong similarities. The existence of overall comparable channel-belt stacking patterns in outcrops separated by distances upward of 18km suggests they were controlled by changing allogenic conditions.

More specifically, significant channel-belt clustering is interpreted to reflect the combined influence of low aggradation rates driven by reduced accommodation, high avulsion frequency where channels are influenced by backwater hydraulics (e.g., reduced slope and bank erodibility), and deposition downstream of a nodal avulsion point. The influence of the aggradation rate is evidenced by the negative relationship between channel-belt clustering and accommodation, as indicated by different architectural parameters including NTG, grain size, and amalgamation. Similarly, the impact of

backwater hydraulics and/or the location of the nodal avulsion point on stacking patterns is evidenced by the positive relationship between channel-belt clustering and the reconstructed backwater length (Turner, 2014).

Whereas overall stacking patterns are interpreted to be predominantly controlled by allogenic forcing, the K-function analysis reveals the existence of different patterns at different scales: (1) small scale clustering, and (2) large scale uniformity. The small-scale clustering is interpreted to be the product of avulsion reoccupation, an autogenic process where the preservation of abandoned channels as topographic lows within the floodplain leads to channel persistence and anticompensation. On the other hand, the large-scale uniformity is interpreted to be the product of externally-forced compensational stacking: the periodic reconfiguration of depositional systems towards topographic lows. This result implies that the preservation of patterns produced by autogenic processes is possible when their spatial scales do not overlap with those of allogenic processes.

APPENDIX A

DIFFERENTIAL GPS DATA

GPS Point Data

Channel-belt GPS points were collected using a differential GNSS combined with a laser range finder. GPS easting and northing coordinates are referenced to the NAD83 coordinate system and UTM zone 12N. Elevation is recorded in meters above mean sea level (MSL). In Table A.1 and Table A.2, sandstone bodies are assigned a unique identifier (SS body) and the location of a GPS point relative to its target sandstone body is documented in the side column. Table A.1 and Table A.2 list GPS points collected in west Bull Canyon (Turner, 2014) and Rock House Cove, respectively. GPS points collected in east Bull Canyon can be found in Pettinga's thesis manuscript (Pettinga, 2012).

Projected Channel-belt Center-Points

For each channel-belt, the center-point coordinates are calculated by averaging the coordinates of its lateral GPS points. Tables A.3 and A.4 list the coordinates of channel-belt center-points projected onto planes parallel to the outcrop orientation (parallel) and perpendicular to the average paleocurrent direction (perpendicular) in west Bull Canyon and Rock House Cove, respectively. Other columns include the sandstone body identifier (SS Body) and the depositional unit it belongs to (DU).

Table A.1

Sandstone Body GPS Points in west Bull Canyon

X	Y	MSL	SS Body	Side
436606.01	4119756.47	1522.82	1	Top
436597.46	4119743.69	1522.21	1	Top
436592.71	4119737.90	1524.49	1	Top
436586.24	4119733.56	1525.00	1	Top
436586.29	4119727.27	1522.80	1	Left
436591.29	4119731.02	1520.41	1	Base
436598.03	4119733.16	1518.85	1	Base
436600.61	4119738.56	1517.78	1	Base
436604.38	4119743.54	1518.62	1	Base
436609.44	4119749.08	1519.32	1	Base
436615.51	4119757.24	1519.98	1	Right
436551.84	4119718.23	1534.37	2	Right
436555.64	4119708.67	1533.75	2	Base
436556.59	4119700.95	1530.27	2	Base
436549.67	4119700.33	1534.16	2	Base
436544.29	4119688.53	1535.52	2	Left
436543.96	4119691.84	1535.65	2	Top
436544.84	4119700.35	1536.83	2	Top
436630.29	4119675.38	1496.38	3	Right
436635.32	4119659.78	1493.23	3	Base
436637.76	4119656.66	1492.19	3	Base
436633.64	4119649.23	1494.13	3	Base
436626.61	4119643.01	1493.54	3	Base
436624.32	4119632.39	1494.49	3	Base
436625.11	4119620.50	1495.29	3	Base
436626.55	4119614.04	1495.17	3	Base
436623.70	4119626.02	1496.24	3	Left
436622.89	4119636.12	1497.27	3	Top
436625.39	4119639.44	1498.05	3	Top
436628.51	4119640.84	1496.07	3	Top
436630.29	4119645.99	1496.94	3	Top
436627.80	4119650.00	1496.20	3	Top
436707.00	4119867.48	1526.12	4	Right
436688.71	4119829.59	1522.83	4	Base
436685.76	4119820.86	1519.87	4	Base
436677.16	4119817.24	1521.40	4	Base
436671.18	4119810.03	1521.64	4	Base
436662.63	4119804.04	1522.15	4	Base
436653.03	4119802.45	1523.00	4	Base
436637.91	4119797.96	1525.23	4	Base
436625.33	4119791.86	1525.24	4	Base

Table A.1 continued

X	Y	MSL	SS Body	Side
436616.30	4119774.43	1527.42	4	Base
436613.79	4119776.46	1526.75	4	Base
436602.25	4119768.12	1528.61	4	Base
436595.84	4119755.53	1529.83	4	Base
436579.98	4119741.53	1532.04	4	Base
436567.11	4119735.71	1535.32	4	Left
436570.47	4119740.13	1535.12	4	Top
436593.18	4119758.63	1534.23	4	Top
436596.53	4119764.92	1535.12	4	Top
436617.15	4119785.78	1532.68	4	Top
436628.59	4119804.40	1533.32	4	Top
436667.36	4119816.25	1528.81	4	Top
436677.39	4119824.49	1528.22	4	Top
436535.03	4119654.71	1539.19	5	Right
436534.95	4119647.21	1538.02	5	Base
436532.73	4119636.77	1538.12	5	Base
436526.52	4119625.58	1537.61	5	Base
436521.97	4119617.32	1539.15	5	Base
436511.69	4119608.18	1542.48	5	Left
436517.18	4119614.37	1542.96	5	Top
436521.79	4119622.70	1542.45	5	Top
436526.59	4119633.08	1540.90	5	Top
436529.85	4119644.55	1540.65	5	Top
436531.35	4119656.22	1540.67	5	Top
436517.32	4119662.57	1551.39	6	Right
436521.40	4119652.11	1547.34	6	Base
436520.85	4119647.79	1547.32	6	Base
436517.54	4119642.68	1549.87	6	Base
436509.78	4119632.47	1553.02	6	Left
436509.02	4119641.41	1555.51	6	Top
436514.87	4119648.46	1554.78	6	Top
436512.77	4119657.61	1552.99	6	Top
436490.08	4119496.87	1526.04	7	Right
436488.04	4119495.49	1523.96	7	Base
436493.23	4119484.62	1521.33	7	Base
436493.54	4119482.39	1521.35	7	Base
436497.61	4119469.20	1522.35	7	Base
436492.83	4119456.83	1525.23	7	Left
436490.15	4119467.99	1527.64	7	Top
436488.39	4119473.55	1528.89	7	Top
436486.45	4119479.06	1527.84	7	Top
436486.16	4119489.45	1528.87	7	Top

Table A.1 continued

X	Y	MSL	SS Body	Side
436489.38	4119546.96	1537.23	8	Right
436495.02	4119546.05	1533.22	8	Base
436488.57	4119533.23	1532.80	8	Base
436487.56	4119509.18	1534.22	8	Base
436484.82	4119497.39	1534.64	8	Base
436480.63	4119494.58	1539.80	8	Left
436477.65	4119496.56	1542.46	8	Top
436482.01	4119510.94	1540.62	8	Top
436484.96	4119521.53	1539.01	8	Top
436526.13	4119575.02	1537.51	9	Right
436527.86	4119573.95	1535.17	9	Base
436521.62	4119562.11	1532.63	9	Base
436519.86	4119556.71	1533.89	9	Base
436510.32	4119547.71	1536.06	9	Base
436502.59	4119537.40	1534.71	9	Base
436498.16	4119530.41	1536.38	9	Base
436481.00	4119521.23	1539.48	9	Left
436499.01	4119523.71	1539.75	9	Top
436507.02	4119544.23	1540.94	9	Top
436521.34	4119565.34	1539.16	9	Top
436658.59	4119554.91	1482.43	10	Right
436667.44	4119557.69	1480.49	10	Base
436672.52	4119554.58	1479.53	10	Base
436678.41	4119537.82	1477.81	10	Base
436676.07	4119530.34	1480.34	10	Base
436666.99	4119520.39	1479.85	10	Base
436660.28	4119518.00	1482.57	10	Left
436666.53	4119525.35	1482.35	10	Top
436673.69	4119535.05	1482.06	10	Top
436671.15	4119542.21	1481.30	10	Top
436281.70	4119345.74	1607.61	11	Right
436279.38	4119330.52	1604.87	11	Base
436266.80	4119322.16	1606.87	11	Base
436259.43	4119310.07	1607.08	11	Base
436243.29	4119309.89	1614.04	11	Left
436250.69	4119316.27	1615.54	11	Top
436260.08	4119327.02	1615.72	11	Top
436272.89	4119332.46	1610.17	11	Top
436280.21	4119340.21	1608.68	11	Top
436345.20	4119439.92	1601.42	12	Right
436342.88	4119433.87	1601.13	12	Base
436336.19	4119422.90	1602.35	12	Base

Table A.1 continued

X	Y	MSL	SS Body	Side
436331.58	4119413.98	1602.37	12	Base
436326.87	4119408.15	1603.87	12	Left
436329.96	4119415.86	1605.09	12	Top
436334.67	4119429.00	1605.69	12	Top
436340.06	4119435.49	1604.17	12	Top
436382.73	4119564.93	1592.51	13	Right
436381.92	4119544.52	1591.02	13	Base
436366.88	4119514.44	1592.03	13	Base
436360.59	4119483.85	1590.38	13	Base
436347.93	4119433.13	1592.63	13	Base
436324.68	4119392.99	1594.37	13	Base
436305.35	4119370.23	1599.11	13	Base
436291.52	4119354.44	1598.32	13	Base
436283.23	4119339.33	1598.20	13	Base
436276.72	4119322.50	1596.59	13	Base
436256.77	4119307.75	1600.11	13	Base
436243.01	4119298.76	1600.22	13	Base
436237.81	4119297.81	1604.87	13	Left
436251.42	4119304.94	1605.75	13	Top
436268.63	4119322.66	1605.20	13	Top
436283.41	4119337.20	1604.20	13	Top
436295.15	4119365.05	1604.56	13	Top
436325.74	4119394.44	1602.26	13	Top
436336.88	4119428.78	1601.93	13	Top
436345.44	4119452.58	1601.30	13	Top
436353.85	4119488.51	1597.92	13	Top
436362.91	4119519.97	1598.14	13	Top
436372.87	4119548.51	1597.95	13	Top
436401.49	4119564.84	1581.49	14	Right
436399.68	4119550.66	1578.30	14	Base
436396.85	4119537.84	1575.62	14	Base
436388.25	4119529.06	1576.79	14	Base
436382.57	4119515.39	1577.69	14	Base
436379.08	4119500.37	1578.99	14	Base
436372.73	4119479.94	1578.09	14	Base
436364.47	4119463.50	1579.39	14	Base
436363.17	4119446.17	1579.12	14	Base
436358.88	4119425.99	1580.17	14	Base
436345.55	4119400.08	1581.06	14	Base
436340.77	4119387.71	1580.79	14	Base
436337.76	4119373.68	1579.99	14	Base
436318.14	4119361.48	1586.74	14	Left

Table A.1 continued

X	Y	MSL	SS Body	Side
436325.03	4119372.27	1587.99	14	Top
436331.70	4119380.12	1588.04	14	Top
436351.06	4119419.18	1585.99	14	Top
436359.37	4119446.38	1585.84	14	Top
436368.67	4119477.17	1583.48	14	Top
436375.22	4119512.83	1585.89	14	Top
436389.04	4119542.18	1586.10	14	Top
436394.31	4119560.93	1584.29	14	Top
436298.61	4119424.12	1627.06	15	Right
436289.94	4119408.80	1623.14	15	Base
436276.66	4119389.92	1621.45	15	Base
436266.08	4119365.41	1624.05	15	Base
436257.75	4119345.25	1622.37	15	Base
436234.87	4119340.48	1630.16	15	Left
436250.88	4119351.60	1631.78	15	Top
436263.52	4119367.37	1630.56	15	Top
436275.03	4119394.82	1630.23	15	Top
436291.71	4119415.50	1628.97	15	Top
436278.10	4119362.21	1616.76	16	Right
436275.28	4119352.97	1614.52	16	Base
436265.00	4119348.13	1618.21	16	Left
436269.26	4119356.01	1619.87	16	Top
436284.77	4119372.08	1612.61	17	Right
436288.72	4119362.48	1608.29	17	Base
436281.64	4119353.85	1609.49	17	Base
436273.50	4119346.42	1612.28	17	Left
436276.50	4119356.62	1614.51	17	Top
436283.36	4119367.47	1613.64	17	Top
436369.55	4119501.75	1586.35	18	Right
436373.33	4119487.41	1583.16	18	Base
436367.16	4119478.27	1584.06	18	Base
436362.98	4119458.02	1585.84	18	Base
436359.11	4119439.27	1586.85	18	Left
436361.05	4119457.11	1589.10	18	Top
436362.49	4119472.55	1589.19	18	Top
436366.89	4119488.63	1587.82	18	Top
436380.94	4119414.77	1564.09	19	Right
436382.15	4119407.40	1562.01	19	Base
436378.05	4119402.98	1564.19	19	Left
436379.97	4119407.63	1566.11	19	Top
436375.63	4119395.75	1564.77	20	Right
436373.78	4119388.28	1563.44	20	Base

Table A.1 continued

X	Y	MSL	SS Body	Side
436373.18	4119377.55	1563.27	20	Base
436360.59	4119365.95	1565.06	20	Base
436355.50	4119350.92	1564.79	20	Base
436342.32	4119335.18	1565.75	20	Base
436335.53	4119329.40	1567.87	20	Left
436339.51	4119339.77	1569.58	20	Top
436349.54	4119352.33	1569.14	20	Top
436354.79	4119364.77	1569.99	20	Top
436366.14	4119386.44	1567.79	20	Top
436351.83	4119376.21	1573.82	21	Right
436349.79	4119369.64	1572.69	21	Base
436343.17	4119363.10	1574.60	21	Base
436334.60	4119359.07	1577.40	21	Left
436336.83	4119366.66	1578.54	21	Top
436342.62	4119373.68	1576.88	21	Top
436306.47	4119295.15	1567.29	22	Right
436297.46	4119287.12	1568.12	22	Base
436291.56	4119280.04	1567.29	22	Base
436235.96	4119254.72	1570.43	22	Left
436244.90	4119262.40	1572.76	22	Top
436269.89	4119273.81	1573.29	22	Top
436286.90	4119282.83	1571.46	22	Top
436253.35	4119241.68	1558.94	23	Right
436254.14	4119234.83	1556.58	23	Base
436242.78	4119225.24	1555.78	23	Base
436239.44	4119224.54	1559.56	23	Left
436244.19	4119229.04	1560.66	23	Top
436251.09	4119237.12	1560.35	23	Top
436407.22	4119428.83	1547.24	23	Base
436407.56	4119411.58	1547.56	23	Base
436397.31	4119402.66	1550.35	23	Base
436393.67	4119385.54	1549.15	23	Base
436384.14	4119361.89	1551.32	23	Base
436371.57	4119346.36	1553.58	23	Base
436349.04	4119317.14	1556.52	23	Left
436350.12	4119325.46	1558.65	23	Top
436360.83	4119340.86	1558.22	23	Top
436381.20	4119367.52	1555.98	23	Top
436388.86	4119388.83	1554.85	23	Top
436399.83	4119415.13	1554.75	23	Top
436409.64	4119449.84	1553.87	23	Top
436416.97	4119456.96	1549.05	24	Right

Table A.1 continued

X	Y	MSL	SS Body	Side
436412.65	4119447.87	1547.79	24	Base
436415.52	4119440.91	1543.72	24	Right
436418.41	4119428.34	1539.90	24	Base
436423.16	4119405.89	1537.96	24	Base
436407.25	4119392.73	1542.10	24	Base
436399.53	4119368.60	1541.96	24	Base
436377.77	4119342.17	1545.05	24	Base
436365.03	4119314.67	1545.73	24	Base
436349.82	4119293.92	1546.98	24	Base
436326.88	4119271.99	1546.63	24	Base
436310.84	4119260.16	1549.72	24	Base
436310.52	4119246.23	1543.88	24	Base
436257.25	4119184.91	1546.41	24	Base
436240.43	4119187.09	1553.86	24	Left
436248.82	4119193.72	1554.16	24	Top
436282.17	4119211.80	1553.00	24	Top
436308.79	4119223.88	1552.79	24	Top
436316.06	4119235.18	1552.30	24	Top
436331.50	4119249.20	1552.67	24	Top
436346.51	4119271.46	1550.89	24	Top
436358.85	4119296.60	1551.07	24	Top
436372.44	4119328.15	1549.31	24	Top
436378.57	4119346.18	1546.90	24	Top
436387.30	4119390.65	1545.96	24	Top
436408.07	4119395.85	1534.88	25	Right
436409.14	4119385.50	1533.57	25	Base
436409.27	4119369.97	1533.59	25	Base
436403.39	4119361.79	1534.79	25	Base
436401.29	4119344.47	1534.43	25	Base
436391.27	4119333.76	1538.03	25	Left
436394.43	4119346.51	1539.25	25	Top
436399.76	4119364.32	1538.16	25	Top
436404.09	4119378.56	1537.07	25	Top
436406.94	4119391.09	1536.17	25	Top
436413.45	4119392.82	1530.27	26	Right
436413.81	4119385.65	1528.68	26	Right
436410.22	4119376.31	1529.24	26	Base
436411.66	4119362.95	1529.28	26	Base
436406.35	4119353.79	1529.48	26	Base
436400.05	4119338.49	1530.23	26	Base
436397.22	4119327.52	1531.51	26	Base
436396.20	4119308.16	1532.66	26	Base

Table A.1 continued

X	Y	MSL	SS Body	Side
436391.70	4119300.23	1533.11	26	Base
436375.05	4119278.95	1531.48	26	Base
436368.00	4119264.04	1533.06	26	Base
436346.28	4119227.79	1534.82	26	Base
436324.96	4119213.37	1537.31	26	Base
436302.74	4119202.81	1541.79	26	Left
436324.26	4119220.14	1541.03	26	Top
436353.01	4119246.12	1540.50	26	Top
436362.78	4119266.70	1539.96	26	Top
436374.63	4119291.75	1538.63	26	Top
436390.81	4119318.68	1536.11	26	Top
436393.98	4119333.61	1535.81	26	Top
436405.08	4119363.58	1533.74	26	Top
436411.80	4119386.74	1532.29	26	Top
436442.03	4119368.89	1513.78	27	Right
436443.55	4119360.95	1513.53	27	Base
436442.52	4119352.88	1511.59	27	Base
436438.97	4119343.04	1511.40	27	Base
436436.76	4119327.45	1512.04	27	Base
436477.49	4119301.60	1504.34	27	Base
436435.87	4119306.69	1514.30	27	Base
436434.85	4119306.33	1515.16	27	Left
436430.66	4119326.18	1516.55	27	Top
436431.58	4119341.70	1516.12	27	Top
436441.14	4119357.39	1515.73	27	Top
436477.85	4119309.13	1502.28	28	Right
436481.23	4119301.96	1500.59	28	Base
436475.95	4119293.09	1501.55	28	Base
436462.11	4119285.53	1504.19	28	Base
436458.41	4119277.58	1503.12	28	Base
436439.74	4119268.81	1505.99	28	Left
436446.20	4119276.43	1507.18	28	Top
436458.32	4119278.22	1507.01	28	Top
436461.64	4119288.90	1507.02	28	Top
436477.29	4119298.31	1504.14	28	Top
436478.87	4119305.44	1503.75	28	Top
436389.35	4119258.86	1520.81	29	Right
436393.53	4119249.23	1519.65	29	Base
436391.02	4119237.94	1521.27	29	Base
436381.12	4119230.45	1523.05	29	Left
436386.94	4119234.85	1523.53	29	Top
436388.80	4119247.08	1523.54	29	Top

Table A.1 continued

X	Y	MSL	SS Body	Side
436389.78	4119253.55	1522.80	29	Top
436395.83	4119245.90	1518.36	30	Right
436394.74	4119233.05	1517.47	30	Base
436381.66	4119224.45	1518.99	30	Base
436376.64	4119216.79	1518.27	30	Base
436360.83	4119207.44	1519.50	30	Base
436354.22	4119188.40	1521.38	30	Left
436354.82	4119197.73	1522.93	30	Top
436365.00	4119214.06	1522.78	30	Top
436381.41	4119225.98	1522.15	30	Top
436391.30	4119234.98	1519.66	30	Top
436515.87	4119430.71	1496.12	31	Right
436512.10	4119425.16	1494.63	31	Base
436505.62	4119409.19	1495.21	31	Base
436498.81	4119396.38	1496.84	31	Base
436481.33	4119386.87	1497.58	31	Base
436476.85	4119374.03	1497.79	31	Base
436473.93	4119364.33	1500.10	31	Base
436469.06	4119355.04	1501.42	31	Base
436463.77	4119342.31	1501.93	31	Left
436468.18	4119354.77	1503.56	31	Top
436471.35	4119365.07	1502.59	31	Top
436473.50	4119376.92	1501.94	31	Top
436488.25	4119392.70	1500.59	31	Top
436499.87	4119410.45	1500.11	31	Top
436506.01	4119425.18	1497.41	31	Top
436512.28	4119429.49	1497.09	31	Top
436509.39	4119310.18	1484.51	32	Right
436520.13	4119294.81	1483.26	32	Base
436514.02	4119282.94	1480.74	32	Base
436517.38	4119265.74	1477.93	32	Base
436514.36	4119254.78	1478.99	32	Base
436458.85	4119249.52	1483.82	32	Base
436451.25	4119226.62	1487.38	32	Base
436445.57	4119207.32	1491.05	32	Base
436417.05	4119196.91	1494.51	32	Left
436442.57	4119203.14	1493.38	32	Top
436445.18	4119221.10	1492.60	32	Top
436455.80	4119250.74	1489.83	32	Top
436500.21	4119252.40	1486.25	32	Top
436506.43	4119270.75	1486.13	32	Top
436514.26	4119290.19	1485.45	32	Top

Table A.1 continued

X	Y	MSL	SS Body	Side
436519.04	4119299.22	1485.29	32	Top
436299.91	4119151.11	1513.69	33	Right
436294.41	4119141.96	1513.70	33	Base
436282.61	4119130.20	1516.55	33	Base
436274.38	4119125.77	1519.73	33	Left
436281.26	4119135.64	1517.54	33	Top
436289.56	4119146.17	1517.10	33	Top
436293.62	4119133.96	1511.19	34	Right
436291.97	4119119.47	1510.71	34	Base
436267.44	4119091.02	1510.87	34	Base
436250.16	4119080.29	1513.45	34	Left
436265.94	4119097.43	1514.84	34	Top
436280.63	4119115.33	1513.37	34	Top
436285.55	4119125.93	1513.42	34	Top
436318.23	4119138.54	1501.63	35	Right
436306.65	4119121.06	1500.63	35	Base
436290.55	4119104.71	1501.12	35	Base
436276.94	4119089.65	1504.01	35	Left
436291.48	4119108.49	1504.55	35	Top
436306.53	4119125.41	1503.22	35	Top
436309.84	4119133.52	1503.56	35	Top
436438.89	4119178.13	1480.23	36	Right
436433.87	4119164.70	1478.26	36	Base
436408.45	4119141.12	1480.56	36	Base
436336.72	4119121.29	1489.38	36	Base
436288.42	4119081.52	1493.49	36	Base
436261.73	4119058.84	1497.74	36	Left
436293.56	4119088.86	1496.43	36	Top
436325.09	4119123.22	1495.69	36	Top
436432.41	4119164.66	1482.98	36	Top
436431.06	4119173.66	1481.81	36	Top
436424.47	4119178.82	1485.90	37	Right
436425.43	4119171.61	1485.14	37	Base
436421.67	4119166.25	1486.32	37	Left
436425.68	4119172.25	1487.14	37	Top
436412.47	4119136.72	1476.05	38	Right
436347.26	4119119.35	1480.99	38	Base
436312.05	4119106.98	1487.06	38	Left
436406.40	4119129.79	1478.13	38	Top
436506.12	4119153.97	1459.03	39	Right
436525.53	4119148.79	1456.20	39	Base
436533.56	4119140.18	1454.78	39	Base

Table A.1 continued

X	Y	MSL	SS Body	Side
436501.17	4119122.17	1457.53	39	Base
436468.28	4119095.41	1461.17	39	Left
436468.18	4119105.16	1462.82	39	Top
436489.61	4119125.63	1460.97	39	Top
436493.75	4119147.05	1460.47	39	Top
436547.79	4119155.20	1452.46	40	Right
436560.32	4119149.56	1450.08	40	Base
436559.96	4119145.25	1451.83	40	Left
436552.39	4119149.51	1452.22	40	Top
436525.59	4119274.35	1470.99	41	Right
436526.64	4119261.82	1469.94	41	Base
436519.33	4119247.17	1468.78	41	Base
436503.93	4119242.26	1470.29	41	Base
436501.47	4119242.82	1474.89	41	Left
436513.28	4119245.52	1473.57	41	Top
436523.97	4119251.72	1471.97	41	Top
436521.17	4119267.31	1471.78	41	Top
436572.29	4119262.99	1456.65	42	Right
436571.48	4119257.91	1456.14	42	Base
436571.32	4119247.79	1455.92	42	Base
436569.94	4119242.55	1457.59	42	Left
436566.79	4119249.62	1457.59	42	Top
436567.68	4119258.80	1457.73	42	Top
436616.70	4119226.02	1448.16	43	Right
436611.69	4119217.61	1448.67	43	Base
436594.35	4119211.59	1449.93	43	Base
436586.28	4119210.62	1453.05	43	Left
436596.89	4119213.72	1452.37	43	Top
436611.41	4119220.77	1449.78	43	Top
436604.70	4119298.95	1459.97	44	Right
436599.45	4119292.22	1459.29	44	Base
436577.65	4119289.15	1462.27	44	Left
436601.45	4119293.40	1460.82	44	Top
436502.52	4119416.77	1495.57	45	Right
436497.21	4119398.41	1494.53	45	Base
436476.29	4119373.67	1496.43	45	Base
436470.33	4119356.62	1497.93	45	Base
436463.86	4119340.13	1502.32	45	Base
436459.74	4119326.99	1500.68	45	Left
436462.13	4119345.33	1503.62	45	Top
436463.36	4119369.61	1502.63	45	Top
436491.33	4119397.75	1498.49	45	Top

Table A.1 continued

X	Y	MSL	SS Body	Side
436500.70	4119415.64	1496.96	45	Top
436517.47	4119379.21	1482.81	46	Right
436515.98	4119369.26	1478.00	46	Base
436534.03	4119345.88	1475.30	46	Base
436511.27	4119353.28	1482.87	46	Left
436504.11	4119369.87	1484.89	46	Top
436513.53	4119371.70	1483.36	46	Top
436604.82	4119397.75	1461.96	47	Right
436601.26	4119393.26	1460.83	47	Base
436594.34	4119389.39	1461.51	47	Base
436590.85	4119390.50	1463.30	47	Left
436599.54	4119392.90	1462.45	47	Top
436493.05	4119740.75	1580.10	48	Right
436491.99	4119723.66	1576.24	48	Base
436487.47	4119710.04	1575.67	48	Base
436483.75	4119695.27	1574.82	48	Base
436485.49	4119673.49	1569.16	48	Base
436463.39	4119637.73	1571.67	48	Base
436446.24	4119626.90	1572.15	48	Base
436446.10	4119624.43	1571.89	48	Base
436424.61	4119595.82	1575.90	48	Base
436417.72	4119585.83	1580.15	48	Left
436426.03	4119607.07	1583.60	48	Top
436449.30	4119634.84	1583.30	48	Top
436468.22	4119666.56	1582.22	48	Top
436479.59	4119689.58	1581.55	48	Top
436487.39	4119713.04	1579.66	48	Top
436490.54	4119723.75	1579.22	48	Top
436487.47	4119729.45	1580.11	49	Right
436486.94	4119714.40	1579.18	49	Base
436478.69	4119688.28	1581.60	49	Base
436471.34	4119680.17	1583.75	49	Left
436476.72	4119692.55	1585.41	49	Top
436486.87	4119712.47	1583.19	49	Top
436519.60	4119763.56	1570.33	50	Right
436515.98	4119751.32	1566.12	50	Base
436501.15	4119733.66	1566.63	50	Base
436500.13	4119719.97	1566.14	50	Base
436489.08	4119706.84	1568.77	50	Base
436487.27	4119700.37	1573.96	50	Left
436491.06	4119714.24	1576.38	50	Top
436497.95	4119734.27	1575.12	50	Top

Table A.1 continued

X	Y	MSL	SS Body	Side
436506.83	4119750.04	1575.38	50	Top
436518.80	4119757.43	1572.69	50	Top
436520.43	4119762.66	1570.85	50	Top
436608.79	4119864.63	1556.29	51	Right
436602.03	4119843.88	1553.87	51	Base
436568.03	4119827.39	1557.48	51	Base
436552.25	4119794.83	1558.78	51	Base
436537.81	4119768.55	1560.39	51	Base
436523.61	4119755.94	1562.25	51	Base
436509.23	4119738.02	1562.54	51	Base
436501.32	4119722.03	1564.69	51	Left
436496.66	4119729.12	1565.13	51	Top
436519.90	4119755.15	1566.21	51	Top
436538.82	4119784.30	1565.00	51	Top
436545.31	4119808.79	1563.47	51	Top
436572.41	4119832.84	1561.66	51	Top
436592.73	4119846.42	1559.11	51	Top
436605.41	4119863.42	1548.54	52	Right
436603.87	4119834.01	1545.10	52	Base
436589.28	4119822.10	1547.11	52	Base
436558.89	4119810.02	1550.44	52	Base
436548.95	4119782.11	1552.03	52	Base
436538.77	4119760.31	1553.93	52	Base
436522.14	4119746.12	1556.74	52	Left
436537.12	4119763.27	1557.25	52	Top
436546.76	4119801.40	1556.74	52	Top
436559.49	4119818.92	1556.43	52	Top
436595.91	4119836.10	1550.75	52	Top
436602.77	4119844.50	1549.74	52	Top
436502.03	4119873.02	1610.59	53	Right
436495.85	4119863.66	1608.50	53	Base
436478.09	4119851.78	1608.07	53	Base
436462.20	4119852.04	1606.91	53	Base
436458.00	4119852.25	1610.97	53	Left
436466.58	4119854.54	1614.09	53	Top
436487.34	4119857.32	1613.88	53	Top
436494.80	4119864.98	1613.19	53	Top
436464.22	4119838.32	1599.49	54	Right
436462.33	4119808.79	1600.05	54	Left
436466.08	4119829.28	1601.41	54	Top
436454.25	4119818.17	1607.69	55	Right
436451.19	4119809.19	1607.53	55	Base

Table A.1 continued

X	Y	MSL	SS Body	Side
436462.84	4119780.46	1604.08	55	Left
436449.91	4119813.10	1612.76	55	Top
436455.38	4119779.92	1607.66	56	Right
436456.69	4119763.24	1605.87	56	Base
436445.01	4119753.34	1607.65	56	Base
436435.00	4119730.90	1612.66	56	Left
436437.28	4119746.98	1614.31	56	Top
436446.47	4119763.80	1613.42	56	Top
436433.17	4119721.41	1612.25	57	Right
436430.15	4119707.66	1612.41	57	Base
436425.28	4119694.39	1612.29	57	Base
436423.76	4119682.32	1611.56	57	Base
436416.52	4119680.64	1614.34	57	Left
436421.84	4119699.63	1617.13	57	Top
436430.16	4119714.97	1615.71	57	Top
436668.74	4119790.99	1507.63	58	Right
436659.43	4119781.79	1507.70	58	Base
436652.71	4119776.85	1508.89	58	Left
436662.84	4119788.83	1509.84	58	Top
436686.92	4119774.50	1496.12	59	Right
436682.15	4119764.75	1494.57	59	Base
436678.79	4119759.90	1493.56	59	Base
436674.03	4119755.20	1493.92	59	Base
436654.78	4119745.35	1495.96	59	Base
436640.81	4119736.50	1496.62	59	Base
436631.15	4119725.96	1498.13	59	Base
436625.18	4119716.08	1500.70	59	Left
436631.05	4119730.43	1500.62	59	Top
436644.31	4119747.66	1500.99	59	Top
436669.60	4119756.73	1498.98	59	Top
436681.52	4119767.47	1497.62	59	Top
436625.09	4119707.18	1500.24	60	Right
436621.90	4119699.53	1499.64	60	Base
436604.39	4119689.19	1502.09	60	Left
436614.86	4119695.72	1502.40	60	Top
436621.46	4119700.11	1501.63	60	Top
436587.12	4119734.40	1521.23	61	Right
436582.98	4119724.52	1519.62	61	Base
436575.04	4119713.10	1519.74	61	Base
436569.93	4119701.05	1519.51	61	Base
436564.56	4119698.84	1523.45	61	Left
436567.22	4119708.52	1524.45	61	Top

Table A.1 continued

X	Y	MSL	SS Body	Side
436572.60	4119720.66	1524.73	61	Top
436579.37	4119729.60	1524.45	61	Top
436578.97	4119575.96	1505.43	62	Right
436581.65	4119568.65	1503.75	62	Base
436570.49	4119564.41	1504.18	62	Base
436557.08	4119563.65	1506.47	62	Left
436565.44	4119564.50	1506.77	62	Top
436578.08	4119571.70	1506.27	62	Top
436561.43	4119581.15	1512.40	63	Right
436560.75	4119575.88	1511.43	63	Base
436549.98	4119576.31	1513.41	63	Left
436558.66	4119577.57	1513.67	63	Top
436515.39	4119558.10	1519.08	64	Right
436505.31	4119554.63	1518.81	64	Base
436500.40	4119543.75	1518.36	64	Base
436493.90	4119535.23	1520.43	64	Left
436498.27	4119547.78	1522.32	64	Top
436504.17	4119555.70	1521.68	64	Top
436639.35	4119573.32	1488.43	65	Right
436640.31	4119557.52	1484.65	65	Base
436639.90	4119533.69	1485.67	65	Base
436627.13	4119531.82	1488.39	65	Base
436617.99	4119532.77	1490.81	65	Left
436631.58	4119533.79	1489.08	65	Top
436633.61	4119546.59	1488.95	65	Top
436635.19	4119563.24	1488.87	65	Top
436618.34	4119627.01	1494.13	66	Right
436621.61	4119615.53	1493.05	66	Base
436613.37	4119607.99	1494.87	66	Base
436616.89	4119592.49	1494.33	66	Base
436612.29	4119586.89	1496.91	66	Left
436608.94	4119601.26	1497.88	66	Top
436614.38	4119610.40	1497.04	66	Top
436618.11	4119618.44	1496.33	66	Top
436669.75	4119578.96	1477.94	67	Base
436660.97	4119570.80	1480.20	67	Base
436654.61	4119563.62	1481.15	67	Base
436648.05	4119564.23	1483.29	67	Left
436655.01	4119567.25	1482.70	67	Top
436663.33	4119574.97	1481.99	67	Top
436682.04	4119588.86	1472.17	68	Right
436683.82	4119580.75	1470.99	68	Base

Table A.1 continued

X	Y	MSL	SS Body	Side
436681.57	4119576.65	1471.98	68	Left
436682.74	4119582.28	1472.35	68	Top
436712.65	4119526.47	1467.43	69	Right
436709.21	4119521.44	1466.27	69	Base
436698.11	4119521.15	1467.08	69	Base
436692.05	4119518.85	1467.29	69	Base
436685.84	4119516.37	1467.47	69	Base
436681.52	4119514.41	1469.40	69	Left
436683.43	4119519.42	1469.83	69	Top
436694.82	4119523.09	1469.11	69	Top
436709.90	4119524.26	1467.84	69	Top
436679.28	4119509.15	1469.68	70	Right
436679.40	4119502.26	1469.28	70	Base
436674.53	4119495.54	1469.52	70	Base
436669.26	4119490.10	1468.65	70	Base
436631.99	4119494.59	1471.58	70	Base
436623.68	4119493.81	1474.05	70	Left
436629.65	4119499.36	1474.74	70	Top
436672.75	4119495.89	1471.02	70	Top
436676.46	4119504.93	1470.99	70	Top
436679.38	4119509.11	1470.29	70	Top
436731.35	4119501.69	1460.57	71	Right
436728.02	4119499.98	1460.32	71	Base
436720.16	4119500.46	1461.29	71	Left
436727.41	4119500.94	1461.15	71	Top
436691.96	4119489.31	1464.09	72	Right
436691.96	4119486.62	1463.43	72	Base
436686.64	4119483.98	1463.89	72	Left
436689.96	4119486.71	1464.22	72	Top
437134.97	4120346.91	1473.45	73	Right
437133.57	4120334.56	1473.57	73	Base
437124.31	4120327.52	1473.88	73	Left
437127.96	4120331.76	1474.15	73	Top
437131.48	4120340.19	1473.82	73	Top
437159.98	4120337.89	1473.89	74	Right
437164.78	4120330.86	1474.03	74	Base
437142.16	4120327.84	1471.28	74	Base
437136.83	4120319.04	1471.84	74	Base
437134.95	4120311.16	1472.25	74	Base
437127.06	4120299.96	1472.56	74	Left
437130.36	4120305.93	1473.39	74	Top
437132.95	4120312.86	1473.58	74	Top

Table A.1 continued

X	Y	MSL	SS Body	Side
437134.04	4120321.90	1473.12	74	Top
437142.21	4120335.37	1473.19	74	Top
437251.87	4120354.06	1467.90	75	Right
437245.37	4120347.87	1466.85	75	Base
437238.67	4120344.55	1467.91	75	Base
437218.57	4120347.96	1467.42	75	Base
437210.43	4120346.05	1468.62	75	Base
437201.63	4120340.72	1468.76	75	Base
437199.42	4120330.63	1467.97	75	Base
437196.56	4120321.45	1469.02	75	Base
437181.22	4120313.65	1468.73	75	Base
437165.80	4120313.22	1469.86	75	Left
437177.33	4120317.58	1471.21	75	Top
437194.32	4120321.79	1470.73	75	Top
437195.33	4120332.72	1470.60	75	Top
437202.56	4120345.43	1470.72	75	Top
437211.07	4120355.58	1469.85	75	Top
437237.19	4120347.28	1469.20	75	Top
437246.25	4120351.15	1468.38	75	Top
437249.73	4120354.35	1468.08	75	Top
437195.51	4120367.55	1473.63	76	Right
437193.75	4120362.36	1473.22	76	Base
437181.11	4120355.99	1473.81	76	Left
437190.92	4120363.77	1474.15	76	Top
437221.96	4120371.28	1473.20	77	Right
437215.86	4120369.67	1472.95	77	Base
437205.91	4120369.37	1473.43	77	Left
437212.51	4120372.33	1473.62	77	Top
437247.59	4120379.84	1472.16	78	Right
437245.44	4120375.88	1472.50	78	Base
437241.12	4120374.14	1472.76	78	Base
437235.06	4120370.71	1472.57	78	Base
437225.85	4120369.99	1472.95	78	Left
437233.89	4120373.24	1473.39	78	Top
437240.69	4120375.92	1474.06	78	Top
437243.70	4120377.17	1473.27	78	Top
437209.60	4120376.17	1474.74	79	Right
437204.67	4120374.69	1474.28	79	Base
437195.36	4120375.77	1474.10	79	Left
437199.03	4120377.02	1474.85	79	Top
437211.69	4120397.46	1477.69	80	Right
437207.67	4120396.26	1477.39	80	Base

Table A.1 continued

X	Y	MSL	SS Body	Side
437200.50	4120395.59	1478.09	80	Base
437195.15	4120396.29	1478.94	80	Left
437202.60	4120399.87	1478.96	80	Top
437234.67	4120408.26	1475.93	81	Right
437233.17	4120405.96	1475.92	81	Base
437229.59	4120402.17	1476.21	81	Base
437218.81	4120397.80	1477.05	81	Base
437212.76	4120397.36	1477.76	81	Left
437217.10	4120401.11	1477.96	81	Top
437230.13	4120405.08	1476.88	81	Top
437261.58	4120478.56	1476.02	82	Right
437257.55	4120475.15	1476.01	82	Base
437250.73	4120468.95	1475.58	82	Base
437241.22	4120465.40	1476.06	82	Base
437228.00	4120464.85	1477.47	82	Base
437220.93	4120466.23	1478.83	82	Base
437213.39	4120462.10	1478.10	82	Base
437208.89	4120458.37	1478.96	82	Base
437207.09	4120451.26	1478.74	82	Base
437203.20	4120428.85	1480.96	82	Base
437191.85	4120416.39	1483.03	82	Base
437171.10	4120409.66	1484.93	82	Left
437186.42	4120417.33	1485.50	82	Top
437198.90	4120430.05	1483.89	82	Top
437200.49	4120451.50	1483.62	82	Top
437208.19	4120462.72	1482.59	82	Top
437228.50	4120468.88	1481.47	82	Top
437250.11	4120476.86	1477.63	82	Top
437293.49	4120532.35	1478.13	83	Right
437292.06	4120524.76	1478.15	83	Base
437285.67	4120523.48	1477.98	83	Base
437279.84	4120524.86	1479.10	83	Left
437289.86	4120524.87	1479.52	83	Top
437334.17	4120611.20	1477.26	84	Right
437322.50	4120584.63	1476.66	84	Base
437313.82	4120573.22	1478.37	84	Base
437305.45	4120566.77	1479.09	84	Base
437291.84	4120548.65	1480.94	84	Base
437287.02	4120533.86	1482.20	84	Base
437273.94	4120534.64	1484.26	84	Left
437282.91	4120535.19	1484.47	84	Top
437289.51	4120549.94	1483.87	84	Top

Table A.1 continued

X	Y	MSL	SS Body	Side
437295.33	4120558.30	1483.59	84	Top
437311.18	4120575.78	1482.48	84	Top
437327.39	4120601.13	1479.00	84	Top
437280.63	4120531.21	1482.28	85	Right
437273.31	4120527.96	1481.22	85	Base
437266.68	4120527.23	1479.99	85	Base
437258.39	4120524.24	1480.84	85	Base
437250.27	4120519.91	1482.80	85	Base
437240.58	4120519.15	1486.62	85	Left
437252.43	4120526.54	1485.12	85	Top
437269.86	4120530.71	1483.46	85	Top
437223.70	4120497.02	1490.45	86	Right
437222.87	4120486.34	1487.77	86	Base
437209.22	4120479.42	1488.54	86	Base
437192.42	4120469.01	1488.26	86	Base
437181.51	4120459.79	1489.69	86	Base
437178.20	4120433.25	1490.17	86	Base
437120.14	4120416.85	1491.31	86	Base
437093.76	4120413.62	1496.73	86	Left
437114.75	4120419.89	1496.34	86	Top
437123.69	4120420.30	1495.95	86	Top
437166.34	4120433.23	1495.49	86	Top
437181.28	4120466.45	1493.24	86	Top
437217.44	4120486.83	1491.62	86	Top
437266.70	4120682.32	1501.68	87	Right
437263.67	4120643.17	1500.28	87	Base
437241.13	4120602.73	1500.37	87	Base
437215.16	4120568.04	1499.80	87	Base
437188.54	4120528.78	1500.98	87	Base
437158.20	4120506.62	1505.17	87	Base
437130.99	4120478.55	1506.45	87	Base
436986.86	4120495.53	1510.01	87	Base
436933.57	4120483.53	1517.27	87	Left
436972.76	4120495.64	1518.95	87	Top
437124.67	4120481.27	1515.29	87	Top
437166.23	4120523.01	1512.58	87	Top
437196.78	4120554.83	1510.20	87	Top
437224.25	4120593.63	1508.01	87	Top
437263.08	4120660.37	1503.75	87	Top
436900.77	4120377.00	1487.71	88	Right
436884.01	4120367.43	1487.32	88	Base
436847.39	4120358.70	1489.45	88	Base

Table A.1 continued

X	Y	MSL	SS Body	Side
436829.16	4120349.53	1490.17	88	Base
436817.31	4120342.32	1493.11	88	Left
436825.73	4120355.23	1493.23	88	Top
436878.18	4120369.37	1489.12	88	Top
436911.53	4120501.79	1531.71	89	Right
436900.46	4120490.56	1531.99	89	Base
436887.68	4120479.62	1531.40	89	Base
436859.09	4120460.46	1532.55	89	Base
436844.41	4120446.43	1531.00	89	Base
436795.52	4120424.07	1531.93	89	Base
436731.77	4120408.12	1544.57	89	Left
436790.55	4120430.93	1543.60	89	Top
436850.79	4120459.77	1538.23	89	Top
436897.42	4120490.75	1535.16	89	Top
436913.08	4120498.17	1529.63	90	Right
436903.82	4120491.47	1528.96	90	Base
436894.20	4120485.76	1531.28	90	Left
436904.49	4120495.43	1531.90	90	Top
436907.03	4120489.18	1525.85	91	Right
436899.83	4120484.66	1524.12	91	Base
436893.14	4120480.92	1526.31	91	Left
436897.82	4120487.59	1527.19	91	Top
437143.85	4120584.84	1538.89	92	Right
437134.85	4120577.71	1538.27	92	Base
437120.21	4120563.92	1539.10	92	Base
437096.54	4120551.78	1540.74	92	Base
437080.89	4120549.97	1540.25	92	Base
437057.28	4120541.69	1539.94	92	Base
437003.39	4120556.19	1544.45	92	Left
437042.29	4120549.32	1544.61	92	Top
437084.93	4120549.71	1543.71	92	Top
437111.71	4120559.98	1543.06	92	Top
437137.90	4120581.78	1540.51	92	Top
437133.83	4120576.70	1538.28	93	Right
437128.40	4120567.02	1537.27	93	Base
437120.16	4120558.18	1537.26	93	Base
437100.65	4120552.20	1539.64	93	Left
437111.08	4120556.67	1539.88	93	Top
437127.53	4120568.82	1538.78	93	Top
437207.38	4120662.09	1541.83	94	Right
437199.86	4120644.05	1537.82	94	Base
437186.02	4120626.49	1538.68	94	Base

Table A.1 continued

X	Y	MSL	SS Body	Side
437163.64	4120604.64	1539.04	94	Base
437151.72	4120593.21	1539.67	94	Base
437142.10	4120585.69	1541.21	94	Base
437128.94	4120575.51	1542.82	94	Base
437117.93	4120568.04	1545.29	94	Left
437129.02	4120579.50	1545.30	94	Top
437152.08	4120598.24	1544.40	94	Top
437168.28	4120611.51	1544.41	94	Top
437187.11	4120633.91	1543.65	94	Top
437202.72	4120658.04	1543.32	94	Top
437190.83	4120631.02	1538.06	95	Right
437180.58	4120621.64	1536.46	95	Base
437172.06	4120608.99	1536.77	95	Base
437163.72	4120603.39	1539.02	95	Left
437173.25	4120612.13	1539.10	95	Top
437183.61	4120623.56	1537.89	95	Top
437186.47	4120679.23	1548.24	96	Right
437184.81	4120652.25	1547.54	96	Base
437172.48	4120635.35	1547.56	96	Base
437159.39	4120620.42	1548.63	96	Base
437134.71	4120597.86	1550.77	96	Base
437107.86	4120575.28	1551.14	96	Base
437073.99	4120560.21	1552.19	96	Base
437039.35	4120554.25	1551.65	96	Base
436955.10	4120560.35	1553.86	96	Base
436905.39	4120545.12	1551.21	96	Base
436866.90	4120515.19	1557.35	96	Base
436819.47	4120476.39	1555.83	96	Base
436726.59	4120449.64	1565.42	96	Base
436751.85	4120458.57	1568.25	96	Left
436803.03	4120475.71	1571.98	96	Top
436861.06	4120519.94	1565.51	96	Top
436985.23	4120573.34	1559.37	96	Top
437089.46	4120568.38	1558.37	96	Top
437139.59	4120608.07	1556.57	96	Top
437178.80	4120646.21	1554.29	96	Top
437186.65	4120668.31	1552.05	96	Top
436880.88	4120501.72	1544.42	97	Right
436880.37	4120495.36	1542.28	97	Base
436871.36	4120491.15	1543.79	97	Base
436858.18	4120483.84	1545.56	97	Base
436846.96	4120478.79	1546.22	97	Base

Table A.1 continued

X	Y	MSL	SS Body	Side
436835.89	4120476.82	1548.01	97	Left
436856.94	4120488.71	1547.87	97	Top
436875.46	4120498.40	1546.82	97	Top
437092.25	4120057.28	1450.01	98	Right
437095.72	4120053.82	1449.12	98	Base
437097.25	4120050.28	1448.85	98	Base
437101.51	4120044.09	1448.36	98	Base
437105.52	4120038.13	1448.62	98	Base
437110.82	4120031.79	1449.14	98	Left
437104.55	4120037.41	1449.99	98	Top
437100.42	4120043.22	1450.74	98	Top
437098.13	4120047.87	1450.48	98	Top
437094.15	4120054.08	1450.37	98	Top
437077.95	4120069.68	1450.20	99	Right
437083.87	4120067.65	1449.30	99	Base
437085.35	4120063.74	1450.53	99	Left
437081.67	4120065.56	1451.02	99	Top
437115.41	4120020.81	1449.86	100	Right
437116.30	4120017.71	1449.53	100	Base
437113.23	4120015.41	1450.30	100	Left
437114.61	4120018.53	1450.41	100	Top
437105.00	4120002.55	1450.63	101	Right
437098.38	4120004.02	1452.38	101	Top
437094.71	4120007.19	1453.16	101	Top
437090.60	4120009.69	1454.16	101	Top
437072.92	4120000.56	1452.83	101	Top
437080.95	4119995.50	1452.82	101	Top
437083.93	4119993.22	1452.39	101	Left
437081.68	4119997.65	1451.59	101	Base
437075.97	4120001.23	1451.74	101	Base
437074.65	4120004.06	1451.90	101	Base
437096.79	4120000.26	1450.54	101	Base
437098.48	4119972.65	1451.79	102	Right
437099.71	4119970.28	1451.60	102	Base
437099.47	4119966.50	1452.23	102	Left
437098.37	4119969.63	1452.27	102	Top
437103.43	4119950.16	1452.66	103	Right
437104.54	4119948.53	1452.66	103	Base
437103.36	4119946.67	1453.35	103	Left
437102.91	4119948.47	1453.42	103	Top
437109.19	4119934.89	1451.71	104	Right
437116.03	4119934.01	1449.99	104	Base

Table A.1 continued

X	Y	MSL	SS Body	Side
437120.44	4119929.20	1450.35	104	Base
437118.49	4119924.09	1451.60	104	Base
437114.93	4119927.25	1452.97	104	Left
437113.67	4119928.52	1452.52	104	Top
437112.42	4119929.83	1452.28	104	Top
437022.47	4119922.64	1469.59	105	Right
437035.65	4119921.54	1467.65	105	Base
437035.38	4119916.13	1468.03	105	Base
437034.80	4119909.56	1467.73	105	Base
437030.61	4119910.68	1470.63	105	Top
437029.33	4119916.61	1470.58	105	Top
437046.29	4119865.21	1458.60	106	Right
437044.44	4119854.35	1458.36	106	Base
437039.54	4119831.65	1459.52	106	Base
437019.19	4119791.23	1461.61	106	Base
437024.00	4119776.12	1461.54	106	Base
437026.27	4119772.02	1463.13	106	Left
437020.08	4119775.33	1464.21	106	Top
437019.50	4119794.86	1464.29	106	Top
437035.60	4119833.83	1461.34	106	Top
437041.56	4119857.18	1460.08	106	Top
437129.44	4119933.00	1446.30	107	Right
437138.51	4119918.58	1443.79	107	Base
437119.29	4119896.33	1445.34	107	Base
437105.52	4119862.04	1445.16	107	Base
437108.15	4119854.26	1447.99	107	Base
437094.50	4119826.15	1448.70	107	Base
437090.94	4119800.61	1449.93	107	Base
437068.97	4119770.14	1453.58	107	Base
437066.86	4119757.57	1455.15	107	Left
437065.19	4119775.53	1456.15	107	Top
437053.29	4119781.56	1456.12	107	Top
437090.00	4119808.81	1453.29	107	Top
437087.64	4119827.53	1452.48	107	Top
437104.74	4119871.27	1452.32	107	Top
437117.51	4119900.47	1450.70	107	Top
437134.19	4119921.08	1447.75	107	Top
437116.07	4119854.21	1441.61	108	Right
437119.32	4119850.42	1440.35	108	Base
437116.70	4119838.15	1440.96	108	Base
437114.13	4119830.36	1441.83	108	Left
437117.96	4119843.95	1443.40	108	Top

Table A.1 continued

X	Y	MSL	SS Body	Side
437116.66	4119850.39	1442.28	108	Top
437100.59	4119802.98	1446.08	108	Right
437091.61	4119771.04	1441.99	108	Base
437094.17	4119761.20	1441.31	108	Base
437095.77	4119736.60	1443.13	108	Base
437092.61	4119734.40	1446.11	108	Left
437091.58	4119744.56	1445.66	108	Top
437089.56	4119761.76	1445.65	108	Top
437086.30	4119773.27	1444.83	108	Top
436998.23	4119848.44	1471.03	110	Right
437003.38	4119837.92	1469.68	110	Base
437007.29	4119826.41	1469.30	110	Base
437004.87	4119810.57	1470.00	110	Base
437003.45	4119796.89	1469.61	110	Base
436996.25	4119780.62	1471.47	110	Left
437000.99	4119801.94	1472.65	110	Top
437000.21	4119815.19	1472.93	110	Top
437002.09	4119833.42	1472.56	110	Top
436998.78	4119840.08	1472.49	110	Top
436996.35	4119810.57	1474.12	111	Right
436999.16	4119802.24	1473.19	111	Base
436990.60	4119772.35	1475.65	111	Left
436985.06	4119777.33	1476.81	111	Top
436994.40	4119804.15	1475.37	111	Top
436974.49	4119770.90	1480.18	112	Right
436981.73	4119768.34	1479.47	112	Base
436979.70	4119756.90	1481.11	112	Left
436976.46	4119765.09	1481.50	112	Top
436952.84	4119847.98	1484.06	113	Right
436956.87	4119845.61	1483.43	113	Base
436946.49	4119836.28	1485.90	113	Left
436951.79	4119845.97	1485.21	113	Top
436910.96	4119791.01	1493.97	114	Right
436917.71	4119785.60	1492.56	114	Base
436922.93	4119782.39	1491.79	114	Base
436921.31	4119776.76	1493.46	114	Left
436917.61	4119781.33	1494.78	114	Top
436911.98	4119785.19	1495.60	114	Top
436913.26	4119819.47	1500.00	115	Right
436901.56	4119801.10	1499.36	115	Base
436900.97	4119788.36	1498.72	115	Base
436899.76	4119777.13	1500.78	115	Left

Table A.1 continued

X	Y	MSL	SS Body	Side
436895.96	4119781.94	1500.79	115	Top
436895.23	4119794.87	1502.19	115	Top
436895.90	4119802.70	1503.02	116	Right
436895.23	4119794.87	1502.18	116	Base
436895.26	4119781.38	1501.59	116	Left
436895.29	4119791.59	1503.07	116	Top
436892.34	4119799.42	1504.88	116	Top
436866.96	4119852.06	1507.80	117	Right
436878.82	4119852.26	1504.03	117	Base
436889.52	4119842.84	1503.53	117	Base
436895.20	4119831.51	1504.89	117	Base
436887.50	4119823.75	1508.72	117	Left
436885.74	4119832.56	1509.01	117	Top
436879.27	4119845.94	1508.26	117	Top
436874.14	4119851.29	1507.87	117	Top
436862.53	4119852.11	1508.33	118	Base
436869.94	4119844.72	1510.64	118	Left
436861.07	4119851.41	1511.88	118	Top
436854.68	4119842.15	1513.78	119	Right
436868.99	4119840.46	1512.28	119	Base
436870.08	4119824.11	1512.44	119	Left
436864.76	4119840.44	1514.76	119	Top
436884.57	4119832.60	1509.74	120	Right
436882.02	4119821.11	1509.38	120	Base
436867.49	4119808.90	1512.22	120	Left
436882.66	4119822.27	1510.53	120	Top
436847.21	4119902.89	1498.38	121	Right
436863.14	4119904.80	1494.50	121	Base
436880.14	4119890.62	1494.84	121	Base
436880.22	4119868.41	1498.12	121	Left
436877.07	4119873.18	1499.45	121	Top
436876.29	4119890.42	1498.89	121	Top
436861.10	4119902.15	1497.32	121	Top
436859.51	4119898.25	1499.45	122	Right
436870.97	4119893.05	1498.63	122	Base
436871.58	4119881.12	1500.29	122	Left
436864.67	4119896.06	1500.37	122	Top
436916.69	4119935.14	1480.70	123	Right
436917.23	4119926.49	1479.79	123	Base
436909.14	4119916.37	1481.38	123	Left
436913.84	4119927.66	1482.04	123	Top
436972.36	4119974.86	1465.89	124	Right

Table A.1 continued

X	Y	MSL	SS Body	Side
436991.24	4119977.04	1465.44	124	Base
436997.40	4119972.23	1465.44	124	Left
436988.68	4119974.52	1466.62	124	Top
436961.75	4119999.71	1468.05	125	Right
436971.06	4119996.81	1467.14	125	Base
436970.12	4119987.97	1467.56	125	Left
436967.23	4119995.15	1467.99	125	Top
436989.04	4120087.29	1462.73	126	Right
436980.41	4120070.24	1460.66	126	Base
436970.32	4120066.08	1462.97	126	Base
436964.52	4120067.65	1465.46	126	Left
436972.30	4120070.75	1463.80	126	Top
436980.42	4120074.76	1463.06	126	Top
436985.45	4120082.13	1463.07	126	Top
437069.97	4120102.81	1448.87	127	Right
437073.42	4120092.45	1447.57	127	Base
437079.68	4120078.11	1447.78	127	Base
437065.50	4120078.54	1448.52	127	Base
437057.59	4120075.31	1449.76	127	Base
437051.19	4120075.57	1450.58	127	Left
437061.02	4120078.65	1449.96	127	Top
437075.62	4120084.11	1449.54	127	Top
437073.51	4120090.95	1449.26	127	Top
437070.40	4120099.74	1449.34	127	Top
437002.94	4120119.57	1462.31	128	Right
437002.57	4120114.12	1461.94	128	Base
436997.43	4120109.98	1462.28	128	Left
437000.00	4120115.73	1462.66	128	Top
436967.69	4120176.48	1461.48	129	Right
436976.69	4120158.89	1460.78	129	Base
437000.69	4120136.66	1462.57	129	Left
436971.92	4120164.59	1462.08	129	Top
436954.28	4120245.65	1461.88	130	Right
436948.90	4120233.32	1461.90	130	Base
436945.66	4120214.67	1461.44	130	Base
436938.89	4120203.54	1462.57	130	Left
436941.29	4120217.20	1464.81	130	Top
436947.33	4120234.57	1464.21	130	Top
437066.20	4120169.93	1459.34	131	Right
437047.32	4120176.61	1457.25	131	Base
437028.89	4120193.65	1460.23	131	Left
437047.21	4120182.27	1459.84	131	Top

Table A.1 continued

X	Y	MSL	SS Body	Side
437082.66	4120178.81	1464.01	132	Right
437068.50	4120177.55	1463.61	132	Base
437032.41	4120198.69	1463.24	132	Base
436952.89	4120271.88	1465.38	132	Left
437044.05	4120199.96	1465.38	132	Top
437076.26	4120180.12	1465.03	132	Top
437126.17	4120163.25	1463.69	133	Right
437117.66	4120164.09	1463.33	133	Base
437110.38	4120167.79	1463.84	133	Left
437120.16	4120165.60	1464.48	133	Top
437129.83	4120153.81	1461.61	134	Right
437121.01	4120157.45	1461.71	134	Base
437115.48	4120160.36	1462.18	134	Left
437123.71	4120158.38	1462.56	134	Top
437158.73	4120147.30	1460.39	135	Right
437153.23	4120144.06	1459.97	135	Base
437147.77	4120141.95	1460.17	135	Base
437139.34	4120148.67	1461.31	135	Left
437147.68	4120144.92	1461.27	135	Top
437153.26	4120145.17	1461.09	135	Top
437200.88	4120172.38	1458.94	136	Right
437191.98	4120156.69	1458.40	136	Base
437181.85	4120152.32	1458.77	136	Base
437170.85	4120152.06	1460.57	136	Left
437181.02	4120154.26	1460.32	136	Top
437195.43	4120162.05	1460.35	136	Top
437206.69	4120226.32	1458.51	137	Right
437201.55	4120193.33	1458.99	137	Base
437191.35	4120168.82	1461.43	137	Base
437183.10	4120167.90	1462.48	137	Base
437164.01	4120166.92	1463.20	137	Left
437176.93	4120169.91	1463.50	137	Top
437188.02	4120170.94	1463.24	137	Top
437199.40	4120195.34	1460.46	137	Top
437166.86	4120221.90	1467.16	138	Right
437162.32	4120215.87	1466.41	138	Base
437154.49	4120213.93	1467.83	138	Left
437160.29	4120218.40	1468.24	138	Top
437147.97	4120208.99	1467.80	139	Right
437137.70	4120192.78	1466.99	139	Base
437120.96	4120183.05	1466.67	139	Base
437098.48	4120186.21	1466.06	139	Base

Table A.1 continued

X	Y	MSL	SS Body	Side
437088.13	4120200.94	1468.01	139	Base
437092.26	4120203.52	1469.51	139	Left
437097.51	4120202.02	1469.42	139	Top
437117.89	4120190.40	1469.69	139	Top
437128.63	4120193.32	1469.67	139	Top
437141.73	4120207.01	1468.46	139	Top
437134.13	4120210.69	1470.77	140	Right
437128.30	4120200.87	1470.24	140	Base
437120.46	4120200.64	1471.02	140	Left
437127.86	4120208.21	1471.13	140	Top
437148.58	4120249.51	1472.88	141	Right
437140.65	4120231.80	1473.22	141	Base
437124.30	4120223.94	1474.32	141	Base
437115.66	4120224.64	1474.87	141	Left
437123.21	4120229.89	1475.74	141	Top
437143.80	4120242.05	1473.95	141	Top
437141.39	4120264.09	1476.10	142	Right
437137.57	4120243.29	1475.72	142	Base
437126.28	4120236.32	1477.19	142	Left
437137.39	4120258.85	1476.82	142	Top
437124.71	4120565.09	1566.68	144	Right
437108.46	4120566.38	1565.45	144	Base
437098.36	4120571.60	1567.14	144	Left
437110.30	4120570.43	1568.74	144	Top
437121.21	4120566.68	1567.43	144	Top
437077.40	4120586.84	1579.08	147	Right
437062.51	4120580.90	1571.10	147	Base
437042.73	4120582.49	1571.70	147	Base
437018.16	4120588.24	1573.18	147	Left
437035.86	4120588.53	1576.57	147	Top
437066.77	4120584.23	1578.48	147	Top
437080.87	4120589.58	1584.89	148	Right
437064.38	4120584.06	1577.53	148	Base
437040.73	4120586.39	1579.62	148	Base
437018.66	4120593.95	1579.33	148	Left
437041.28	4120585.48	1582.61	148	Top
437069.79	4120585.80	1584.79	148	Top
437042.36	4120583.92	1579.15	149	Right
437016.03	4120592.41	1574.90	149	Base
436982.71	4120580.34	1575.38	149	Base
436967.42	4120578.37	1578.26	149	Left
436987.62	4120584.10	1578.72	149	Top

Table A.1 continued

X	Y	MSL	SS Body	Side
437014.93	4120594.69	1580.06	149	Top
437029.60	4120591.39	1580.03	149	Top
437059.03	4120558.64	1554.41	150	Right
437005.84	4120563.74	1552.70	150	Base
436970.69	4120543.94	1555.35	150	Base
436914.21	4120526.02	1558.20	150	Base
436866.67	4120502.66	1555.88	150	Base
436807.27	4120495.05	1562.37	150	Base
436753.20	4120486.30	1564.77	150	Base
436691.57	4120471.68	1566.73	150	Base
436638.46	4120455.84	1570.16	150	Base
436570.03	4120431.39	1575.47	150	Base
436543.48	4120380.20	1573.61	150	Base
436516.37	4120306.83	1577.48	150	Base
436502.42	4120246.59	1577.24	150	Base
436497.51	4120227.45	1581.72	150	Left
436505.50	4120285.52	1584.97	150	Top
436540.57	4120387.06	1583.86	150	Top
436645.28	4120463.03	1577.67	150	Top
436777.75	4120492.98	1573.30	150	Top
436851.64	4120505.18	1570.45	150	Top
436926.49	4120533.55	1566.46	150	Top
437038.46	4120564.44	1562.33	150	Top
436735.85	4120476.38	1564.13	151	Right
436710.59	4120465.19	1560.01	151	Base
436685.27	4120462.75	1562.49	151	Base
436671.62	4120463.26	1566.76	151	Left
436693.26	4120472.86	1568.05	151	Top
436721.07	4120474.65	1566.43	151	Top
436996.16	4120518.88	1531.78	152	Right
436983.55	4120506.77	1525.29	152	Base
436968.50	4120500.54	1527.02	152	Base
436955.61	4120498.45	1529.41	152	Base
436931.05	4120490.46	1529.60	152	Base
436905.79	4120479.35	1530.61	152	Base
436892.89	4120474.26	1534.87	152	Left
436909.47	4120489.61	1536.97	152	Top
436949.35	4120499.02	1534.67	152	Top
436971.41	4120505.07	1534.32	152	Top
436987.30	4120518.24	1533.23	152	Top
436982.44	4120531.04	1541.02	153	Right
436947.52	4120516.99	1542.82	153	Base

Table A.1 continued

X	Y	MSL	SS Body	Side
436902.26	4120503.72	1545.75	153	Base
436892.73	4120500.38	1547.63	153	Left
436915.30	4120511.22	1547.80	153	Top
436945.12	4120517.39	1546.66	153	Top
436970.34	4120530.99	1544.64	153	Top
436600.92	4120356.08	1536.67	154	Right
436584.96	4120300.12	1535.87	154	Base
436586.77	4120240.13	1534.80	154	Base
436592.49	4120163.14	1540.03	154	Base
436618.94	4120109.62	1539.04	154	Base
436645.25	4120055.31	1539.45	154	Base
436684.29	4120012.88	1541.19	154	Base
436707.48	4119972.96	1541.46	154	Base
436736.07	4119918.20	1542.63	154	Left
436696.11	4119983.17	1546.27	154	Top
436679.04	4120013.76	1546.36	154	Top
436628.81	4120065.90	1547.58	154	Top
436608.16	4120125.27	1545.27	154	Top
436563.14	4120225.74	1542.94	154	Top
436576.49	4120169.50	1547.40	155	Right
436596.83	4120147.06	1547.11	155	Base
436624.67	4120080.32	1545.66	155	Base
436664.91	4120031.37	1545.48	155	Base
436688.09	4119995.50	1547.05	155	Base
436706.21	4119954.31	1548.43	155	Base
436732.75	4119914.85	1548.90	155	Left
436719.17	4119917.86	1553.91	155	Top
436692.23	4119975.19	1551.01	155	Top
436655.77	4120029.50	1551.02	155	Top
436623.41	4120065.19	1551.19	155	Top
436603.95	4120107.74	1549.93	155	Top
436583.08	4120158.04	1548.17	155	Top
436554.05	4120126.55	1567.09	156	Right
436565.34	4120115.06	1564.06	156	Base
436565.60	4120097.44	1568.89	156	Left
436558.19	4120114.60	1568.53	156	Top
436596.68	4120091.15	1556.56	157	Right
436611.42	4120065.99	1556.08	157	Base
436620.69	4120042.03	1556.65	157	Base
436635.09	4120027.68	1556.14	157	Base
436642.20	4120018.53	1560.45	157	Left
436621.50	4120028.83	1562.77	157	Top

Table A.1 continued

X	Y	MSL	SS Body	Side
436612.66	4120052.05	1562.51	157	Top
436595.92	4120078.53	1561.23	157	Top
436647.32	4120020.67	1557.83	158	Right
436665.63	4120004.61	1555.30	158	Base
436679.88	4119980.59	1554.68	158	Base
436707.40	4119914.77	1559.26	158	Left
436692.94	4119941.31	1564.24	158	Top
436677.91	4119973.49	1563.36	158	Top
436654.75	4120007.05	1560.31	158	Top
436573.93	4120061.58	1576.66	159	Right
436584.19	4120052.13	1574.82	159	Base
436584.58	4120044.10	1577.54	159	Left
436577.92	4120054.70	1578.98	159	Top
436510.80	4120127.94	1581.23	160	Right
436543.22	4120114.35	1575.03	160	Base
436549.33	4120091.36	1578.17	160	Base
436561.86	4120071.70	1579.03	160	Base
436585.66	4120029.32	1580.20	160	Base
436585.09	4120016.25	1581.83	160	Left
436575.04	4120044.80	1583.52	160	Top
436552.09	4120076.06	1582.76	160	Top
436535.09	4120120.18	1579.09	160	Top
436617.31	4119997.53	1576.27	161	Right
436644.31	4119974.65	1577.20	161	Base
436650.66	4119955.06	1583.15	161	Left
436639.99	4119969.37	1583.15	161	Top
436615.42	4119991.35	1581.70	161	Top
436647.43	4119956.39	1584.34	162	Right
436660.30	4119942.17	1580.68	162	Base
436665.60	4119926.84	1580.48	162	Base
436662.27	4119916.64	1583.94	162	Left
436657.85	4119936.75	1587.09	162	Top
436649.80	4119951.16	1586.83	162	Top
436682.76	4119951.66	1566.98	163	Right
436683.24	4119946.59	1567.18	163	Base
436681.38	4119937.57	1569.88	163	Left
436679.27	4119944.49	1570.28	163	Top
436687.94	4119870.37	1582.39	164	Right
436693.44	4119856.26	1580.12	164	Base
436693.29	4119842.96	1582.20	164	Base
436691.71	4119835.79	1583.96	164	Left
436687.33	4119843.22	1585.35	164	Top

Table A.1 continued

X	Y	MSL	SS Body	Side
436687.48	4119857.54	1585.95	164	Top
436494.77	4120127.79	1587.83	165	Right
436535.78	4120104.85	1584.90	165	Base
436558.45	4120060.29	1586.04	165	Base
436588.59	4119999.55	1585.99	165	Left
436567.82	4120032.87	1592.63	165	Top
436531.35	4120096.93	1590.23	165	Top
436494.85	4120240.45	1585.28	166	Right
436490.17	4120208.61	1581.44	166	Base
436482.03	4120164.04	1583.09	166	Base
436483.59	4120130.58	1589.81	166	Left
436481.04	4120153.11	1590.02	166	Top
436475.66	4120183.68	1590.46	166	Top
436488.10	4120223.53	1588.02	166	Top
436500.76	4120077.05	1605.71	167	Right
436535.05	4120047.15	1602.91	167	Base
436552.42	4120014.65	1602.14	167	Base
436552.74	4119993.51	1605.53	167	Left
436544.00	4120020.47	1611.00	167	Top
436530.43	4120045.66	1610.78	167	Top
436504.54	4120070.11	1609.18	167	Top
436602.34	4119957.76	1603.52	168	Right
436632.04	4119947.83	1598.91	168	Base
436618.74	4119922.86	1609.79	168	Left
436619.85	4119940.22	1609.66	168	Top
436628.56	4119845.32	1613.36	169	Right
436644.57	4119848.31	1607.71	169	Base
436643.26	4119837.44	1612.17	169	Left
436640.43	4119845.88	1613.26	169	Top
436748.11	4119923.65	1533.58	170	Right
436752.88	4119921.09	1531.79	170	Base
436752.77	4119914.28	1533.95	170	Left
436750.04	4119919.87	1533.93	170	Top
436753.99	4119931.82	1527.35	171	Right
436763.11	4119920.14	1524.88	171	Base
436764.40	4119910.26	1527.76	171	Left
436757.84	4119920.79	1529.07	171	Top
436757.76	4119947.96	1521.68	172	Right
436763.03	4119948.50	1518.61	172	Base
436763.95	4119929.88	1521.89	172	Left
436759.61	4119942.99	1522.65	172	Top
436732.94	4119997.40	1524.15	173	Right

Table A.1 continued

X	Y	MSL	SS Body	Side
436739.43	4119985.79	1522.86	173	Base
436740.29	4119967.52	1526.10	173	Left
436739.89	4119980.33	1525.46	173	Top
436715.99	4120002.03	1530.48	174	Right
436725.74	4119991.66	1528.86	174	Base
436726.20	4119975.53	1531.46	174	Left
436718.87	4119992.65	1531.74	174	Top
436706.30	4120050.26	1523.03	175	Right
436716.83	4120032.33	1521.25	175	Base
436724.36	4120009.45	1524.96	175	Left
436710.39	4120030.79	1526.15	175	Top
436719.13	4120044.69	1517.98	176	Right
436739.46	4120023.74	1515.48	176	Base
436735.45	4120012.21	1519.90	176	Left
436725.77	4120031.62	1520.08	176	Top
436767.88	4120021.74	1508.58	177	Right
436766.31	4120013.16	1508.41	177	Base
436768.34	4120003.14	1510.47	177	Left
436764.98	4120010.72	1510.82	177	Top
436779.07	4120036.74	1502.60	178	Right
436782.17	4120028.88	1501.55	178	Base
436788.11	4120016.17	1500.68	178	Base
436804.68	4119997.67	1499.27	178	Base
436802.38	4119974.42	1503.60	178	Left
436801.20	4119993.40	1503.79	178	Top
436774.51	4120015.90	1505.30	178	Top
436854.42	4120100.51	1477.96	179	Right
436856.24	4120094.18	1478.01	179	Base
436856.29	4120088.16	1478.69	179	Left
436854.19	4120094.73	1478.80	179	Top
436831.63	4120139.28	1486.71	180	Right
436845.59	4120136.34	1485.11	180	Base
436844.60	4120129.02	1486.35	180	Left
436836.96	4120136.59	1486.94	180	Top
436834.73	4120181.12	1481.26	181	Right
436835.01	4120175.54	1480.94	181	Base
436827.15	4120167.23	1482.62	181	Left
436833.88	4120178.34	1482.03	181	Top
436608.76	4120156.56	1532.86	182	Right
436618.36	4120144.00	1530.19	182	Base
436633.69	4120116.05	1530.39	182	Base
436634.14	4120110.79	1532.68	182	Left

Table A.1 continued

X	Y	MSL	SS Body	Side
436615.62	4120133.25	1536.56	182	Top
436623.36	4120347.90	1525.85	183	Right
436617.57	4120328.19	1519.69	183	Base
436602.42	4120276.64	1522.04	183	Base
436596.55	4120231.16	1522.49	183	Base
436606.85	4120175.52	1530.15	183	Base
436616.06	4120132.18	1538.14	183	Left
436599.40	4120162.36	1538.55	183	Top
436576.96	4120217.65	1534.40	183	Top
436597.76	4120250.79	1530.77	183	Top
436618.65	4120344.91	1528.07	183	Top
436589.09	4120255.29	1534.73	184	Right
436588.37	4120243.61	1533.80	184	Base
436582.33	4120237.33	1535.87	184	Left
436587.26	4120246.32	1536.00	184	Top
436595.77	4120335.40	1536.35	185	Right
436588.39	4120311.92	1535.22	185	Base
436579.10	4120279.98	1534.89	185	Base
436576.77	4120265.45	1539.16	185	Left
436579.74	4120304.25	1540.08	185	Top
436611.52	4120395.06	1544.70	186	Right
436597.19	4120377.74	1542.33	186	Base
436587.28	4120345.50	1542.47	186	Base
436571.41	4120320.34	1548.72	186	Left
436584.65	4120355.96	1547.92	186	Top
436598.38	4120385.87	1546.42	186	Top
436621.07	4120407.30	1547.38	187	Right
436599.91	4120384.88	1545.37	187	Base
436585.09	4120374.60	1550.24	187	Left
436596.65	4120391.11	1550.74	187	Top
436567.60	4120296.73	1547.10	188	Right
436568.88	4120283.11	1543.37	188	Base
436555.61	4120255.87	1549.97	188	Left
436554.62	4120280.40	1550.64	188	Top
436580.23	4120361.44	1551.26	189	Right
436568.54	4120325.22	1551.69	189	Base
436554.06	4120274.24	1551.11	189	Base
436542.77	4120213.79	1551.11	189	Base
436524.02	4120181.05	1559.45	189	Left
436530.70	4120208.79	1559.83	189	Top
436546.12	4120283.60	1556.63	189	Top
436564.10	4120333.88	1555.25	189	Top

Table A.1 continued

X	Y	MSL	SS Body	Side
436541.15	4120310.36	1563.10	190	Right
436542.57	4120300.84	1559.94	190	Base
436531.44	4120292.32	1565.38	190	Left
436532.85	4120303.26	1565.80	190	Top
436522.36	4120308.29	1573.76	191	Right
436516.19	4120271.42	1569.71	191	Base
436504.53	4120248.74	1575.96	191	Left
436509.33	4120274.61	1577.66	191	Top
436555.34	4120472.05	1600.25	192	Right
436539.25	4120415.40	1588.29	192	Base
436508.90	4120346.11	1590.53	192	Base
436495.31	4120286.86	1589.82	192	Base
436468.25	4120229.78	1596.47	192	Base
436451.55	4120190.79	1600.01	192	Left
436480.69	4120270.88	1601.08	192	Top
436500.66	4120339.13	1606.40	192	Top
436523.74	4120415.39	1601.18	192	Top
436945.12	4120398.01	1487.60	193	Right
436933.24	4120395.68	1485.49	193	Base
436912.49	4120392.15	1486.52	193	Base
436864.88	4120389.55	1488.77	193	Base
436833.86	4120374.45	1492.09	193	Left
436854.12	4120386.98	1492.37	193	Top
436898.37	4120393.58	1490.13	193	Top
436934.31	4120406.39	1491.69	194	Right
436912.87	4120397.93	1491.91	194	Base
436899.73	4120401.59	1493.46	194	Left
436915.00	4120401.89	1494.17	194	Top
436835.34	4120374.05	1492.30	195	Right
436800.23	4120363.53	1491.71	195	Base
436738.66	4120353.00	1494.41	195	Base
436727.11	4120340.10	1493.52	195	Base
436687.64	4120331.80	1497.35	195	Left
436740.28	4120355.90	1496.80	195	Top
436815.81	4120371.75	1494.10	195	Top
436810.35	4120376.39	1497.16	196	Right
436775.72	4120376.22	1498.00	196	Base
436742.52	4120363.44	1499.52	196	Base
436730.19	4120359.10	1502.42	196	Left
436768.20	4120375.05	1501.96	196	Top
436945.52	4120440.09	1502.49	197	Right
436928.69	4120427.67	1501.66	197	Base

Table A.1 continued

X	Y	MSL	SS Body	Side
436900.67	4120426.96	1504.00	197	Base
436892.83	4120431.64	1507.84	197	Left
436928.25	4120439.10	1507.52	197	Top
436990.85	4120431.71	1496.21	198	Right
436977.48	4120428.52	1495.30	198	Base
436961.71	4120433.82	1498.74	198	Left
436875.26	4120477.12	1538.57	199	Right
436840.00	4120463.87	1531.54	199	Base
436795.17	4120451.07	1535.68	199	Base
436755.67	4120443.15	1540.42	199	Base
436702.93	4120439.01	1547.96	199	Left
436746.29	4120451.40	1546.45	199	Top
436785.00	4120455.71	1543.12	199	Top
436844.20	4120472.47	1541.91	199	Top
436797.41	4120450.13	1534.22	200	Right
436775.29	4120444.81	1532.45	200	Base
436734.55	4120432.23	1535.16	200	Base
436698.77	4120431.78	1541.14	200	Base
436656.36	4120417.28	1544.87	200	Base
436628.52	4120408.35	1548.49	200	Left
436687.45	4120429.78	1546.13	200	Top
436774.74	4120448.06	1537.58	200	Top
436717.80	4120431.35	1538.14	201	Right
436698.08	4120430.73	1537.37	201	Base
436650.71	4120406.18	1539.11	201	Base
436629.08	4120394.67	1540.81	201	Left
436661.89	4120414.80	1543.13	201	Top
436696.88	4120430.24	1540.59	201	Top
436910.12	4120303.80	1474.73	202	Right
436892.43	4120291.75	1473.73	202	Base
436849.15	4120306.36	1475.65	202	Base
436802.13	4120313.72	1481.52	202	Left
436837.48	4120310.79	1480.52	202	Top
436895.76	4120294.27	1477.89	202	Top
436973.51	4120292.91	1469.85	203	Right
436956.54	4120311.02	1469.49	203	Base
436937.39	4120307.58	1469.31	203	Base
436920.46	4120283.75	1470.64	203	Left
436934.62	4120308.80	1470.87	203	Top
436942.46	4120318.28	1471.82	203	Top
436969.50	4120299.38	1471.03	203	Top
437000.36	4120594.47	1579.35	204	Right

Table A.1 continued

X	Y	MSL	SS Body	Side
436941.88	4120561.66	1573.59	204	Base
436884.52	4120534.98	1575.62	204	Base
436790.80	4120503.53	1577.18	204	Base
436726.28	4120483.08	1578.52	204	Base
436636.89	4120476.05	1587.74	204	Left
436688.73	4120487.69	1591.53	204	Top
436770.26	4120504.56	1588.12	204	Top
436857.79	4120532.62	1590.69	204	Top
436931.02	4120557.29	1583.15	204	Top
436932.60	4120577.27	1593.30	205	Right
436865.63	4120536.23	1590.60	205	Base
436814.64	4120509.10	1591.11	205	Base
436746.63	4120499.72	1597.28	205	Left
436784.68	4120502.08	1597.36	205	Top
436830.95	4120515.12	1603.92	205	Top
436877.19	4120541.96	1601.23	205	Top
436638.89	4119074.30	1453.02	206	Left
436649.93	4119059.58	1450.98	206	Base
436664.80	4119039.60	1451.95	206	Top
436647.06	4119045.89	1452.92	206	Top
436687.38	4119035.22	1450.04	206	Base
436701.05	4119039.78	1448.24	206	Base
436705.26	4119029.04	1450.12	206	Top
436688.19	4119023.17	1451.97	206	Top
436734.47	4119182.46	1450.15	206	Base
436692.15	4119132.84	1449.12	206	Base
436680.40	4119134.78	1453.40	206	Top
436691.48	4119140.62	1450.89	206	Top
436827.40	4119303.66	1443.08	206	Right
436830.34	4119289.69	1441.73	206	Base
436825.72	4119281.28	1443.36	206	Top
436827.81	4119290.80	1444.74	206	Top
436779.68	4119223.63	1446.51	206	Top
436759.47	4119195.84	1444.15	206	Base
436759.66	4119185.81	1445.38	206	Base
436755.20	4119191.53	1445.42	206	Top
436826.61	4119242.63	1440.44	206	Base
436686.82	4119213.53	1457.74	213	Right
436695.49	4119202.41	1455.39	213	Base
436650.20	4119156.71	1456.97	213	Left
436644.34	4119170.33	1457.85	213	Top
436704.76	4119226.22	1452.49	214	Right

Table A.1 continued

X	Y	MSL	SS Body	Side
436712.13	4119212.03	1451.70	214	Base
436708.09	4119202.77	1453.13	214	Left
436706.32	4119216.03	1453.19	214	Top
436742.19	4119301.02	1446.44	215	Right
436741.23	4119285.64	1446.18	215	Base
436752.59	4119262.48	1448.62	215	Base
436746.28	4119238.18	1450.20	215	Left
436743.42	4119254.67	1450.32	215	Top
436733.24	4119284.98	1449.18	215	Top
436768.65	4119247.48	1446.11	217	Right
436777.10	4119238.00	1445.47	217	Base
436768.82	4119227.72	1447.04	217	Left
436765.61	4119237.19	1447.78	217	Top
436746.09	4119395.17	1444.56	224	Right
436736.10	4119377.35	1443.96	224	Base
436756.63	4119357.77	1444.45	224	Base
436759.10	4119336.20	1446.43	224	Left
436727.25	4119360.47	1447.60	224	Top
436736.96	4119387.21	1446.97	224	Top
436850.82	4119407.81	1442.91	225	Right
436864.43	4119397.02	1441.02	225	Base
436868.20	4119375.15	1443.73	225	Left
436858.61	4119396.61	1444.57	225	Top
436884.66	4119436.77	1439.33	226	Right
436877.57	4119423.01	1439.40	226	Base
436873.94	4119426.37	1442.65	226	Left
436875.95	4119430.64	1442.30	226	Top
436779.31	4119537.71	1450.55	227	Right
436817.03	4119514.54	1449.15	227	Base
436806.23	4119472.47	1450.52	227	Base
436731.39	4119410.66	1453.26	227	Base
436681.14	4119367.45	1457.86	227	Base
436641.39	4119303.78	1461.80	227	Base
436615.09	4119289.33	1467.06	227	Left
436669.23	4119372.21	1462.66	227	Top
436797.51	4119473.33	1454.17	227	Top
436808.54	4119511.89	1452.20	227	Top
436937.06	4119485.26	1440.73	228	Right
436936.00	4119479.39	1440.36	228	Base
436927.20	4119474.89	1441.49	228	Left
436932.64	4119482.56	1442.06	228	Top
436825.90	4119525.15	1446.72	229	Right

Table A.1 continued

X	Y	MSL	SS Body	Side
436874.39	4119512.06	1447.26	229	Base
436819.58	4119499.14	1446.98	229	Left
436830.74	4119518.07	1447.40	229	Top
436851.99	4119561.27	1446.35	230	Right
436835.19	4119542.67	1445.45	230	Base
436835.30	4119547.01	1447.67	230	Left
436842.46	4119553.83	1447.50	230	Top
436849.12	4119600.84	1450.83	231	Right
436836.84	4119572.88	1450.10	231	Base
436793.87	4119565.24	1450.27	231	Base
436758.59	4119569.52	1454.58	231	Left
436788.31	4119580.07	1453.86	231	Top
436832.60	4119590.43	1452.66	231	Top
436872.26	4119761.51	1485.17	232	Right
436869.27	4119746.50	1484.78	232	Base
436855.30	4119737.59	1487.08	232	Left
436865.11	4119750.73	1486.99	232	Top
436844.03	4119727.83	1484.23	233	Right
436834.80	4119724.16	1482.26	233	Base
436825.88	4119724.03	1484.43	233	Left
436836.63	4119730.63	1485.96	233	Top
436801.93	4119720.48	1483.82	233	Base
436741.07	4119767.59	1492.04	233	Left
436804.73	4119724.39	1486.87	233	Top
436819.59	4119724.95	1485.43	234	Right
436892.88	4119720.98	1475.34	235	Right
436882.21	4119708.95	1474.11	235	Base
436861.23	4119703.88	1476.16	235	Base
436851.89	4119710.22	1478.43	235	Left
436866.50	4119709.31	1478.21	235	Top
436888.96	4119720.72	1476.92	235	Top
436819.03	4119669.16	1464.25	236	Right
436810.62	4119666.69	1463.87	236	Base
436787.29	4119680.58	1466.19	236	Left
436808.66	4119672.22	1466.08	236	Top
436846.99	4119657.48	1458.52	237	Right
436833.83	4119646.16	1458.09	237	Base
436815.58	4119648.41	1459.13	237	Base
436778.40	4119666.72	1461.10	237	Left
436814.03	4119651.34	1460.63	237	Top
436829.10	4119649.81	1459.99	237	Top
436853.43	4119618.74	1452.65	238	Right

Table A.1 continued

X	Y	MSL	SS Body	Side
436843.40	4119616.07	1453.79	238	Base
436830.41	4119620.32	1454.94	238	Left
436841.62	4119620.26	1454.63	238	Top
436964.83	4119704.02	1455.16	239	Right
436940.31	4119672.01	1453.44	239	Base
436900.48	4119635.27	1453.18	239	Base
436884.47	4119625.59	1455.71	239	Left
436895.47	4119642.71	1456.44	239	Top
436944.73	4119690.33	1457.17	239	Top
436918.00	4119608.84	1448.76	240	Right
436913.73	4119604.36	1448.46	240	Base
436910.33	4119606.63	1449.21	240	Left
436914.16	4119608.23	1449.28	240	Top
437016.66	4119647.28	1443.46	241	Right
436987.63	4119618.34	1440.48	241	Base
436958.27	4119602.09	1439.95	241	Base
436943.95	4119566.81	1438.82	241	Base
436941.92	4119521.52	1442.95	241	Left
436937.35	4119540.23	1444.21	241	Top
436958.37	4119585.83	1443.84	241	Top
436984.21	4119621.62	1445.34	241	Top
437034.45	4119643.91	1439.69	242	Right
437020.02	4119632.13	1438.12	242	Base
437008.22	4119629.71	1439.99	242	Left
437018.81	4119636.07	1440.06	242	Top
436969.05	4119781.57	1464.59	243	Right
436964.71	4119773.20	1462.85	243	Base
436943.61	4119765.42	1464.37	243	Base
436922.12	4119766.49	1467.27	243	Left
436951.28	4119772.20	1466.03	243	Top
436963.14	4119776.84	1465.54	243	Top
437050.63	4119785.06	1454.41	246	Right
437039.70	4119780.02	1452.42	246	Base
437010.49	4119768.26	1454.56	246	Left
437031.20	4119773.81	1454.51	246	Top
437050.13	4119786.26	1455.45	246	Top
436426.27	4119673.22	1612.77	248	Right
436420.49	4119646.76	1611.15	248	Base
436411.00	4119608.48	1612.51	248	Left
436422.33	4119661.50	1615.21	248	Top

Table A.2

Sandstone Body GPS Points in Rock House Cove

X	Y	MSL	SS Body	Side
418726.1	4116703	1480.775	1	Left
418975.8	4117030	1497.983	1	Top
419127.1	4117000	1492.305	1	Base
419050.7	4117132	1500.252	1	Top
419105.4	4117108	1489.08	1	Base
419186.7	4117221	1497.805	1	Right
419116.9	4117290	1508.653	2	Right
419104.5	4117214	1506.344	2	Base
419074.6	4117236	1510.698	2	Top
418945.3	4117029	1505.498	2	Base
418930.6	4117028	1514.161	2	Top
418526.6	4116806	1513.467	2	Left
418945.9	4117163	1520.002	3	Left
418964.6	4117181	1520.729	3	Right
418949.1	4117174	1521.609	3	Top
418956.5	4117170	1517.733	3	Base
418725	4116875	1526.177	4	Left
419032.2	4117365	1525.82	4	Right
418905.9	4117193	1529.51	4	Top
418933.8	4117180	1524.916	4	Base
418780.3	4116946	1533.089	4	Top
418801.2	4116950	1521.334	4	Base
418843.7	4116957	1502.349	5	Left
418924.5	4117014	1500.394	5	Right
418840	4116969	1505.984	5	Top
418861	4116971	1500.368	5	Base
419012.2	4117366	1537.406	6	Right
418963.6	4117281	1536.6	6	Left
418999.6	4117331	1538.31	6	Top
419004.1	4117330	1535.522	6	Base
418944.5	4117267	1540.308	7	Left
418991.8	4117325	1540.297	7	Right
418949	4117275	1542.267	7	Top
418950.9	4117273	1540.359	7	Base
418937.2	4117318	1559.14	8	Left
418982.7	4117391	1558.842	8	Right
418949.6	4117346	1560.08	8	Top
418951.9	4117346	1559.006	8	Base
418972.6	4117397	1565.445	9	Left

Table A.2 continued

X	Y	MSL	SS Body	Side
418988.2	4117415	1565.432	9	Right
418981.2	4117408	1567.693	9	Top
418983.4	4117407	1564.329	9	Base
418882.1	4117213	1542.356	10	Left
418919.4	4117218	1542.662	10	Right
418899.7	4117214	1544.025	10	Top
418906.6	4117214	1541.187	10	Base
418913.8	4117223	1546.332	11	Left
418916.8	4117232	1546.272	11	Right
418914.2	4117224	1548.423	11	Top
418915.2	4117223	1545.401	11	Base
418867.8	4117221	1549.12	12	Left
418907.6	4117236	1551.133	12	Right
418889.7	4117224	1550.85	12	Top
418891.5	4117223	1549.875	12	Base
418870.8	4117227	1553.63	13	Right
418801	4117091	1555.486	13	Left
418799.5	4117128	1556.371	13	Top
418806.8	4117130	1550.857	13	Base
418873.2	4117235	1560.111	14	Left
418915.5	4117288	1560.226	14	Right
418887.5	4117242	1562.44	14	Top
418891.5	4117241	1558.191	14	Base
418819.2	4117162	1550.836	15	Left
418815.1	4117193	1549.236	15	Right
418816	4117180	1550.54	15	Top
418820.2	4117180	1548.397	15	Base
418816.1	4117076	1541.786	16	Left
418832.1	4117150	1540.35	16	Right
418818.8	4117131	1544.498	16	Top
418821.4	4117135	1541.224	16	Base
418807.5	4117116	1547.64	17	Left
418820.8	4117152	1547.684	17	Right
418816.6	4117134	1548.85	17	Top
418819.1	4117138	1545.563	17	Base
418805.7	4117166	1561.915	18	Right
418783	4117097	1561.907	18	Left
418783.6	4117118	1561.841	18	Top
418787.5	4117120	1559.581	18	Base
418779.3	4117107	1565.317	19	Right
418748.9	4117057	1564.026	19	Left

Table A.2 continued

X	Y	MSL	SS Body	Side
418755.6	4117079	1565.228	19	Top
418759.1	4117081	1561.714	19	Base
418752.3	4116995	1538.293	20	Left
418764.5	4117005	1537.656	20	Right
418755	4117002	1538.351	20	Top
418758.3	4117005	1539.679	20	Base
418746.6	4117000	1542.691	21	Left
418752.3	4117007	1545.21	21	Right
418747.8	4117002	1543.894	21	Top
418752	4117003	1541.793	21	Base
418766.4	4117022	1546.855	22	Right
418702	4116889	1549.852	22	Left
418719.3	4116903	1550.455	22	Top
418990	4116914	1555.832	22	Base
418741.9	4117023	1560.461	23	Right
418722.7	4116998	1556.545	23	Left
418718.9	4117001	1560.145	23	Top
418730.1	4117010	1560.325	23	Base
418717.5	4117006	1562.543	24	Right
418715.8	4116990	1562.519	24	Left
418713.6	4116998	1563.767	24	Top
418716	4117001	1562.576	24	Base
418738.3	4117026	1567.576	25	Right
418702.8	4116964	1567.513	25	Left
418708.2	4116983	1568.741	25	Top
418708.5	4116987	1565.029	25	Base
418681.4	4116972	1581.579	26	Left
418687	4116981	1580.224	26	Right
418681.8	4116978	1584.122	26	Top
418686.9	4116978	1581.479	26	Base
418748.4	4116918	1541.904	27	Left
418756.7	4116941	1539.898	27	Right
418749.2	4116926	1545.436	27	Top
418756.5	4116929	1538.756	27	Base
418975.5	4117409	1570.972	28	Right
418761.1	4117220	1576.014	28	Left
418866.7	4117256	1579.979	28	Top
418872.1	4117251	1575.429	28	Base
418968	4117410	1579.05	29	Right
418802.2	4117238	1581.812	29	Left
418840.4	4117246	1585.942	29	Top

Table A.2 continued

X	Y	MSL	SS Body	Side
418844.9	4117246	1580.088	29	Base
418746.6	4117173	1589.662	30	Left
418959.9	4117417	1589.727	30	Right
418764.4	4117241	1589.957	30	Top
418762.7	4117237	1586.168	30	Base
418775.3	4117246	1594.798	31	Left
418827.3	4117263	1595.892	31	Right
418811.3	4117257	1598.715	31	Top
418815.3	4117256	1593.757	31	Base
418662.4	4117012	1596.113	32	Left
418671.2	4117026	1597.212	32	Right
418660.7	4117022	1600.234	32	Top
418670.6	4117022	1594.563	32	Base
418650.3	4117001	1600.525	33	Right
418648.4	4116992	1600.571	33	Left
418644.2	4116999	1603.477	33	Top
418650.1	4117000	1599.169	33	Base
418641.3	4116978	1599.444	34	Right
418630.7	4116967	1601.148	34	Left
418632	4116971	1603.814	34	Top
418633.9	4116971	1600.989	34	Base
418677.6	4116974	1585.11	35	Right
418653.3	4116946	1585.544	35	Left
418666.1	4116965	1586.606	35	Top
418666	4116963	1584.005	35	Base
418916	4117448	1610.144	36	Right
418711.2	4117145	1607.057	36	Left
418901.6	4117406	1614.05	36	Top
418902.9	4117406	1606.612	36	Base
418803	4117264	1604	37	Right
418646.8	4117292	1606.675	37	Left
418756.3	4117250	1604.358	37	Top
418760	4117247	1599.018	37	Base
418727.1	4117191	1601.893	38	Right
418617	4116969	1608.701	38	Left
418664.5	4117057	1610.965	38	Top
418670.9	4117055	1603.968	38	Base
418757.1	4117253	1617.223	39	Left
418818	4117292	1617.542	39	Right
418794	4117275	1619.594	39	Top
418799	4117276	1614.358	39	Base
418892.3	4117415	1618.546	40	Left

Table A.2 continued

X	Y	MSL	SS Body	Side
418903.3	4117452	1617.175	40	Right
418899.1	4117429	1618.878	40	Top
418907.3	4117426	1615.834	40	Base
418882.3	4117414	1624.076	41	Right
418634.6	4117045	1622.092	41	Left
418860.8	4117392	1625.504	41	Top
418866.3	4117392	1623.936	41	Base
418879.6	4117416	1629.456	42	Right
418629.7	4117044	1626.568	42	Left
418628.9	4117051	1628.079	42	Top
418628.3	4117048	1625.283	42	Base
418580.1	4117001	1639.943	43	Left
418868.3	4117457	1637.73	43	Right
418846.4	4117399	1642.326	43	Top
418853.7	4117398	1635.251	43	Base
418683.2	4117256	1651.29	44	Left
418705.1	4117268	1651.176	44	Right
418684.6	4117263	1654.304	44	Top
418694.8	4117263	1647.719	44	Base
418603.8	4117065	1651.86	45	Left
418607.4	4117069	1650.13	45	Right
418601.7	4117064	1652.04	45	Top
418604.8	4117065	1651.745	45	Base
418602.9	4117055	1648.861	46	Left
418601.9	4117061	1649.044	46	Right
418602.3	4117057	1650.402	46	Top
418604.1	4117056	1648.77	46	Base
418596.2	4117055	1653.926	47	Left
418598.5	4117063	1652.376	47	Right
418591.6	4117063	1655.979	47	Top
418598.9	4117060	1652.248	47	Base
418578.2	4117029	1652.327	48	Right
418561.9	4117012	1650.671	48	Left
418568.9	4117018	1653.108	48	Top
418577.6	4117019	1647.802	48	Base
418689.5	4117278	1664.547	49	Left
418848	4117452	1655.24	49	Right
418824.6	4117400	1658.856	49	Top
418825.7	4117399	1653.335	49	Base
418840.9	4117428	1662.148	50	Right
418551.9	4117029	1670.259	50	Left
418663.9	4117254	1671.916	50	Top

Table A.2 continued

X	Y	MSL	SS Body	Side
418662.3	4117255	1666.304	50	Base
418666	4117259	1661.773	51	Right
418556.5	4117030	1665.18	51	Left
418656.9	4117237	1666.064	51	Top
418660.4	4117237	1658.452	51	Base
418641	4117155	1658.882	52	Right
418626.9	4117129	1661.047	52	Left
418632.3	4117141	1662.27	52	Top
418636.2	4117141	1659.019	52	Base
418597.6	4117113	1675.721	53	Right
418552.1	4117034	1676.538	53	Left
418569.4	4117068	1676.605	53	Top
418575.9	4117067	1672.738	53	Base
418656.7	4117256	1678.68	54	Left
418825	4117443	1677.395	54	Right
418816.9	4117415	1679.844	54	Top
418820.3	4117414	1673.904	54	Base
418810.1	4117442	1691.591	55	Right
418538.8	4117043	1697.184	55	Left
418760.4	4117347	1694.719	55	Top
418763.5	4117349	1682.03	55	Base

Table A.3

Projected Channel-belt Center-Points in west Bull Canyon

		Parallel		Perpendicular	
SS Body	**DU**	**X**	**Y**	**X**	**Y**
40	2	125.48887	1456.8356	1376.977	1405.046
42	2	231.128709	1464.8898	1277.714	1413.333
43	2	205.804248	1457.1728	1315.977	1405.499
47	2	359.164281	1474.9091	1144.793	1423.425
98	2	1171.58524	1485.8041	602.2822	1429.583
99	2	1181.0858	1488.6196	571.8257	1431.066
100	2	1155.41968	1487.8085	629.5532	1428.84
101	2	1129.7225	1487.6254	644.038	1429.802
102	2	1110.45738	1487.331	674.5457	1429.785
103	2	1097.54667	1488.4951	693.8125	1429.741
104	2	1078.3592	1486.631	713.0574	1429.069
108	2	1001.85775	1474.153	802.4576	1414.208
127	2	1190.77272	1487.668	549.3587	1431.431
215	2	327.780401	1459.7695	1293.444	1403.98
217	2	305.431255	1456.8625	1333.486	1401.114
224	2	411.381648	1458.6386	1203.569	1405.232
225	2	485.264925	1459.0868	1193.836	1402.427
226	2	539.914148	1458.6129	1160.077	1401.3
228	2	607.303222	1460.4278	1124.795	1402.533
229	2	568.493481	1465.4894	1073.695	1410.606
230	2	616.632969	1466.6962	1033.601	1412.006
231	2	629.17102	1473.0659	998.5162	1418.891
238	2	677.201813	1476.4701	968.0963	1421.42
240	2	706.324643	1472.36	991.955	1414.927
241	2	719.452766	1466.8012	1027.055	1408.461
242	2	787.012691	1465.1633	988.4478	1406.455
246	2	898.556579	1483.779	849.4413	1426.193
1	3	657.868374	1542.5111	808.4579	1494.073
3	3	591.737118	1515.2696	898.9866	1465.548
10	3	512.19822	1499.2372	1017.203	1448.214
27	3	225.094238	1521.9191	1169.044	1474.145
28	3	196.74778	1510.3339	1223.213	1461.982
29	3	125.265315	1526.31	1254.328	1479.342
30	3	93.2913408	1523.0989	1283.107	1475.821
31	3	302.85345	1508.9708	1128.424	1460.471
32	3	165.363909	1495.1943	1256.394	1446.569
33	3	-25.274704	1516.5228	1335.921	1470.833
34	3	-47.468643	1510.4767	1366.253	1465.791
35	3	-34.231788	1502.7207	1364.313	1456.216

Table A.3 continued

		Parallel		Perpendicular	
SS Body	**DU**	**X**	**Y**	**X**	**Y**
36	3	-7.9290279	1490.6617	1367.031	1442.076
37	3	85.3280834	1489.207	1328.417	1439.861
38	3	2.11509626	1482.4904	1368.386	1434.902
39	3	76.9922026	1462.8487	1388.496	1413.028
41	3	195.045813	1479.7837	1263.843	1429.958
44	3	269.426055	1470.187	1242.57	1418.543
45	3	277.218369	1507.5319	1144.078	1458.726
46	3	290.781301	1493.184	1159.929	1443.02
58	3	719.44656	1531.881	780.7264	1481.626
59	3	681.444298	1520.6195	814.0614	1470.61
60	3	626.779568	1521.4073	852.6535	1472.197
61	3	622.49981	1542.9655	827.7248	1494.03
62	3	491.799517	1521.858	965.0909	1473.301
63	3	491.45787	1528.7639	957.3135	1480.491
64	3	433.351937	1534.1589	983.2	1486.085
65	3	508.648319	1506.0419	998.1773	1455.167
66	3	550.029651	1513.9518	939.0655	1463.729
67	3	550.402358	1506.418	953.2579	1456.316
68	3	567.220134	1491.2296	976.7365	1438.936
69	3	509.673237	1485.324	1039.158	1433.193
70	3	477.419762	1487.7633	1052.112	1436.304
71	3	516.477922	1477.6793	1061.355	1425.081
72	3	481.031762	1479.7031	1071.072	1427.467
73	3	1442.99888	1520.4755	320.8498	1463.098
74	3	1427.01969	1518.713	343.2948	1462.105
75	3	1475.37659	1515.5251	339.9119	1457.192
76	3	1481.49808	1521.6919	311.2639	1464.481
77	3	1504.06464	1520.2042	303.2159	1463.923
78	3	1526.50697	1521.2278	303.1647	1462.458
79	3	1507.16419	1522.503	295.2118	1464.622
80	3	1526.13429	1528.7616	276.1424	1470.319
81	3	1539.15367	1525.4002	272.8545	1468.128
82	3	1571.03446	1530.4948	234.4889	1473.031
83	3	1680.17758	1532.6859	167.066	1473.499
105	3	1049.05	1494.508	710.1424	1437.555
106	3	939.968984	1491.0612	812.7746	1433.762
107	3	998.183627	1483.4687	797.9827	1424.007
110	3	916.99868	1500.7104	803.5177	1444.566
111	3	900.771007	1503.9703	830.891	1446.754
112	3	868.424356	1508.293	853.5481	1451.833
113	3	919.554741	1513.9957	771.8961	1458.667

Table A.3 continued

		Parallel		Perpendicular	
SS Body	**DU**	**X**	**Y**	**X**	**Y**
114	3	851.761888	1520.3423	823.5303	1465.877
115	3	864.253316	1527.6537	809.3232	1472.872
116	3	841.640165	1530.0832	812.6111	1475.063
117	3	879.952998	1535.0666	764.689	1482.186
118	3	883.052574	1537.3652	748.6808	1483.584
119	3	863.601104	1540.8377	764.8791	1487.63
120	3	857.293271	1538.4376	777.6432	1485.297
121	3	909.308787	1526.2478	717.8222	1473.551
122	3	922.002079	1529.4786	709.8839	1476.134
123	3	974.266061	1512.2662	686.7735	1458.076
124	3	1045.60881	1499.1152	647.7427	1443.927
125	3	1058.31764	1502.0319	628.5709	1446.692
126	3	1135.50236	1500.6981	548.2522	1445.724
128	3	1180.52677	1499.9202	516.1481	1446.007
129	3	1209.38562	1501.1464	468.0431	1447.896
130	3	1244.69206	1501.9477	394.2271	1449.216
131	3	1257.6649	1499.528	451.8887	1445.106
132	3	1279.81217	1506.5158	410.3669	1451.587
133	3	1283.09808	1505.0477	485.7208	1448.327
134	3	1273.55093	1503.174	493.6664	1445.953
135	3	1283.23784	1502.2225	512.8748	1444.234
136	3	1315.38261	1501.9807	500.001	1443.426
137	3	1341.00215	1503.7334	463.1515	1445.761
138	3	1347.10811	1510.2143	444.1039	1452.086
139	3	1321.41092	1510.031	450.592	1453.956
140	3	1321.25564	1513.1702	450.6578	1455.84
141	3	1356.40681	1517.1105	420.3037	1460.254
142	3	1362.68356	1520.1383	404.3833	1464.164
178	3	986.012106	1534.6451	583.3052	1483.909
179	3	1086.6951	1512.9894	505.4629	1461.892
180	3	1108.74921	1521.8606	467.2436	1470.982
181	3	1147.45027	1518.9963	425.4074	1468.461
202	3	1272.77449	1518.8693	295.3654	1469.019
203	3	1295.62056	1511.7314	330.3772	1460.04
206	3	244.427606	1455.878	1372.013	1400.817
213	3	211.879099	1464.2814	1359.526	1411.105
214	3	256.981193	1461.9339	1343.328	1407.059
227	3	426.770805	1472.3293	1144.683	1420.285
232	3	800.786806	1511.5004	847.3232	1457.5
233	3	762.427368	1507.4588	872.888	1453.882
234	3	752.662825	1509.9797	861.7057	1455.53

Table A.3 continued

		Parallel		Perpendicular	
SS Body	**DU**	**X**	**Y**	**X**	**Y**
235	3	778.732686	1502.6291	879.069	1446.958
236	3	705.517167	1488.683	907.5562	1435.063
237	3	696.187417	1482.4147	920.1668	1428.335
239	3	754.13806	1480.1588	940.8692	1423.419
243	3	865.94595	1493.438	836.9916	1437.528
2	4	596.243589	1554.0828	836.1968	1506.73
4	4	721.567823	1553.9557	754.2451	1504.98
5	4	515.726369	1557.8265	902.1403	1509.877
6	4	531.208668	1569.6339	880.1119	1522.805
7	4	368.922641	1537.4678	1044.369	1490.447
8	4	403.576871	1551.4531	1003.118	1504.674
9	4	435.644013	1552.7807	974.2502	1505.682
14	4	289.035909	1593.421	1033.557	1548.68
19	4	254.707766	1572.8438	1090.59	1526.565
20	4	206.49058	1573.2065	1132.367	1527.411
21	4	202.785445	1583.1501	1127.892	1537.21
22	4	84.4522889	1571.8653	1204.631	1527.613
23	4	36.8097527	1560.6137	1237.98	1517.016
24	4	149.471684	1556.6281	1165.527	1511.37
25	4	227.184364	1544.6216	1137.759	1497.876
26	4	147.024351	1541.1454	1200.268	1494.645
48	4	507.399851	1596.234	856.9917	1550.443
49	4	558.607835	1600.3674	821.7824	1553.769
50	4	594.395679	1591.4375	798.9937	1544.922
51	4	671.968611	1582.2561	750.4867	1535.297
52	4	688.413683	1574.6015	738.968	1527.314
84	4	1728.20841	1536.0902	122.2343	1477.161
85	4	1660.66399	1537.4141	162.4522	1479.32
86	4	1544.70061	1543.1817	210.9153	1487.689
87	4	1627.35456	1561.1989	71.91622	1507.636
88	4	1313.87631	1532.4294	244.4623	1482.745
89	4	1382.08224	1582.6873	146.69	1533.743
90	4	1456.26055	1577.1714	131.9858	1526.5
91	4	1446.86869	1572.1587	135.0543	1522.41
92	4	1603.28173	1593.1354	82.64996	1539.124
93	4	1625.9104	1590.3921	101.8291	1536.567
94	4	1693.05102	1597.2297	60.28527	1542.42
95	4	1696.47667	1592.9363	60.09518	1536.976
97	4	1423.43252	1591.2251	119.7261	1543.279
152	4	1481.80248	1580.4936	130.499	1529.906
153	4	1494.09202	1591.8859	111.6342	1541.465

Table A.3 continued

		Parallel		Perpendicular	
SS Body	**DU**	**X**	**Y**	**X**	**Y**
154	4	1035.52748	1572.9941	432.2219	1525.659
155	4	938.875773	1578.1142	522.3093	1530.478
156	4	947.522251	1598.1944	438.0274	1553.964
157	4	935.139522	1588.6857	501.8335	1541.884
158	4	883.807284	1587.0636	601.2436	1537.783
163	4	873.716614	1596.1767	620.8394	1547.161
170	4	881.810262	1562.4776	661.3523	1511.788
171	4	888.552901	1556.0884	662.7221	1505.032
172	4	904.873739	1550.9451	643.2725	1499.842
173	4	930.369046	1555.209	598.4993	1505.178
174	4	933.297798	1560.9606	589.0816	1511.377
175	4	965.706554	1555.3825	547.1357	1505.714
176	4	962.777811	1549.6307	551.7495	1499.894
177	4	976.030147	1541.5608	570.702	1490.847
182	4	1013.41126	1565.3784	423.9546	1518.82
183	4	1100.09654	1566.8601	324.4787	1521.036
184	4	1083.86886	1570.1201	311.7804	1525.253
185	4	1131.83755	1574.7798	254.1261	1529.572
186	4	1176.34953	1584.3606	199.9132	1540.479
187	4	1217.94827	1587.8759	169.5006	1543.218
188	4	1096.06524	1583.3958	276.9587	1539.675
189	4	1089.30708	1590.0989	282.0185	1546.625
190	4	1098.49707	1599.1923	243.8284	1556.553
193	4	1355.58377	1533.7473	228.381	1482.049
194	4	1384.34946	1536.8572	217.2572	1485.372
195	4	1259.1184	1535.1008	235.008	1487.896
196	4	1281.35886	1540.2052	227.1502	1492.782
197	4	1409.37889	1550.5383	184.01	1498.9
198	4	1448.2818	1543.5933	201.4099	1491.375
199	4	1365.79245	1587.203	138.8614	1539.466
200	4	1304.99069	1582.1376	153.2366	1537.287
201	4	1266.55364	1579.6656	162.7859	1534.858
11	5	124.109978	1614.6188	1153.17	1571.334
12	5	249.651618	1610.097	1074.308	1566.123
13	5	240.182097	1606.6539	1058.139	1562.914
16	5	149.403376	1622.9635	1124.543	1579.251
17	5	162.516016	1617.7188	1124.353	1573.808
18	5	301.7292	1596.6518	1030.43	1551.095
54	5	657.225516	1620.4609	700.5195	1575.821
96	5	1551.15752	1607.5225	65.60097	1556.698
151	5	1332.59173	1608.7904	112.3654	1562.402

Table A.3 continued

		Parallel		Perpendicular	
SS Body	**DU**	**X**	**Y**	**X**	**Y**
159	5	905.395526	1605.3519	499.2548	1560.001
160	5	914.771859	1610.6786	473.7631	1565.713
161	5	866.756592	1606.9605	584.3628	1560.174
162	5	847.243007	1611.6887	631.0175	1562.737
164	5	792.795667	1608.0818	714.3829	1558.987
165	5	904.867545	1616.0247	483.5756	1570.82
166	5	981.834859	1619.0856	353.6944	1575.985
191	5	1069.0947	1608.9528	268.2501	1566.181
15	6	174.557062	1634.1334	1100.868	1590.978
53	6	695.165645	1632.978	665.61	1587.731
55	6	634.457051	1626.0293	724.7949	1581.262
56	6	582.92295	1628.4881	765.0493	1584.468
57	6	524.98784	1630.4302	813.264	1585.719
144	6	1621.33561	1617.9143	93.15708	1564.121
147	6	1611.22942	1627.3412	63.00766	1574.397
148	6	1604.53335	1632.7888	55.19364	1580.539
149	6	1585.42352	1629.3554	56.70235	1577.761
150	6	1300.43143	1609.346	200.6517	1561.625
167	6	868.660436	1633.43	506.6787	1588.67
168	6	826.937453	1632.426	618.9772	1585.796
169	6	752.790197	1637.3141	718.6212	1588.395
192	6	1109.52879	1636.0108	208.1779	1593.224
204	6	1434.40213	1629.2992	72.88598	1581.389
205	6	1459.46264	1642.3525	73.30272	1593.322
248	6	476.941511	1627.3399	872.5586	1582.391

Table A.4

Projected Channel-belt Center-Points in Rock House Cove

		Parallel		Perpendicular	
SS Body	**DU**	**X**	**Y**	**X**	**Y**
1	1	255.7449	1489.934	458.888	1489.702
2	2	208.7707	1511.666	331.4203	1511.32
3	2	390.192	1521.067	262.435	1520.887
4	2	298.3669	1526.688	283.4414	1526.083
5	2	215.7784	1502.135	410.8975	1501.746
6	3	511.9846	1537.124	133.8432	1537.973
7	3	479.8141	1540.322	152.6301	1540.679
8	3	512.1192	1559.089	95.2803	1559.3
9	3	560.0522	1565.671	54.445	1565.9
10	3	376.1928	1542.776	203.9964	1543.134
11	3	395.0616	1546.997	197.9397	1547.217
12	3	373.8845	1550.452	187.4614	1550.396
13	3	290.6877	1554.744	233.3144	1554.895
14	3	400.6402	1560.49	157.685	1560.388
15	3	287.5196	1550.248	210.103	1550.607
16	3	251.3489	1541.275	271.3583	1541.272
17	3	258.4539	1547.622	248.1967	1548.54
18	3	242.0556	1562.188	244.9402	1561.684
19	3	187.8985	1564.872	278.6367	1564.378
20	3	129.6357	1538.185	353.0728	1538.267
21	3	124.9656	1544.804	348.1292	1544.389
22	3	81.8099	1549.068	386.8016	1548.439
23	3	116.4136	1558.57	335.49	1558.672
24	3	96.02805	1563.083	341.5829	1562.973
25	3	96.84236	1567.846	345.4689	1567.728
26	3	57.66743	1581.105	350.4954	1580.866
27	3	80.19261	1541.395	417.1419	1541.166
28	4	415.6386	1573.711	100.3108	1573.344
29	4	435.3072	1580.313	97.0298	1580.824
30	4	389.827	1589.606	113.6362	1590.102
31	4	324.696	1595.209	131.8816	1595.3
32	4	71.89694	1596.973	304.1772	1596.534
33	4	44.44043	1600.697	319.6557	1600.375
34	4	17.74632	1600.716	335.6679	1599.91
35	4	32.5744	1586.15	359.3514	1585.618
36	5	363.2481	1608.414	97.7003	1608.24
37	5	282.3595	1605.03	84.4345	1605.304
38	5	115.9156	1605.41	248.4391	1604.731

Table A.4 continued

		Parallel		Perpendicular	
SS Body	**DU**	**X**	**Y**	**X**	**Y**
39	5	326.4042	1617.702	110.9904	1616.84
40	5	514.0512	1618.1	0	1617.827
41	5	277.7607	1623.293	141.3875	1622.709
42	5	274.6495	1628.058	138.6479	1627.696
43	5	251.9458	1638.659	129.3072	1638.578
44	5	249.6635	1650.569	88.4964	1650.843
45	5	56.52545	1650.968	238.6948	1650.054
46	5	47.87614	1648.857	245.3116	1647.784
47	5	44.76161	1653.094	243.1242	1652.77
48	5	0	1651.537	268.5181	1650.939
49	6	372.1991	1659.746	18.95504	1659.504
50	6	230.1328	1666.461	120.037	1665.775
51	6	110.7766	1663.633	168.0675	1663.021
52	6	126.4563	1659.917	179.0951	1659.161
53	6	36.26317	1675.593	221.6847	1675.217
54	6	342.4748	1677.762	22.8987	1677.627

APPENDIX B

DERIVATIONS OF POINT PATTERN ANALYSIS METHODS

Quadrat Method Derivation

The quadrat method uses the Pearson X^2 goodness-of-fit to test whether point-counts in the different quadrats are truly Poisson distributed (Smith, 2014). In simple terms, this statistic compares observed point-counts to the expected point-count under CSR and is given by:

$$X^2 = \sum_{i=1}^{m} \frac{(O(PC(Qi)) - E(PC))^2}{E(PC)} \tag{B.1}$$

where $PC(Qi)$ is the point-count of quadrat Qi, $O(PC(Qi))$ is the observed point-count in quadrat Qi, and $E(PC)$ is the expected point-count under CSR (i.e., same for all quadrats under CSR). The expected point-count is given by

$$E(PC|D) = area(Q) * D = area(Q) * \frac{n}{area(R)} \tag{B.2}$$

and since $area(Q) = \frac{area(R)}{m}$, the expected point-count becomes:

$$E(PC|D) = \frac{n}{m} = \bar{n} \tag{B.3}$$

where $\bar{n}$ is the sample mean of all point-counts. Therefore, the X^2 statistic becomes:

$$X^2 = \sum_{i=1}^{m} \frac{(O(PC(Qi)) - \bar{n})^2}{\bar{n}} = (m-1)\frac{s^2}{\bar{n}} \tag{B.4}$$

where $s^2 = \frac{1}{m-1}\sum_{i=1}^{m}(O(PC(Qi)) - \bar{n})^2$ is the sample variance of the point-count distribution. Since the number of quadrats m is a constant, the X^2 statistic reduces to the ratio of variance over mean $\frac{s^2}{\bar{n}}$.

Nearest-Neighbor Method Derivation

Mean Nearest-Neighbor Distance under CSR

Given a random point s_i within a random point pattern, the probability that the random variable N – denoting the NN distance of s_i – be as large as a random distance d is the probability that the point-count PC within a circle C centered around s_i with a radius d is zero such that:

$$Pr(N > d) = \Pr(PC(C_d) = 0) \tag{B.5}$$

where N is a random variable indicating the nearest-neighbor distance of random point s_i, C_d is the circle centered around s_i with radius d, and $PC(C_d)$ is the point-count within circle C_d. Since the CSR hypothesis asserts that the number of points within a given subregion is Poisson distributed, it follows that:

$$\begin{aligned} Pr(N > d) = \Pr(PC(C_d) = 0) &= \frac{D * area(C_d)^0}{0!}\, e^{-D*area(C_d)} \\ &= e^{-D*area(C_d)} \end{aligned} \tag{B.6}$$

Hence, the cumulative distribution function CDF of the nearest-neighbor distance is given by:

$$CDF(d) = Pr(N \leq d) = 1 - Pr(N > d) = 1 - e^{-D*area(C)} \tag{B.7}$$

By differentiating the CDF, we can obtain the probability density function PDF of the nearest-neighbor distance as follows (Smith, 2014):

$$PDF(d) = CDF'(d) = 2D\pi d e^{-D\pi d^2} \tag{B.8}$$

The expected mean (E) and variance (Var) of this distribution are given by:

$$E(N) = \frac{1}{2\sqrt{D}} \qquad Var(N) = \frac{4-\pi}{4D\pi} \tag{B.9}$$

The Clark-Evans test (Clark and Evans, 1954) uses a normal approximation to the sample mean of N. To approximate the sample mean of N, this test relies on the Central Limit Theorem, which states that the mean of independently and identically distributed random variables $Ni: i = 1, \ldots, n$ is approximately normally distributed. Therefore, the sample mean of N is normally distributed and is giving by:

$$\bar{N} = \frac{1}{n}\sum_{i=1}^{n} Ni \tag{B.10}$$

where $\bar{N}$ is the sample mean of all nearest-neighbor distributions, Ni is the nearest-neighbor distribution of point s_i, and n is the total number of points. Using Eq. B.9, the expected mean and variance of the sample mean of all nearest-neighbor distributions is therefore:

$$E(\bar{N}) = \frac{1}{n}\sum_{i=1}^{n} E(Ni) = \frac{1}{2\sqrt{D}} \qquad Var(\bar{N}) = \frac{1}{n}\sum_{i=1}^{n} Var(Ni) = \frac{4-\pi}{n(4D\pi)} \tag{B.11}$$

The Clark-Evans test also involves standardizing the sample mean as follows:

$$Std(\bar{N}) = \frac{(\bar{N} - E(\bar{N}))}{\sigma(\bar{N})} \tag{B.12}$$

where $\sigma(\bar{N})$ is the standard error of $\bar{N}$ and is giving by (Bailey and Gatrell, 1995)

$$\sigma(\bar{N}) = \sqrt{Var(\bar{N})} = \sqrt{\frac{4-\pi}{n(4D\pi)}} \tag{B.13}$$

Thus, the standardized sample mean is approximated by a standard normal distribution

with a mean of 0 and a standard deviation of 1 (Figure 8).

Point Pattern Mean Nearest-Neighbor Distance

To test the CSR hypothesis, the Clark-Evans test (1954) involves calculating the mean of all nearest-neighbor distances within a point pattern and evaluating how it compares to the sample mean of NN distances under CSR (derivation shown above). Given the point pattern Sn with points $(si: 1, \dots, n)$, the mean NN distance is given by:

$$\overline{dm} = \frac{1}{n}\sum_{i=1}^{n} di \tag{B.14}$$

where $\overline{dm}$ is the mean NN distance, and di is the NN-distance of point si. The standardized mean NN distance is calculated using the expected mean $E(\bar{N})$ and standard deviation $\sigma(\bar{N})$ equations of the sample mean of all NN distributions under CSR (Eq. B.11 and Eq. B.13 in Appendix B) as follows:

$$Std(\overline{dm}) = \frac{(\overline{dm} - E(\bar{N}))}{\sigma(\bar{N})} \tag{B.15}$$

K-Function Derivation under CSR

Edge Effects

This standard K-function estimation assumes the point pattern is stationary. However, this does not hold true in bounded regions. As can be seen in Figure 9A, the points outside the study region (i.e., in red) are not counted as part of the point count of the point s_i. In our case, this limitation is due to the limited lateral extent of the outcrop. This has the effect of decreasing the number of expected points inside the region. To counter this downward bias, Ripley (1976) introduced a correction that consists in adding a weighting factor for each point s_i so that it inflates the counts for points near the

boundary. With that, the estimation of the K function becomes:

$$K(h) = \frac{1}{D}\left[\frac{1}{n}\sum_{i=1}^{n}\left(\sum_{i\neq j}\frac{I_h(d_{ij})}{w_{(s_i,s_j)}}\right)\right] \quad \text{(B.16)}$$

where $w_{(s_i,s_j)}$ is the weighting factor and is defined as the proportion of the circle, centered at s_i and passing through s_j, which lies inside the study region R, as shown in Figure 9B.

K-function under CSR

To characterize the K-function under CSR, the expected number of points within a circle of radius h (represented by the expression in brackets in the equation above) needs to be quantified for random point patterns. As demonstrated before, the expected point count in region R under CSR follows a Poisson distribution and is therefore proportional to the area of region R as follows:

$$D = \frac{E(h)}{a(h)} \quad \text{(B.17)}$$

where D is the average point density, $E(h)$ is the expected point count in a circle of radius h, and $a(h)$ is the area of a circle of radius h. Hence, the K-function simply reduces to the circle area under CSR as follows:

$$K(h) = \frac{E(h)}{D} = \frac{D * a(h)}{D} = a(h) = \pi h^2 \quad \text{(B.18)}$$

CSR Test

Testing the CSR hypothesis involves comparing the pattern's K-function for a given scale to the area of a circle of the same scale as follows (Smith, 2014):

- $K(h) > \pi h^2$, clustering at scale h (mean point count higher than expected under

CSR)

- $K(h) < \pi h^2$, dispersion at scale h (mean point count lower than expected under CSR)

For practical purposes, K-function can be standardized to an L-function as follows,

$$L(h) = \sqrt{\frac{K(h)}{\pi}} - h \tag{B.19}$$

- When $L(h) > 0$, the pattern is clustered at scale h
- When $L(h) < 0$, the pattern is dispersed at scale h

APPENDIX C

MATLAB SCRIPTS FOR POINT PATTERN ANALYSIS METHODS

Matlab scripts are provided for all point pattern analysis techniques described in the Methods section. For each technique, script files are listed in the order in which they are called starting with the main script entry file. For each method, basic instructions are included to outline the key input parameters needed for the script to be executed. The code also includes comments (green) that document the different steps involved in the execution of a given point pattern analysis technique.

Quadrat Method

To use the quadrat method on a new dataset, provide these input parameters in the 'Quadrat.m' script file:

1. Load coordinates of channel-belt center-points in the 'points' array
2. Define index limits of each DU within the 'points' array
3. Define width and height of study region, and cell width and height
4. Define the minimum Y value for each DU
5. Define the number of rows covering each DU based on total thickness of DU
6. Assign proper indexing of cells in each DU based on the number of rows used
7. Run and debug

Quadrat.m

```
%Filename: Quadrat.m
%Author: Wassim Benhallam
%Version: 1.0
%Description: Calculate variance/mean ratios for depositional units

%Provide coordinates of channel-belt center-points, [X Y]
points = [ ];

%Specify Index limits each depositional unit
[DU0] = points(1:3,:);
[DU1] = points(4:9,:);
[DU2] = points(10:35,:);
[DU3] = points(36:54,:);
[DU4] = points(55:98,:);
[DU5] = points(99:121,:);
[DU6] = points(122:136,:);

%Construct a grid for each depositional unit
Rx = 2500;  %study region width
Ry = 250;   %study region height
cw = 100;   %grid cell width
ch = 25;    %grid cell height

%Create a grid (array of cells) for each unit
cellsDU0 = Cell();
cellsDU1 = Cell();
cellsDU2 = Cell();
cellsDU3 = Cell();
cellsDU4 = Cell();
cellsDU5 = Cell();
cellsDU6 = Cell();

%Define base elevation for each DU
minYs = [1360   %DU0
        1375   %DU1
        1380   %DU2
        1410   %DU3
        1450   %DU4
        1520   %DU5
        1560]; %DU6

%Populate grid cells of each DU with location, width, and height information
walker = 1;
minX = floor(min(DU0(:,1))/100)+1;
maxX = floor(max(DU0(:,1))/100)+1;
for i=minX:maxX %DU0 400*50 = 20000
    cellsDU0(walker) = Cell(i*cw – cw, minYs(1), cw, ch);
    cellsDU0(walker + 1) = Cell(i*cw – cw, minYs(1)+ch, cw, ch);
    walker = walker + 2;
end

walker = 1;
minX = floor(min(DU1(:,1))/100)+1;
maxX = floor(max(DU1(:,1))/100)+1;
```

```
for i=minX:maxX  %DU1 900*50 = 45000
    cellsDU1(walker) = Cell(i*cw – cw, minYs(2), cw, ch);
    cellsDU1(walker + 1) = Cell(i*cw – cw, minYs(2)+ch, cw, ch);
    walker = walker + 2;
end

walker = 1;
minX = floor(min(DU2(:,1))/100)+1;
maxX = floor(max(DU2(:,1))/100)+1;
for i=minX:maxX  %DU2 1500*50 = 75000
    cellsDU2(walker) = Cell(i*cw – cw, minYs(3), cw, ch);
    cellsDU2(walker + 1) = Cell(i*cw – cw, minYs(3)+ch, cw, ch);
    walker = walker + 2;
end

walker = 1;
minX = floor(min(DU3(:,1))/100)+1;
maxX = floor(max(DU3(:,1))/100)+1;
for i=minX:maxX  %DU3 1500*50 = 75000
    cellsDU3(walker) = Cell(i*cw – cw, minYs(4), cw, ch);
    cellsDU3(walker + 1) = Cell(i*cw – cw, minYs(4)+ch, cw, ch);
    walker = walker + 2;
end

walker = 1;
minX = floor(min(DU4(:,1))/100)+1;
maxX = floor(max(DU4(:,1))/100)+1;
for i=minX:maxX  %DU4 1900*100 = 190000
    cellsDU4(walker) = Cell(i*cw – cw, minYs(5), cw, ch);
    cellsDU4(walker + 1) = Cell(i*cw – cw, minYs(5)+ch, cw, ch);
    cellsDU4(walker + 2) = Cell(i*cw – cw, minYs(5)+(2*ch), cw, ch);
    cellsDU4(walker + 3) = Cell(i*cw – cw, minYs(5)+(3*ch), cw, ch);
    walker = walker + 4;
end

walker =1;
minX = floor(min(DU5(:,1))/100)+1;
maxX = floor(max(DU5(:,1))/100)+1;
for i=minX:maxX  %DU5 1500*50 = 75000
    cellsDU5(walker) = Cell(i*cw – cw, minYs(6), cw, ch);
    cellsDU5(walker + 1) = Cell(i*cw – cw, minYs(6)+ch, cw, ch);
    walker = walker + 2;
end

walker = 1;
minX = floor(min(DU6(:,1))/100)+1;
maxX = floor(max(DU6(:,1))/100)+1;
for i=minX:maxX  %DU6 1000*25 = 25000
    cellsDU6(walker) = Cell(i*cw – cw, minYs(7), cw, ch);
    walker = walker + 1;
end

%Count number of centerpoints within grid cells of each DU
%DU0 count
for i=1:length(DU0)
  x = floor(DU0(I,1)/100)*100;
```

```
  minX = floor(min(DU0(:,1))/100)*100
  column = ((x – minX)/100 + 1)*2;
  if(DU0(I,2) < minYs(1)+ch)
     index = column-1;
  else
     index = column;
  end
  cellsDU0(index) = cellsDU0(index).incrementCount();
end

%DU1 count
for i=1:length(DU1)
  x = floor(DU1(I,1)/100)*100;
  minX = floor(min(DU1(:,1))/100)*100
  column = ((x – minX)/100 + 1)*2;
  if(DU1(I,2) < minYs(2)+ch)
     index = column-1;
  else
     index = column;
  end
  cellsDU1(index) = cellsDU1(index).incrementCount();
end

%DU2 count
for i=1:length(DU2)
  x = floor(DU2(I,1)/100)*100;
  minX = floor(min(DU2(:,1))/100)*100
  column = ((x – minX)/100 + 1)*2;
  if(DU2(I,2) < minYs(3)+ch)
     index = column-1;
  else
     index = column;
  end
  cellsDU2(index) = cellsDU2(index).incrementCount();
end

%DU3 count
for i=1:length(DU3)
  x = floor(DU3(I,1)/100)*100;
  minX = floor(min(DU3(:,1))/100)*100
  column = ((x – minX)/100 + 1)*2;
  if(DU3(I,2) < minYs(4)+ch)
     index = column-1;
  else
     index = column;
  end
  cellsDU3(index) = cellsDU3(index).incrementCount();
end

%DU4 count
for i=1:length(DU4)
  x = floor(DU4(I,1)/100)*100;
  minX = floor(min(DU4(:,1))/100)*100
  column = ((x – minX)/100 + 1)*4;
  if(DU4(I,2) < minYs(5)+ch)
     index = column – 3;
```

```
  else if(DU4(I,2) < minYs(5)+(2*ch))
        index = column – 2;
    else if(DU4(I,2) < minYs(5)+(3*ch))
        index = column – 1;
      else
        index = column;
      end
    end
  end
  cellsDU4(index) = cellsDU4(index).incrementCount();
end

%DU5 count
for i=1:length(DU5)
  x = floor(DU5(I,1)/100)*100;
  minX = floor(min(DU5(:,1))/100)*100
  column = ((x – minX)/100 + 1)*2;
  if(DU5(I,2) < minYs(6)+ch)
    index = column-1;
  else
    index = column;
  end
  cellsDU5(index) = cellsDU5(index).incrementCount();
end

%DU6 count
for i=1:length(DU6)
  x = floor(DU6(I,1)/100)*100;
  minX = floor(min(DU6(:,1))/100)*100
  column = ((x – minX)/100 + 1);
  index = column;
  cellsDU6(index) = cellsDU6(index).incrementCount();
end

%Compute the expected random cell count for each unit
meanDU0 = length(DU0)/length(cellsDU0);
meanDU1 = length(DU1)/length(cellsDU1);
meanDU2 = length(DU2)/length(cellsDU2);
meanDU3 = length(DU3)/length(cellsDU3);
meanDU4 = length(DU4)/length(cellsDU4);
meanDU5 = length(DU5)/length(cellsDU5);
meanDU6 = length(DU6)/length(cellsDU6);

%Calculate ratio of variance/mean for each unit
sum = 0;
for i=1:length(cellsDU0)
   sum = sum + (cellsDU0(i).count – meanDU0)^2;
end
variance = sum/(length(cellsDU0) – 1);
ratioDU0 = variance/meanDU0;

sum = 0;
for i=1:length(cellsDU1)
   sum = sum + (cellsDU1(i).count – meanDU1)^2;
end
variance = sum/(length(cellsDU1) – 1);
```

```
ratioDU1 = variance/meanDU1;

sum = 0;
for i=1:length(cellsDU2)
   sum = sum + (cellsDU2(i).count – meanDU2)^2;
end
variance = sum/(length(cellsDU2) – 1);
ratioDU2 = variance/meanDU2;

sum = 0;
for i=1:length(cellsDU3)
   sum = sum + (cellsDU3(i).count – meanDU3)^2;
end
variance = sum/(length(cellsDU3) – 1);
ratioDU3 = variance/meanDU3;

sum = 0;
for i=1:length(cellsDU4)
   sum = sum + (cellsDU4(i).count – meanDU4)^2;
end
variance = sum/(length(cellsDU4) – 1);
ratioDU4 = variance/meanDU4;

sum = 0;
for i=1:length(cellsDU5)
   sum = sum + (cellsDU5(i).count – meanDU5)^2;
end
variance = sum/(length(cellsDU5) – 1);
ratioDU5 = variance/meanDU5;

sum = 0;
for i=1:length(cellsDU6)
   sum = sum + (cellsDU6(i).count – meanDU6)^2;
end
variance = sum/(length(cellsDU6) – 1);
ratioDU6 = variance/meanDU6;

[ratio] =   [   ratioDU0 minYs(1)
              ratioDU1 minYs(2)
              ratioDU2 minYs(3)
              ratioDU3 minYs(4)
              ratioDU4 minYs(5)
              ratioDU5 minYs(6)
              ratioDU6 minYs(7)];

%Plot variance/mean ratios for each unit
[P,S] = polyfit(ratio(:,1),ratio(:,2), 10);
TT = polyval(P, ratio(:,1));
plot(ratio(:,1),ratio(:,2),'bx', ratio(:,1), TT, 'linewidth', 3, 'color', 'black');
t = text(ratio(1,1)+0.03,ratio(1,2)+10,'DU0');
t = text(ratio(2,1),ratio(2,2)+10,'DU1');
t = text(ratio(3,1)+0.03,ratio(3,2),'DU2');
t = text(ratio(4,1)+0.03,ratio(4,2),'DU3');
t = text(ratio(5,1)+0.03,ratio(5,2),'DU4');
t = text(ratio(6,1),ratio(6,2)+10,'DU5');
t = text(ratio(7,1),ratio(7,2),'DU6');
```

```
xlabel('Variance/mean');
ylabel('y');

%Plot center-points
figure
scatter(points(:,1), points(:,2), 20 ,points(:,3), 'filled');

%Plot grid boundaries for each unit
for i=1:length(cellsDU0)
   rectangle('Position', [cellsDU0(i).x, cellsDU0(i).y, cellsDU0(i).width, cellsDU0(i).height]);
end
for i=1:length(cellsDU1)
   rectangle('Position', [cellsDU1(i).x, cellsDU1(i).y, cellsDU1(i).width, cellsDU1(i).height]);
end
for i=1:length(cellsDU2)
   rectangle('Position', [cellsDU2(i).x, cellsDU2(i).y, cellsDU2(i).width, cellsDU2(i).height]);
end
for i=1:length(cellsDU3)
   rectangle('Position', [cellsDU3(i).x, cellsDU3(i).y, cellsDU3(i).width, cellsDU3(i).height]);
end
for i=1:length(cellsDU4)
   rectangle('Position', [cellsDU4(i).x, cellsDU4(i).y, cellsDU4(i).width, cellsDU4(i).height]);
end
for i=1:length(cellsDU5)
   rectangle('Position', [cellsDU5(i).x, cellsDU5(i).y, cellsDU5(i).width, cellsDU5(i).height]);
end
for i=1:length(cellsDU6)
   rectangle('Position', [cellsDU6(i).x, cellsDU6(i).y, cellsDU6(i).width, cellsDU6(i).height]);
end
```

Cell.m

```
%Filename: Cell.m
%Author: Wassim Benhallam
%Version: 1.0
%Description: define grid cell

classdef Cell
   properties
      x;
      y;
      width;
      height;
      count = 0;
   end


   methods
      %constructor
      function obj = Cell(x,y,width,height)
         if nargin ~= 0
            obj.x = x;
            obj.y = y;
            obj.width = width;
```

```
            obj.height = height;

        end
    end

    function c = getCount(obj)
        c = obj.count;
    end

    function obj = incrementCount(obj)
        obj.count = obj.count + 1;
    end
    function obj = resetCount(obj)
        obj.count = 0;
    end

    function inside = isPointInside(obj,x,y)
        if(x >= obj.x && x <= obj.x + obj.width && y >= obj.y && y <= obj.y + obj.height)
            inside = true;
        else
            inside = false;
        end
    end

  end
end
```

Nearest-Neighbor Method

To use the nearest-neighbor method on a new dataset, provide these input parameters in the 'NNMethod.m' script file:

1. Load coordinates of channel-belt center-points in the 'points' array
2. Define additional depositional units or remove existing ones depending on how many units are defined in your outcrop
3. Calculate the area of new depositional units
4. Run and debug

NNMethod.m

```
%Filename: NNMethod.m
%Author: Wassim Benhallam
%Version: 1.0
%Description: Calculate mean NN-distance for each unit

%Steps for clark evans test
   % 1- Calculate nn-distance for each point in the patterns
   % 2- Compute sample mean NN-distance and compare to CSR mean
   % 3- Standardize the sample mean and compare to to Z (alpha/2) for various
   % 4- Plot levels of signficance alpha for both clustering and dispersion.

%Provide coordinates of channel-belt center-points, [X Y]
points = [  ];

%Specify begining and ending indices for each depositional unit
[DU0] = points(1:3,:);
[DU1] = points(4:9,:);
[DU2] = points(10:35,:);
[DU3] = points(36:54,:);
[DU4] = points(55:98,:);
[DU5] = points(99:121,:);
[DU6] = points(122:136,:);

%Specify area of each DU
areaDU0 = (max(DU0(:,1)) - min(DU0(:,1)))*(max(DU0(:,2)) - min(DU0(:,2)));
areaDU1 = (max(DU1(:,1)) - min(DU1(:,1)))*(max(DU1(:,2)) - min(DU1(:,2)));
areaDU2 = (max(DU2(:,1)) - min(DU2(:,1)))*(max(DU2(:,2)) - min(DU2(:,2)));
areaDU3 = (max(DU3(:,1)) - min(DU3(:,1)))*(max(DU3(:,2)) - min(DU3(:,2)));
areaDU4 = (max(DU4(:,1)) - min(DU4(:,1)))*(max(DU4(:,2)) - min(DU4(:,2)));
areaDU5 = (max(DU5(:,1)) - min(DU5(:,1)))*(max(DU5(:,2)) - min(DU5(:,2)));
areaDU6 = (max(DU6(:,1)) - min(DU6(:,1)))*(max(DU6(:,2)) - min(DU6(:,2)));
totArea = (max(points(:,1)) - min(points(:,1)))*(max(points(:,2)) - min(points(:,2)));
areas = [areaDU0, areaDU1, areaDU2, areaDU3, areaDU4, areaDU5, areaDU6, totArea];

%Plot normal bell curve (covers more than 99% of the curve)
ix = -5:0.001:5;
iy = pdf('normal', ix, 0, 1);
h = plot(ix,iy);

for k=1:length(areas)
   %set your pattern parameters
   if(k == 1)
      pattern = DU0;
   elseif(k == 2)
      pattern = DU1;
   elseif(k == 3)
      pattern = DU2;
   elseif(k == 4)
      pattern = DU3;
   elseif(k == 5)
      pattern = DU4;
   elseif(k == 6)
      pattern = DU5;
```

```
elseif(k == 7)
   pattern = DU6;
elseif(k == 8)
   pattern = points;
end

area = areas(k);
n = length(pattern);
landa = length(pattern)/totArea;

%compute nn-distance for each point in the pattern
for i=1:n
   minD = 1000;
   for j=1:n
      if(i ~= j)
         distance = sqrt((pattern(i,1) - pattern(j,1))^2 + (pattern(i,2) - pattern(j,2))^2);
         if(distance < minD)
            minD = distance;
         end
      end
   end
   pattern(i,4) = minD;
end

%Compute sample mean value, replace n by m later
sum = 0;
for i=1:n
   sum = sum + pattern(i,4);
end
mean = sum/n;

%Standardize sample mean
E = 1/(2*sqrt(landa));
stdDev = sqrt((4 - pi)/(n*4*pi*landa));
stdMean = (mean - E)/stdDev;
fprintf('pattern: %d with stdMean = %f\n',k, stdMean);

%One tailed CSR test using upper and lower tails
if(stdMean > 0)
   if(stdMean >= 2.33)
      display('Strong dispersion at the 0.01 significance level');
   elseif(stdMean >= 1.65)
      display('Standard dispersion at the 0.05 significance level');
   else
      display('Weak dispersion at the 0.1 significance level');
   end
else
   if(stdMean < -2.33)
      display('Strong clustering at the 0.01 significance level');
   elseif(stdMean < -1.65)
      display('Standard clustering at the 0.05 significance level');
   else
      display('Weak clustering at the 0.1 significance level');
   end
end
```

```
    %Plot standardized mean NN-distance for the current unit
    line(stdMean*[1 1], get(gca,'YLim'), 'color', 'red');

    if(k == 1)
        t = text(stdMean,0.3,'DU0');
    elseif(k == 2)
        t = text(stdMean,0.3,'DU1');
    elseif(k == 3)
        t = text(stdMean,0.3,'DU2');
    elseif(k == 4)
        t = text(stdMean,0.3,'DU3');
    elseif(k == 5)
        t = text(stdMean,0.3,'DU4');
    elseif(k == 6)
        t = text(stdMean,0.3,'DU5');
    elseif(k == 7)
        t = text(stdMean,0.3,'DU6');
    elseif(k == 8)
        t = text(stdMean,0.3,'All');
    end
    set(t, 'rotation', 90);
end

%Plot boundaries of significance
line(2.33*[1 1], get(gca,'YLim'), 'color', 'green');
line(-2.33*[1 1], get(gca,'YLim'), 'color', 'green');
t = text(2.33,0.1,'Strong dispersion');
set(t, 'rotation', 90);
t = text(-2.33,0.1,'Strong clustering');
set(t, 'rotation', 90);
title('Nearest Neighbor Method: One-tailed test');
```

K-function Method

To use the K-function on a new dataset, provide these input parameters in the 'generateSimulation.m' script file:

1. Load coordinates of channel-belt center-points in the 'inputPoints' array and include their depositional unit in the third column
2. Define the target depositional unit for the K-function calculation in the 'range' parameter
3. Define the maximum scale limit in the 'limit' parameter. This value should be constrained by the minimum outcrop dimension
4. Define the scale increment in the 'increment' parameter
5. Define the number of Monte Carlo simulation to generate
6. Run and debug

generateSimulations.m

```
%Filename: generateSimulations.m
%Author: Wassim Benhallam
%Version: 1.0
%Description: Calculates K-function for random Monte Carlo Simulations

%Provide coordinates of channel-belt center-points in the form [X Y DU]
inputPoints = [];   %[X Y DU]
range = 2; %use 'all', 0, 1, 2, 3, 4, 5, or 6 to define points range

%--------Find points and range for DU-----------
pointPattern = getPoints(range, inputPoints);
Ymin = min(pointPattern(:,2));
Ymax = max(pointPattern(:,2));
Xmin = min(inputPoints(:,1))
Xmax = max(inputPoints(:,1))
%--------Required parameters-----------
N=size(pointPattern, 1);
width = Xmax - Xmin
A=width*(Ymax - Ymin);
limit = 200;    %scale limit
increment = 5;  %scale increment
allResults = [];
MonteCarloSimulations = 99; %Number of simulations
mySum = 0;
%------------generateSimulations--------------------
for i=1:MonteCarloSimulations
   %generate random points within the study region
   points = rand(N,2);
   points(:,1) = Xmin + width.*points(:,1);
   points(:,2) = Ymin + (Ymax - Ymin).*points(:,2);
   simulationResults = [];
   for h=0:increment:limit; %Iterate here through different values of h.
      mySum = 0; Ko = 0; K = 0;
      for j=1:N
         for k=1:N
            if j~=k
               distance = sqrt((points(j,1) - points(k,1))^2 + (points(j,2) - points(k,2))^2); %Eucledean
distance between sj and sk
               if distance <= h
                  proportion = computeProportionOptimized(points(j,1), points(j,2), distance, Xmin,
Ymin, Xmax, Ymax);
                  mySum = mySum + (1/proportion);
               end
            end
         end
      end
      %Compute K with corresponding h, append to simulationResults
      Ko = mySum * (A/(N*N));
      K = sqrt(Ko/pi) - h;
      simulationResults = [simulationResults; K];
   end
   allResults = horzcat(allResults, simulationResults);
end
```

```
simulations = allResults;

%------------generatePattern----------------
pattern = computeKfunctionForPattern(N, A, limit, increment, pointPattern, Xmin, Ymin, Xmax,
Ymax);
%------------plotResults--------------------
plotResults(limit, increment, simulations, pattern);
```

getPoints.m

```
%Filename: getPoints.m
%Author: Wassim Benhallam
%Version: 1.0
%Description: Returns points of a specified depositional unit

function points = getPoints(range, allPoints)
   points = [];
   if(strcmp(range, 'all'))
      points = allPoints;
   else
      for i=1:size(allPoints, 1)
         if(allPoints(i, 3) == range)
            points = [points; allPoints(i, :)];
         end
      end
   end
end
```

computeProportionOptimized.m

```
%Filename: computeProportionOptimized.m
%Author: Wassim Benhallam
%Version: 1.0
%Description: Computes the edge effects correction

function proportion = computeProportionOptimized( centerX, centerY, t, Xmin, Ymin, Xmax, Ymax )
   angleOut = 0;
   d1 = Ymax - centerY;
   d2 = Xmax - centerX;
   d3 = centerY - Ymin;
   d4 = centerX - Xmin;

   a=0;
   b=0;
   c=0;
   d=0;

   if(t > d1)
      a = 1;
   end
   if(t > d2)
      b = 1;
   end
```

```
if(t > d3)
   c = 1;
end
if(t > d4)
   d = 1;
end

sum = a + b + c + d;

if(sum == 0)       %No intersection
   angleOut = 0;
elseif(sum == 1)   %Intersection with one side
   if(a == 1)
      angleOut = 2*acos(d1/t);
   elseif(b==1)
      angleOut = 2*acos(d2/t);
   elseif(c==1)
      angleOut = 2*acos(d3/t);
   elseif(d==1)
      angleOut = 2*acos(d4/t);
   end
elseif(sum == 2)   %Intersection with two sides
   %----------Intersection with two congruent sides----------
   if(a==1 && b==1)
      if(t^2 <= d1^2 + d2^2)
         angleOut = 2*acos(d1/t) + 2*acos(d2/t);
      else
         angleOut = pi/2 + acos(d1/t) + acos(d2/t);
      end
   elseif(b==1 && c==1)
      if(t^2 <= d2^2 + d3^2)
         angleOut = 2*acos(d2/t) + 2*acos(d3/t);
      else
         angleOut = pi/2 + acos(d2/t) + acos(d3/t);
      end
   elseif(c==1 && d==1)
      if(t^2 <= d3^2 + d4^2)
         angleOut = 2*acos(d3/t) + 2*acos(d4/t);
      else
         angleOut = pi/2 + acos(d3/t) + acos(d4/t);
      end
   elseif(d==1 && a==1)
      if(t^2 <= d4^2 + d1^2)
         angleOut = 2*acos(d4/t) + 2*acos(d1/t);
      else
         angleOut = pi/2 + acos(d4/t) + acos(d1/t);
      end
   %----------Intersection with two opposite sides----------
   elseif(a==1 && c==1)
      angleOut = 2*acos(d1/t) + 2*acos(d3/t);
   elseif(b==1 && d==1)
      angleOut = 2*acos(d2/t) + 2*acos(d4/t);
   end
elseif(sum == 3)   %Intersection with three sides
   if(a==1 && b==1 && c==1)
      if(t^2 <= d1^2 + d2^2 && t^2 <= d2^2 + d3^2)    %Two corners out
```

```
            angleOut = 2*acos(d1/t) + 2*acos(d2/t) + 2*acos(d3/t);
        elseif(t^2 <= d1^2 + d2^2 && t^2 > d2^2 + d3^2) %One corner out
            angleOut = pi/2 + 2*acos(d1/t) + acos(d2/t) + acos(d3/t);
        elseif(t^2 > d1^2 + d2^2 && t^2 <= d2^2 + d3^2) %One corner out
            angleOut = pi/2 + acos(d1/t) + acos(d2/t) + 2*acos(d3/t);
        elseif(t^2 > d1^2 + d2^2 && t^2 > d2^2 + d3^2)  %Two corners in
            angleOut = pi + acos(d1/t) + acos(d3/t);
        end
    elseif(a==1 && b==1 && d==1)
        if(t^2 <= d1^2 + d2^2 && t^2 <= d1^2 + d4^2)
            angleOut = 2*acos(d1/t) + 2*acos(d2/t) + 2*acos(d4/t);
        elseif(t^2 <= d1^2 + d2^2 && t^2 > d1^2 + d4^2)
            angleOut = pi/2 + 2*acos(d2/t) + acos(d1/t) + acos(d4/t);
        elseif(t^2 > d1^2 + d2^2 && t^2 <= d1^2 + d4^2)
            angleOut = pi/2 + acos(d1/t) + acos(d2/t) + 2*acos(d4/t);
        elseif(t^2 > d1^2 + d2^2 && t^2 > d1^2 + d4^2)
            angleOut = pi + acos(d4/t) + acos(d2/t);
        end
    elseif(a==1 && c==1 && d==1)
        if(t^2 <= d1^2 + d4^2 && t^2 <= d3^2 + d4^2)
            angleOut = 2*acos(d1/t) + 2*acos(d3/t) + 2*acos(d4/t);
        elseif(t^2 <= d1^2 + d4^2 && t^2 > d3^2 + d4^2)
            angleOut = pi/2 + 2*acos(d1/t) + acos(d3/t) + acos(d4/t);
        elseif(t^2 > d1^2 + d4^2 && t^2 <= d3^2 + d4^2)
            angleOut = pi/2 + acos(d1/t) + acos(d4/t) + 2*acos(d3/t);
        elseif(t^2 > d1^2 + d4^2 && t^2 > d3^2 + d4^2)
            angleOut = pi + acos(d1/t) + acos(d3/t);
        end
    elseif(b==1 && c==1 && d==1)
        if(t^2 <= d2^2 + d3^2 && t^2 <= d3^2 + d4^2)
            angleOut = 2*acos(d2/t) + 2*acos(d3/t) + 2*acos(d4/t);
        elseif(t^2 <= d2^2 + d3^2 && t^2 > d3^2 + d4^2)
            angleOut = pi/2 + 2*acos(d2/t) + acos(d3/t) + acos(d4/t);
        elseif(t^2 > d2^2 + d3^2 && t^2 <= d3^2 + d4^2)
            angleOut = pi/2 + acos(d2/t) + acos(d3/t) + 2*acos(d4/t);
        elseif(t^2 > d2^2 + d3^2 && t^2 > d3^2 + d4^2)
            angleOut = pi + acos(d2/t) + acos(d3/t);
        end
    end
end

    proportion = (2*pi - angleOut)/(2*pi);
end
```

computeKfunctionForPattern.m

```
%Filename: computeKfunctionForPattern.m
%Author: Wassim Benhallam
%Version: 1.0
%Description: Returns K-function values calculated for a given point pattern

function results = computeKfunctionForPattern(N, A, limit, increment, pointPattern, Xmin, Ymin,
Xmax, Ymax)
    mySum = 0;
```

```
    results = [];
    %-------------K-function--------------
    for h=0:increment:limit; %iterate here through different values of h.
        mySum = 0; K = 0;
        for j=1:N
            for k=1:N
                if j~=k
                    distance = sqrt((pointPattern(j,1) - pointPattern(k,1))^2 + (pointPattern(j,2) -
pointPattern(k,2))^2);%Eucledean distance sj and sk
                    if distance <= h
                        proportion = computeProportionOptimized(pointPattern(j,1), pointPattern(j,2), distance,
Xmin, Ymin, Xmax, Ymax);
                        mySum = mySum + (1/proportion);
                    end
                end
            end
        end
        mySum
        Ko = mySum * (A/(N*N));
        K = sqrt(Ko/pi) - h;
        results = [results; K];
    end
end
```

plotResults.m

```
%Filename: plotResults.m
%Author: Wassim Benhallam
%Version: 1.0
%Description: Plots K-function values for the random Monter Carlo enveloppe and for the point
pattern

function plotResults(limit, increment, simulations, pattern)
    maxs = [];
    mins = [];
    h = [];
    for i=0:increment:limit
        h = [h ; i];
    end
    for i=1:size(simulations, 1)
        maxs = [maxs; max(simulations(i,:))];
        mins = [mins; min(simulations(i,:))];
    end
    hold on;
    %patch([h fliplr(h)], [maxs,fliplr(mins)],'g');% area(h, maxs);
    plot(h, maxs, 'Color', 'black');
    plot(h, mins, 'Color', 'black');
    plot(h, pattern, 'Color', [59/255, 113/255, 86/255], 'LineWidth', 2);
    box on;
    hold off;
end
```

Quadrat-based Moving Window Analysis

To apply the quadrat-based moving window analysis on a new dataset, provide these input parameters in the 'MovingWindow.m' script file:

1. Load coordinates of channel-belt center-points in the 'inputPoints' array
2. Define the base and top Y coordinates of the moving window
3. Define the moving window increment step
4. Define the width and height of a grid cell
5. Define the moving average range
6. Run and debug

MovingWindow.m

```
%Filename: MovingWindow.m
%Author: Wassim Benhallam
%Version: 1.0
%Description: Performs a moving window analysis based on the quadrat method

%Provide coordinates of channel-belt centerpoints here
inputPoints = [];

%---------------Setup required parameters--------------%
base = min(inputPoints(:,2));       %Starting position of window base
top = max(inputPoints(:,2)) - 15;   %Final position of window base
increment = 1;                      %Increment of window base
cw = 100;                           %Cell width in window
ch = 35;                            %Cell height in window
ratios = [];                        %Holds final ratios
aveSize = 8;                        %Define moving average range

%-----------Loop through all window positions-----------%
for k=base:increment:top
   cells = Cell();

   %--------Calculate Min X within current window------%
   min = 10000;
   for c=1:length(inputPoints)
      if(inputPoints(c,2) < k+(2*ch) && inputPoints(c,2) >= k)
         if(inputPoints(c,1) < min)
            min = inputPoints(c,1);
         end
      end
   end

   %--------Calculate Max X within current window------%
   max = 0;
   for c=1:length(inputPoints)
```

```
        if(inputPoints(c,2) < k+(2*ch) && inputPoints(c,2) >= k)
            if(inputPoints(c,1) > max)
                max = inputPoints(c,1);
            end
        end
    end

    %--------Fill current window with cells------%
    min = floor(min/100);
    max = floor(max/100);
    walker = 1;
    for i=min:max
        cells(walker) = Cell(i*cw, k, cw, ch);
        cells(walker + 1) = Cell(i*cw, k+ch, cw, ch);
        walker = walker + 2;
    end

    %--------Count points within each cell of current window------%
    for i=1:length(inputPoints)
        x = floor(inputPoints(i,1)/100)*100;
        column = ((x/100 + 1) - min)*2 ;
        if(inputPoints(i,2) < k+ch & inputPoints(i,2) >= k)
            index = column-1;
            cells(index) = cells(index).incrementCount();
        elseif(inputPoints(i,2) < k+(2*ch) & inputPoints(i,2) >= k+ch)
            index = column;
            cells(index) = cells(index).incrementCount();
        end
    end

    %--------Count total number of points within current window------%
    counts = {cells.count};
    pointsIn = 0;
    for i=1:length(counts)
        pointsIn = pointsIn + counts{i};
    end

    %--------Calculate Mean and variance of current window------%
    mean = pointsIn/length(cells);
    sum = 0;
    for i=1:length(cells)
        sum = sum + (cells(i).count - mean)^2;
    end
    variance = sum/(length(cells) - 1);
    ratio = variance/mean;
    row = [ratio k];
    ratios = vertcat(ratios, row);

    %--------Plot cell positions within current grid------%
    scatter(inputPoints(:,1), inputPoints(:,2));
    for i=1:length(cells)
        rectangle('Position', [cells(i).x, cells(i).y, cells(i).width, cells(i).height]);
    end
end

%--------Plot ratios for each window position------%
```

```
figure;
scatter(ratios(:,1), ratios(:,2),'rx');
length(ratios);

%--------Calculate a moving average for ratios------%
movingAverage = [];
for i=aveSize+1:aveSize:length(ratios)
    average = 0;
    height = 0;
    for j=i-aveSize:i-1
        average = ratios(j,1) + average;
        height = ratios(j,2) + height;
    end
    average = average/aveSize;
    height = height/aveSize;
    newRow = [average height];
    movingAverage = vertcat(movingAverage, newRow);
end

%--------Plot Moving average curve------%
hold on;
plot(movingAverage(:,1), movingAverage(:,2));
xlabel('Clustering Index');
ylabel('Elevation in meters');
```

Cell.m

```
%Filename: Cell.m
%Author: Wassim Benhallam
%Version: 1.0
%Description: Defines grid cell information

classdef Cell
    properties
        x;
        y;
        width;
        height;
        count = 0;
    end

    methods
        %constructor
        function obj = Cell(x,y,width,height)
            if nargin ~= 0
                obj.x = x;
                obj.y = y;
                obj.width = width;
                obj.height = height;

            end
        end

        function c = getCount(obj)
```

```
        c = obj.count;
    end

    function obj = incrementCount(obj)
        obj.count = obj.count + 1;
    end
    function obj = resetCount(obj)
        obj.count = 0;
    end

    function inside = isPointInside(obj,x,y)
        if(x >= obj.x && x <= obj.x + obj.width && y >= obj.y && y <= obj.y + obj.height)
            inside = true;
        else
            inside = false;
        end
    end

  end
end
```

K-function-based Moving Window Analysis

To apply the K-function-based moving window analysis on a new dataset, provide these input parameters in the 'MovingWindow.m' script file:

1. Load coordinates of channel-belt center-points in the 'points' array
2. Define the base and top Y coordinates of the moving window base
3. Define the moving window increment step
4. Define the moving window height
5. Define the scale increment
6. Define the number of Monte Carlo simulations
7. Run and debug

MovingWindow.m

```
%Filename: MovingWindow.m
%Author: Wassim Benhallam
%Version: 1.0
%Description: Performs a moving window analysis based on the K-function method

points = [];
base = min(points(:,2));           %Starting position of window base
movingWindowIncrement = 1;         %Moving window increment
wh = 150;                          %Moving window height
offset = wh;                       %Offset of final position of window from max Y.
top = max(points(:,2)) - offset    %Final position of window base
windows = Window();                %Array of all windows
walker = 1;                        %Window index
scaleIncrement = 1;                %Scale increment
numberOfSimulations = 99;          %Number of Monte Carlo simulations
windowSimulations = [];
allWindowSimulations = [];
pointsInWindow = [];

for k=base:movingWindowIncrement:top
   fprintf('Moving window is currently at y:%i\n',k);
   %Find Xmin, Xmax, and count
   Xmin = 2000;
   Xmax = 0;
   count = 0;
   pointsInWindow = [];

   %Calculate minimum and maximum X coordinates of current window
   for c=1:length(points)
      if(points(c,2) < k+wh && points(c,2) >= k)
         pointsInWindow = [pointsInWindow; points(c,:)];
         count = count+1;
         if(points(c,1) < Xmin)
            Xmin = points(c,1);
         end
         if(points(c,1) > Xmax)
            Xmax = points(c,1);
         end
      end
   end

   %----------------K-function----------------
   %Generate 99 random MonteCarlo simulations for the current window
   windowSimulations = generateSimulations( Xmin, k, Xmax, k+wh, count , numberOfSimulations,
scaleIncrement);

   %Compute K-function for point pattern within current window
   Kvalues = computeKfunctionForPattern( Xmin, k, Xmax, k+wh, count , pointsInWindow,
scaleIncrement);

   %---------Creating a window structure-------
   windows(walker) = Window(Xmin, k, Xmax, k+wh, count, windowSimulations, Kvalues);
   walker = walker + 1;
```

```
end

%----------Plotting the window-----------
scatter(points(:,1), points(:,2));
for i=1:length(windows)
    rectangle('Position', [windows(i).Xmin, windows(i).Ymin, windows(i).Xmax - windows(i).Xmin,
windows(i).Ymax - windows(i).Ymin]);
end

figure;
%----------Plot 3D K-function values and 3D P-values----------
allPs = plotDataIn3D(windows, wh, scaleIncrement, movingWindowIncrement, base, top);

%----------Optional/Extra----------
%----------Plot 2D K-function window and 2D P-values at a given scale----------
movingKsAndPs = plotKMovingWindow(windows, allPs, wh);
%----------Calculate moving average of 2D K-function and 2D P-value plots----------
movingAverage = calculateMovingAverage(movingKsAndPs, 8);
```

Window.m

```
%Filename: Window.m
%Author: Wassim Benhallam
%Version: 1.0
%Description: Defines parameters of a window

classdef Window
    properties
        Xmin;
        Ymin;
        Xmax;
        Ymax;
        count = 0;
        simulations = [];
        Kvalues = [];
    end

    methods
        %constructor
        function obj = Window(Xmin,Ymin,Xmax,Ymax, count, simulations, Kvalues)
            if nargin ~= 0
                obj.Xmin = Xmin;
                obj.Ymin = Ymin;
                obj.Xmax = Xmax;
                obj.Ymax = Ymax;
                obj.count = count;
                obj.simulations = simulations;
                obj.Kvalues = Kvalues;
            end
        end

        function c = getCount(obj)
            c = obj.count;
        end
```

```
    function obj = set.count(obj, value)
        obj.count = value;
    end

    function count = get.count(obj)
        count = obj.count;
    end

    function obj = incrementCount(obj)
        obj.count = obj.count + 1;
    end

  end
end
```

generateSimulations.m

```
%Filename: generateSimulations.m
%Author: Wassim Benhallam
%Version: 1.0
%Description: Calculates K-function values for random Monte Carlo simulations

%N: number of points, n: number of monter carlo simulations
function allResults = generateSimulations( Xmin, Ymin, Xmax, Ymax, N , n, scaleIncrement)
    A=(Xmax - Xmin) * (Ymax - Ymin);    %Area of window
    limit = Ymax - Ymin;                %Upper limit of h
    allResults = [];                    %Stores all simulations
    mySum = 0;

    for i=1:n
        points = rand(N,2);
        points(:,1) = Xmin +(Xmax - Xmin).*points(:,1);
        points(:,2) = Ymin + (Ymax - Ymin).*points(:,2);
        simulationResults = [];
        for h=0:scaleIncrement:limit; %Iterate through different scales
            mySum = 0;
            Ko = 0;
            K = 0;
            for j=1:N
                for k=1:N
                    if j~=k
                        distance = sqrt((points(j,1) - points(k,1))^2 + (points(j,2) - points(k,2))^2); %Eucledean
distance between sj and sk
                        if distance <= h
                            %Get the proportion W(sj, sk)
                            proportion = computeProportionOptimized(points(j,1), points(j,2), distance, Xmin,
Ymin, Xmax, Ymax);
                            mySum = mySum + (1/proportion);
                        end
                    end
                end
            end
            Ko = mySum * (A/(N*N));
```

```
        K = sqrt(Ko/pi) - h;
        simulationResults = [simulationResults; K];
    end
    allResults = horzcat(allResults, simulationResults);
  end
end
```

computeProportionOptimized.m

```
%Filename: computeProportionOptimized.m
%Author: Wassim Benhallam
%Version: 1.0
%Description: Calculates edge effects correction

function proportion = computeProportion2( centerX, centerY, t, Xmin, Ymin, Xmax, Ymax )
  angleOut = 0;
  d1 = Ymax - centerY;
  d2 = Xmax - centerX;
  d3 = centerY - Ymin;
  d4 = centerX - Xmin;
  a=0;
  b=0;
  c=0;
  d=0;
  if(t > d1)
    a = 1;
  end
  if(t > d2)
    b = 1;
  end
  if(t > d3)
    c = 1;
  end
  if(t > d4)
    d = 1;
  end
  sum = a + b + c + d;

  if(sum == 0)       %No intersection
    angleOut = 0;
  elseif(sum == 1)   %Intersection with one side
    if(a == 1)
      angleOut = 2*acos(d1/t);
    elseif(b==1)
      angleOut = 2*acos(d2/t);
    elseif(c==1)
      angleOut = 2*acos(d3/t);
    elseif(d==1)
      angleOut = 2*acos(d4/t);
    end
  elseif(sum == 2)   %Intersection with two sides
    %----------Intersection with two congruent sides----------
    if(a==1 && b==1)
      if(t^2 <= d1^2 + d2^2)
```

```
            angleOut = 2*acos(d1/t) + 2*acos(d2/t);
        else
            angleOut = pi/2 + acos(d1/t) + acos(d2/t);
        end
    elseif(b==1 && c==1)
        if(t^2 <= d2^2 + d3^2)
            angleOut = 2*acos(d2/t) + 2*acos(d3/t);
        else
            angleOut = pi/2 + acos(d2/t) + acos(d3/t);
        end
    elseif(c==1 && d==1)
        if(t^2 <= d3^2 + d4^2)
            angleOut = 2*acos(d3/t) + 2*acos(d4/t);
        else
            angleOut = pi/2 + acos(d3/t) + acos(d4/t);
        end
    elseif(d==1 && a==1)
        if(t^2 <= d4^2 + d1^2)
            angleOut = 2*acos(d4/t) + 2*acos(d1/t);
        else
            angleOut = pi/2 + acos(d4/t) + acos(d1/t);
        end
    %----------Intersection with two opposite sides----------
    elseif(a==1 && c==1)
        angleOut = 2*acos(d1/t) + 2*acos(d3/t);
    elseif(b==1 && d==1)
        angleOut = 2*acos(d2/t) + 2*acos(d4/t);
    end
elseif(sum == 3)    %Intersection with three sides
    if(a==1 && b==1 && c==1)
        if(t^2 <= d1^2 + d2^2 && t^2 <= d2^2 + d3^2)     %Two corners out
            angleOut = 2*acos(d1/t) + 2*acos(d2/t) + 2*acos(d3/t);
        elseif(t^2 <= d1^2 + d2^2 && t^2 > d2^2 + d3^2)  %One corner out
            angleOut = pi/2 + 2*acos(d1/t) + acos(d2/t) + acos(d3/t);
        elseif(t^2 > d1^2 + d2^2 && t^2 <= d2^2 + d3^2)  %One corners out
            angleOut = pi/2 + acos(d1/t) + acos(d2/t) + 2*acos(d3/t);
        elseif(t^2 > d1^2 + d2^2 && t^2 > d2^2 + d3^2)   %Two corners ins
            angleOut = pi + acos(d1/t) + acos(d3/t);
        end
    elseif(a==1 && b==1 && d==1)
        if(t^2 <= d1^2 + d2^2 && t^2 <= d1^2 + d4^2)
            angleOut = 2*acos(d1/t) + 2*acos(d2/t) + 2*acos(d4/t);
        elseif(t^2 <= d1^2 + d2^2 && t^2 > d1^2 + d4^2)
            angleOut = pi/2 + 2*acos(d2/t) + acos(d1/t) + acos(d4/t);
        elseif(t^2 > d1^2 + d2^2 && t^2 <= d1^2 + d4^2)
            angleOut = pi/2 + acos(d1/t) + acos(d2/t) + 2*acos(d4/t);
        elseif(t^2 > d1^2 + d2^2 && t^2 > d1^2 + d4^2)
            angleOut = pi + acos(d4/t) + acos(d2/t);
        end
    elseif(a==1 && c==1 && d==1)
        if(t^2 <= d1^2 + d4^2 && t^2 <= d3^2 + d4^2)
            angleOut = 2*acos(d1/t) + 2*acos(d3/t) + 2*acos(d4/t);
        elseif(t^2 <= d1^2 + d4^2 && t^2 > d3^2 + d4^2)
            angleOut = pi/2 + 2*acos(d1/t) + acos(d3/t) + acos(d4/t);
        elseif(t^2 > d1^2 + d4^2 && t^2 <= d3^2 + d4^2)
            angleOut = pi/2 + acos(d1/t) + acos(d4/t) + 2*acos(d3/t);
```

```
        elseif(t^2 > d1^2 + d4^2 && t^2 > d3^2 + d4^2)
            angleOut = pi + acos(d1/t) + acos(d3/t);
        end
    elseif(b==1 && c==1 && d==1)
        if(t^2 <= d2^2 + d3^2 && t^2 <= d3^2 + d4^2)
            angleOut = 2*acos(d2/t) + 2*acos(d3/t) + 2*acos(d4/t);
        elseif(t^2 <= d2^2 + d3^2 && t^2 > d3^2 + d4^2)
            angleOut = pi/2 + 2*acos(d2/t) + acos(d3/t) + acos(d4/t);
        elseif(t^2 > d2^2 + d3^2 && t^2 <= d3^2 + d4^2)
            angleOut = pi/2 + acos(d2/t) + acos(d3/t) + 2*acos(d4/t);
        elseif(t^2 > d2^2 + d3^2 && t^2 > d3^2 + d4^2)
            angleOut = pi + acos(d2/t) + acos(d3/t);
        end
    end
  end
  proportion = (2*pi - angleOut)/(2*pi);
end
```

computeKfunctionForPattern.m

```
%Filename: computeKfunctionForPattern.m
%Author: Wassim Benhallam
%Version: 1.0
%Description: Calculates K-function values for a given point pattern

function Ks = computeKfunctionForPattern( Xmin, Ymin, Xmax, Ymax, N , points, scaleIncrement)
   A=(Xmax - Xmin) * (Ymax - Ymin);    %Area of window
   limit = Ymax - Ymin;              %Upper limit of h
   mySum = 0;
   Ks = [];
   for h=0:scaleIncrement:limit; %Iterate through different scales
      mySum = 0;
      Ko = 0;
      K = 0;
      for j=1:N
         for k=1:N
            if j~=k
               distance = sqrt((points(j,1) - points(k,1))^2 + (points(j,2) - points(k,2))^2); %Eucledean
distance between sj and sk
               if distance <= h
                  %Get the proportion W(sj, sk)
                  proportion = computeProportionOptimized(points(j,1), points(j,2), distance, Xmin,
Ymin, Xmax, Ymax);
                  mySum = mySum + (1/proportion);
               end
            end
         end
      end
      Ko = mySum * (A/(N*N));
      K = sqrt(Ko/pi) - h;
      Ks = [Ks; K];
   end
end
```

plotDataIn3D.m

```
%Filename: plotDataIn3D.m
%Author: Wassim Benhallam
%Version: 1.0
%Description: Plots the 3D K-function values and P-values. (Axes are window position, scale, and K-function value/P-value)

function allPs = plotDataIn3D(windows, scaleLimit, scaleIncrement, movingWindowIncrement, base, top)
    n = size(windows,2); %number of windows
    allMaxKs = [];      %all maxKs vectors
    allMinKs = [];
    allKs = [];
    allPs = [];
    for i=1:n
        maxKs = [];
        minKs = [];
        Ps = [];
        currentWindow = windows(i);
        simulations = currentWindow.simulations;
        for j=1:size(simulations,1)  %1 to max scale
            maxKs = [maxKs max(simulations(j,:))];
            minKs = [minKs min(simulations(j,:))];
            p = computePvalue(currentWindow.Kvalues(j), simulations(j,:));
            Ps = [Ps p];
        end
        allMaxKs = [allMaxKs; maxKs];
        allMinKs = [allMinKs; minKs];
        allKs = [allKs; currentWindow.Kvalues'];
        allPs = [allPs; Ps];
    end

    x = 0:scaleIncrement:scaleLimit;
    y = base:movingWindowIncrement:top;

    %Get X and Y matrices
    [X Y] = meshgrid(x, y);

    %--------------Method 1: Plot original matrices----------
    % hold on;
    % surf(X,Y,allMaxKs);
    % surf(X,Y,allMinKs);
    % surf(X,Y,allKs, 'FaceColor',[1 1 1]);

    %--------------Method 2: Plot interpolated matrices----------
    % % %get x, y, and z vectors
    x = reshape(X, size(X,1)*size(X,2), 1);
    y = reshape(Y, size(Y,1)*size(Y,2), 1);
    zmax = reshape(allMaxKs, size(allMaxKs,1)*size(allMaxKs,2), 1);
    zmin = reshape(allMinKs, size(allMinKs,1)*size(allMinKs,2), 1);
    z = reshape(allKs, size(allKs,1)*size(allKs,2), 1);
    p = reshape(allPs, size(allPs,1)*size(allPs,2), 1);
    %
    stepsX = linspace(0, scaleLimit, scaleLimit);   %set number of values to 50 to match original matrix
```

```
    stepsY = linspace(base,top, top - base);        %set number of values to 200 to match original matrix
    [XNew,YNew] = meshgrid(stepsX, stepsY);
    Zmax = griddata(x, y, zmax, XNew, YNew);
    Zmin = griddata(x, y, zmin, XNew, YNew);
    Z = griddata(x, y, z, XNew, YNew);
    P = griddata(x, y, p, XNew, YNew);
    hold on;
    surf(XNew, YNew, Zmax, 'FaceColor', [1 0 0]);
    surf(XNew, YNew, Zmin, 'FaceColor', [0 0 1]);
    surf(XNew, YNew, Z, 'FaceColor',[1 1 1]);
    set(gca,'color','none');
    xlabel('Scale of clustering/uniformity');
    ylabel('Elevation of moving window(m)');
    zlabel('K-function value');
    % title('K-function based moving window analysis');

    figure;
    surf(XNew, YNew, P);
    xlabel('Scale of clustering/uniformity');
    ylabel('Elevation of moving window(m)');
    zlabel('P-value');
    set(gcf, 'renderer', 'zbuffer');
    colorbar;
end
```

computePvalue.m

```
%Filename: computePvalue.m
%Author: Wassim Benhallam
%Version: 1.0
%Description: Calculates P-value at a given scale

function p = computePvalue(Kvalue, simulations)
    m = 0; %Number of simulations with a K-function value at least as high as that of the pattern.
    for i=1:size(simulations,2)
        if(simulations(i) >= Kvalue)
            m = m + 1;
        end
    end
    p = (m+1)/(size(simulations,2)+1);
end
```

plotKMovingWindow.m

```
%Filename: plotKMovingWindow.m
%Author: Wassim Benhallam
%Version: 1.0
%Description: Plots Kfunction values and P-value for a given scale

function movingKsAndPs = plotKMovingWindow(windows, allPs, scale);
    scale = scale + 1;
    allKs = {windows.Kvalues};
    movingKsAndPs = [];
```

```
    xAxis = 1:1:length(allKs)
    newXAxis = max(xAxis) - xAxis;
    for i=1:length(allKs)
        movingKsAndPs = [movingKsAndPs; allKs{i}(scale)];
    end

    movingKsAndPs = [movingKsAndPs allPs(:,scale) newXAxis'];

    figure;
    plot(movingKsAndPs(:,1), movingKsAndPs(:,3),'blue');
    title('K-function based moving window');
    xlabel('K-function');
    ylabel('Moving Window Position');
    set(gca,'YDir','reverse');
    figure;

    plot(movingKsAndPs(:,2), movingKsAndPs(:,3), 'red');
    title('P-values');
    xlabel('P-values');
    ylabel('Moving Window Position');
    set(gca,'YDir','reverse');
end
```

calculateMovingAverage.m

```
%Filename: calculateMovingAverage.m
%Author: Wassim Benhallam
%Version: 1.0
%Description: Calculates a moving average of K-function values and P-values

function movingAverage = calculateMovingAverage(movingKsAndPs, aveSize);
    movingAverage = [];
    for i=aveSize+1:aveSize:length(movingKsAndPs)
        averageK = 0;
        averageP = 0;
        height = 0;
        for j=i-aveSize:i-1
            averageK = movingKsAndPs(j,1) + averageK;
            averageP = movingKsAndPs(j,2) + averageP;
            height = movingKsAndPs(j,3) + height;
        end
        averageK = averageK/aveSize;
        averageP = averageP/aveSize;
        height = height/aveSize;
        newRow = [averageK averageP height];
        movingAverage = vertcat(movingAverage, newRow);
    end
```

APPENDIX D

LiDAR VISUALIZATION PLUGIN

Terrestrial laser ranging (LiDAR) is an extremely accurate and efficient remote sensing technology with tremendous application potential in outcrop stratigraphic modelling. Laser range data, combined with remotely sampled imagery, enables researchers to produce high-accuracy 3D digital outcrop models (DOM) that can be used to conduct high precision facies characterization, map key surfaces (i.e., fault planes, unconformities), and make various geologic interpretations. However, existing LiDAR acquisition and processing software is not designed for geologic applications and is therefore not suited for outcrop interpretation and modeling. Similarly, conventional geologic software with modeling capabilities (such as Petrel) does not allow the integration of LiDAR data into its workflows. Therefore, a plugin is developed for Schlumberger's Petrel E&P software platform that allows the integration of LiDAR technology into various Petrel workflows. In addition to raw LiDAR point cloud visualization, the plugin also enables the visualization of textured TIN meshes (triangulated irregular networks) that are built in third-party LiDAR processing software.

Applications

These textured surfaces can be used in Petrel to build digital outcrop models that serve both as analogs and quantitative inputs into reservoir models. Other benefits to the

use of DOMs include the ability to digitally inspect stratigraphic units, generate more realistic and predictive flow simulation geocellular models, and use these models to project geology across canyons. Ultimately, the addition of LiDAR technology to Petrel's toolbox through this plugin bridges the existing gap between oil and gas exploration-to-production software (such as Petrel) and industry-independent LiDAR acquisition and processing software vendors.

Installation Instructions

To install the LiDAR plugin, the following software is needed:

- Windows 7 operating system or later
- Petrel 2013 with valid license
- Visual Studio 2010 with .NET 4.0
- Ocean for Petrel 2013

Once the required software is downloaded, install in the following order

1. Download and install Petrel 2013
2. Download and install Visual Studio 2010 (VS 2010)
3. Download and install Ocean for Petrel 2013

Note that Ocean for Petrel 2013 only works with Visual Studio 2010. Do not install Visual Studio 2012 or later versions. Also, Petrel 2013 and Visual Studio 2010 should be installed prior to installing Ocean for Petrel 2013.

Building the Visual Studio Project

Follow the instructions below to build and install the LiDAR plugin in Petrel 2013. Note that the Visual Studio project for the LiDAR plugin and demo files are available in

the "LiDAR Visualization Plugin" folder under the Rocks2Models group's shared drive.

1. Copy the project folder inside "VS2010 - Lidar Project" to your local project folder in "Documents/VS Studio 2010/Projects"
2. Start Visual Studio 2010 and open the project
3. In the "Solution Explorer," right click on "Solution 'LidarPlugin'" and select "Build Solution"
4. You will likely get "missing reference path" errors or warnings. To fix these:
    a. Open the "Reference" folder under "LidarPluginProject" in the solution explorer
    b. Note and remove all missing references. Missing references are shown with a yellow exclamation mark next to their icons
    c. Right-click the "References" folder under "LidarPLuginProject" in the solution explorer, and select "Add Reference"
    d. In the new dialog, select the "Browse" tab and browse to the "Petrel 2013/Public" folder under your "Schlumberger" installation folder in "Program Files"
    e. Select all the references that were previously marked as missing (by Ctrl clicking)
    f. Click Ok and build the solution again

Start Petrel 2013, the "Lidar" menu item is now displayed as part of the top menu tool bar. Note that the above workflow is only performed once. The next time Petrel is started, the plugin will still be available.

Plugin Demo

To import a Triangulated Irregular Network (TIN), or a textured mesh surface in simple terms, follow these steps:

1. Click on the "Lidar" menu item in Petrel and select "Import Mesh Surface"
2. In the "Import file" dialog, make sure "SurfaceMeshASCII(*.iv)" is selected in the file type combo box
3. Browse to the "Demo Files" folder and select one of the two provided ".iv" demo files
4. Click open. This step will take 1 to 2 minutes (more time for larger files)
5. Create a 3D window in Petrel from the "Window" menu and check the imported file in the input tab. After a couple of seconds, you should see the surface in the 3D window
6. Make sure the vertical exaggeration is set to "1" so that the surface is not distorted
7. Start making interpretations

LiDAR Point Cloud To Textured Surface

Although you can import a point cloud to Petrel using this LiDAR plugin, it is always preferable to directly import a textured surface mesh that is reconstructed from the original LiDAR point cloud. This reconstruction process can be tedious and time-consuming in the absence of a simple to use workflow and the appropriate processing software. To create these surfaces, I recommend using "MeshLab," an open source and free 3D mesh processing software. Download and install the software, then follow these instructions:

1. Open Meshlab, click File > Import Mesh and select a small test point cloud. Point

clouds can be imported in many formats including ".ply" and ".pts". If you do not have a point cloud yet, you can use the provided ".ply" demo point cloud.

2. Next, proceed to clean the decimated mesh by removing unwanted/outlier points. To do that, highlight the unwanted vertices using the select tool, then click the "delete vertices" button from the top menu tool bar.
3. Use Poisson-disk sampling to decimate the point cloud (typically to less than 1M points). To do that, select Filters > Sampling > Poisson-Disk Sampling. In the new dialog, type in the new point spacing in the first "Explicit Radius" field in meters. Try using a 0.2 (i.e., 20 cm) as a point spacing.
4. Check the "Base Mesh Subsampling" option then click the "Apply" button.
5. In the layer dialog, highlight the new mesh file and check the new vertex count in the bottom of the main window. If the vertex count is still large, repeat from step 3 with a new larger spacing parameter.
6. To reconstruct the mesh surface, the normal vector to every vertex in the cloud needs to be calculated. To do that, select Filters > Point Set > Compute normal for point sets. Use 10 neighbors. This process will usually take about 3mins for a cloud of 1 million points. You can display the resulting normals by going to Render > Show Vertex Normals.
7. Transfer the vertex normals to the original nondecimated mesh by clicking Filters > Sampling > Vertex Attribute Transfer. In the new dialog, select the decimated mesh as a source mesh and the original nondecimated mesh as a target mesh. Uncheck "Transfer Color" and check the "Transfer Normal" option, then hit "Apply." The original mesh now has normal vectors.

8. Highlight the original mesh, then select Filters > Point Set > Surface Reconstruction: Poisson. Use 12 for "Octree Depth" and 7 for "Solver Divide," and then hit Apply. This process will also take about 3mins for a 1M large point cloud. Once the surface is created, select the "Wireframe" display option to display the polygons and edges.
9. Clean the surface and remove erroneous polygons by highlighting them using the "Select Faces in a rectangular region" button in the top tool bar, then clicking the "delete the current set of selected faces and all the vertices surrounded by that faces" button. If the resulting surface is too large/heavy to handle, decimate it using either Poisson-Disk sampling or "Quadratic Edge Collapse Decimation" under Filters > Remeshing Simplification and Reconstruction.
10. Once the surface is cleaned, proceed to transfer colors from the original point cloud to the reconstructed surface. To do that, select Filters > Sampling > Vertex Attribute Transfer. Select the original point cloud as a source mesh and the reconstructed surface as a target mesh, check "Transfer Color" as the only option, then hit Apply. The reconstructed surface is now textured using RGB colors of the original point cloud.
11. Finally, export the reconstructed surface using File > "Export Mesh as," and make sure to select "VRML File Format" as a file type.
12. Rename the extension of the output file form ".wrl" to ".iv." The new reconstructed surface with the ".iv" extension is now ready to be imported to Petrel using the LiDAR plugin as illustrated in the previous section.

REFERENCES

Allen, J.R.L., 1978, Studies in fluviatile sedimentation: an exploratory quantitative model for the architecture of avulsion-controlled alluvial suites: Sedimentary Geology, v. 21, p. 129–147.

Allen, J.R.L., 1979, Studies in fluviatile sedimentation: an elementary geometrical model for the connectedness of avulsion-related channel sandstone bodies: Sedimentary Geology, v. 24, p. 253–267.

Allen, J. L., and Johnson, C. L., 2010, Facies control on sandstone composition (and influence of statistical methods on interpretations) in the John Henry Member, Straight Cliffs Formation, Southern Utah, USA: Sedimentary Geology, v. 230, no. 1, p. 60-76.

Allen, J.L., and Johnson, C. L., 2011, Architecture and formation of transgressive-regressive cycles in marginal marine strata of the John Henry Member, Straight Cliffs Formation, Upper Cretaceous of southern Utah, USA: Sedimentology, v. 58, p. 1486-1513.

Armstrong, R. L., 1968, Sevier orogenic belt in Nevada and Utah: Geological Society of America Bulletin, v. 79, no. 4, p. 429-458.

Aslan, A. and Blum, M.D., 1999, Contrasting styles of Holocene avulsion, Texas Gulf Coastal Plain, U.S.A, in: N.D. Smith and J. Rogers, eds., Fluvial Sedimentology VI: Spec. Publ. Int. Assoc. Sedimentol., v. 28, p. 293–308.

Bailey, T.C. and Gatrell, A.C., 1995, Interactive Spatial Data Analysis, Addison Wesley Longman Limited: Essex, England.

Bridge, J.S. and Leeder, M.R., 1979, A simulation model of alluvial stratigraphy: Sedimentology, v. 26, p. 617–644.

Bryant, M., Falk, P. and Paola, C., 1995, Experimental study of avulsion frequency and rate of deposition: Geology, v. 23, p. 365–368.

Chatanantavet, P., Lamb, M. P., and Nittrouer, J. A., 2012, Backwater controls of avulsion location on deltas: Geophysical Research Letters, v. 39, no. 1.

Chentnik, B., Johnson, C.L., Mulhern, J., Stright, L., in press, Valleys, estuaries, and

lagoons: Paleoenvironments and regressive-transgressive architecture of the Upper Cretaceous Straight Cliffs Formation, accepted pending moderate revisions: Journal of Sedimentary Research.

Chow, V. T., 1959, Open-Channel Hydraulics: New York, McGraw-Hill, 680 p.

Clark, P. J. and Evans, F. C., 1954, Distance to nearest neighbor as a measure of spatial relationships in populations: Ecology, v. 35, p. 445–453

Colombera, L., Mountney, N. P., and McCaffrey, W. D., 2015, A meta-study of relationships between fluvial channel-body stacking pattern and aggradation rate: implications for sequence stratigraphy: Geology, v. 43, no. 4, p. 283 - 286.

Coney, P. J., 1972, Cordilleran tectonics and North America plate motion: American Journal of Science, v. 272, no. 7, p. 603–628.

Cressie, N.A.C., 1993, Statistics for Spatial Data, (revised edition) Wiley: New York.

DeCelles, P. G. and Coogan, J. C., 2006, Regional structure and kinematic history of the Sevier fold-and-thrust belt, central Utah: Geological Society of America Bulletin, v. 118, no. 7-8, p. 841–864.

Dickinson, W. R., 1974, Plate tectonics and sedimentation, tectonics and sedimentation, in: W. R. Dickinson, eds., Tectonics and Sedimentation: Society of Economic Paleontologists and Mineralogists Special Publication v. 22, p. 1–27.

Diggle, P.J., 2003, Statistical Analysis of Spatial Point Patterns, second edition, Oxford University Press: London.

Dooling, P. R., 2013, Tidal facies, stratigraphic architecture, and along-strike variability of a high energy, transgressive shoreline, Late Cretaceous, Kaiparowits Plateau, Southern Utah, Master's thesis, University of Utah, Salt Lake City, 135 p.

Eaton, J. G., 1991, Biostratigraphic framework for the upper Cretaceous rocks of the Kaiparowits Plateau, southern Utah, in: J. D. Nations and J. G. Eaton, eds., Stratigraphy, Depositional Environments, and Sedimentary Tectonics of the Western Margin, Cretaceous Western Interior Seaway: Geological Society of America Special Paper, v. 260, p. 47-64.

Fabuel-Perez, I., Hodgetts, D., and Redfern, J., 2009, A new approach for outcrop characterization and geostatistical analysis of a low-sinuosity fluvial-dominated succession using digital outcrop models: Upper Triassic Oukaimeden Sandstone Formation, central High Atlas, Morocco: AAPG Bulletin, v. 93, no. 6, p. 795–827.

Gallin, W., Johnson, C., Allen, J., and Johnson, C. L., 2010, Fluvial and marginal marine

architecture of the John Henry Member, Straight Cliffs Formation, Kelly Grade of the Kaiparowits Plateau, South-Central Utah: Geology of South-Central Utah, v. 39.

Ganti, V., Chu, Z., Lamb, M. P., Nittrouer, J. A., and Parker, G., 2014, Testing morphodynamic controls on the location and frequency of river avulsions on fans versus deltas: Huanghe (Yellow River), China: Geophysical Research Letters, v. 41, p. 7882–7890.

Gibling, M. R., 2006, Width and thickness of fluvial channel bodies and valley fills in the geological record: a literature compilation and classification: Journal of Sedimentary Research, v. 76, p. 731–770.

Gooley, J. T., 2010, Alluvial architecture and predictive modeling of the Late Cretaceous John Henry Member, Straight Cliffs Formation, Southern Utah, Master's thesis, University of Utah, Salt Lake City, 376 p.

Hajek, E. A., Heller, P. L., & Sheets, B. A., 2010, Significance of channel-belt clustering in alluvial basins: Geology, v. 38, no. 6, p. 535-538.

Hancock, J. M., and Kauffman, E. G., 1979, The great transgressions of the Late Cretaceous: Journal of the Geological Society, v. 136, no. 2, p. 175–186.

Haq, B. U., Hardenbol, J., Vail, P. R., 1987, Chronology of fluctuating sea levels since the Triassic: Science, v. 235, no. 4793, p. 1156–1167.

Heller, P.L. and Paola, C., 1996, Downstream changes in alluvial architecture: an exploration of controls on channel-stacking patterns: Journal of Sedimentary Research, v. 66, p. 297–306.

Hettinger, R.D., McCabe, P. J., and Shanley, K. W., 1993, Detailed facies anatomy of transgressive and highstand systems tracts from the Upper Cretaceous of southern Utah, USA: Chapter 9: Recent Applications of Siliciclastic Sequence Stratigraphy, American Association of Petroleum Geologists Memoir 58: p. 235–257.

Hofmann, M.H., Wroblewski, A., and Boyd, R., 2011, Mechanisms Controlling the Clustering of Fluvial Channels and the Compensational Stacking of Cluster Belts: Journal of Sedimentary Research, v. 81, p. 670-685.

Hooke, R.L., and Rohrer, W.L., 1979, Geometry of alluvial fans: effect of discharge and sediment size: Earth Surface Processes and Landforms, v. 4, p. 147–166.

Jerolmack, D.J., and Paola, C., 2007, Complexity in a cellular model of river avulsion: Geomorphology, v. 91, p. 259–270.

Jerolmack, D. J., and J. B. Swenson, 2007, Scaling relationships and evolution of distributary networks on wave-influenced deltas: Geophysical Research Letters, v. 34, no. 23.

Jones, L. S. and Schumm, S. A., 1999, Causes of avulsion: an overview, in: N. D. Smith and J. Rogers, eds., Fluvial Sedimentology VI: Blackwell Publishing Ltd., Oxford, UK.

Jordan, T. E., 1981, Thrust loads and foreland basin evolution, Cretaceous, Western United States: AAPG Bulletin, no. 12, p. 2506–2520.

Kauffman, E. G., 1977, Geological and biological overview: Western Interior Cretaceous Basin: The Mountain Geologist, v. 14, no. 3-4, p. 75–99.

Kleinhans, M. G., 2010, Sorting out river channel patterns: Progress in Physical Geography, v. 34, no. 3, p. 287-326.

Lawton, T. F., Pollock, S. L., and Robinson, R. A. J., 2003, Integrating sandstone petrology and nonmarine sequence stratigraphy: application to the late Cretaceous fluvial systems of southwestern Utah, U.S.A.: Journal of Sedimentary Research, v. 73, no. 3, p. 389-406.

Leeder, M. R., 1978, A quantitative stratigraphic model for alluvium, with special reference to channel deposit density and interconnectedness, in: A. D. Miall, eds., Fluvial Sedimentology: Canadian Society of Petroleum Geologists Memoir 5, p. 587–596

Little, W. W., 1997, Tectonic and eustatic controls on cyclical fluvial patterns, Upper Cretaceous strata of the Kaiparowits Basin, Utah, in: L. M. Hill, eds., Learning from the Land: Grand Staircase – Escalante National Monument Science Symposium Proceedings: Salt Lake City: Bureau of Land Management, p. 489–504.

Liu, S., Nummedal, D., Gurnis, M., 2014, Dynamic versus flexural controls of Late Cretaceous Western Interior Basin, USA: Earth and Planetary Science Letters, v. 389, p. 221–229.

Lyons, W.J., 2004, Quantifying channelized submarine depositional systems from bed to basin scale, Ph.D. thesis, Cambridge, Massachusetts Institute of Technology, 252 p.

Mackey, S.D. and Bridge, J.S., 1995, Three-dimensional model of alluvial stratigraphy: theory and application: Journal of Sedimentary Research, v. 65, p. 7–31.

Miall, A. D., 2014, Fluvial Depositional Systems: Cham, Springer International Publishing: p. 332.

Miller, K. G., Kominz, M. A., Browning, J. V., Wright, J. D., Mountain, G. S., Katz, M. E., Sugarman, P. J., Cramer, B. S., Christie-Blick, N., Pekar, S. F., 2005, The Phanerozoic record of global sea-level change: Science, v. 310, no. 5752, p. 1293–8.

Mohrig, D., Heller, P.L., Paola, C., and Lyons, W.J., 2000, Interpreting avulsion process from ancient alluvial sequences: Guadalope-Matarranya (northern Spain) and Wasatch Formation (western Colorado): Geological Society of America Bulletin, v. 112, p. 1787–1803.

Morozova, G.S. and Smith, N.D., 2000, Holocene avulsion styles and sedimentation patterns of the Saskatchewan River, Cumberland Marshes, Canada: Sed. Geol., v. 130, p. 81–105

Mulhern, J. S., Johnson, C. L., Stright, L.E., Chentnik, B. M., 2014, Implications of an expanded section and delta deposits in the Cretaceous Straight Cliffs Formation in the northern Kaiparowits Plateau, southern Utah, USA, Abstracts with Program: AAPG Annual Convention and Exhibition 2014, Houston, TX.

Peterson, F.E., 1969a, Cretaceous sedimentation and tectonism in the southeastern Kaiparowits region, Utah: USGS Open-File Report 1314, Sequence Stratigraphy and Basin Evolution of the Kaiparowits Plateau: p. 259.

Peterson, F.E., 1969b, Four new members of the Upper Cretaceous Straight Cliffs Formation in the south- eastern Kaiparowits region, Kane County, Utah: USGS Bulletin 1274-J, p. J1–J28.

Pettinga, L., 2012, Alluvial architecture and paleomorphodynamics of the Upper Cretaceous John Henry Member, Straight Cliffs Formation, Utah, Master's Thesis: University Utah, Department of Geology and Geophysics, Salt Lake City, UT, USA.

Postma, G., 2014, Generic autogenic behaviour in fluvial systems, in: A. W. Martinius, R. Ravnås, J. A. Howell, R. J. Steel and J. P. Wonham, eds., From Depositional Systems to Sedimentary Successions on the Norwegian Continental Margin: John Wiley & Sons, Ltd, Chichester, UK.

Rannie, W.F., Thorleifson, L.H., and Teller, J.T., 1989, Holocene evolution and paleohydrology of the Portage la Praire alluvial fan: Canadian Journal of Earth Sciences, v. 26, p. 1834–1841.

Richards, K., Chandra, S., and Friend, P., 1993, Avulsive channel systems: characteristics and examples: Geological Society of London, p. 195–203.

Ripley, B.D., 1976, The second-order analysis of stationary point processes: Journal of

Applied Probability, v. 13, p. 255-266.

Ripley, B.D., 1979, Tests of 'randomness' for spatial point patterns: Journal of the Royal Statistical Society, Series B 41, p. 368–374

Ripley, B.D., 1996, Pattern Recognition and Neural Networks, Cambridge University Press: Cambridge, England.

Sakoe, H. and Chiba, S., 1978, Dynamic programming optimization for spoken word recognition: IEEE Trans. Acoustics, Speech, Signal Proc., ASSP-26, no. 1, p. 43-49.

Shanley, K. W., 1991, Sequence stratigraphic relationships and facies architecture of Turonian-Campanian strata, Kaiparowits Plateau, south-central Utah: Colorado School of Mines, p. 390.

Shanley, K. W., and McCabe, P. J., 1991, Predicting facies architecture through sequence stratigraphy - an example from the Kaiparowits Plateau, Utah: Geology, v. 19, p. 742-745.

Shanley, K. W., and McCabe, P. J., 1993, Alluvial architecture in a sequence stratigraphic framework: a case history from the Upper Cretaceous of southern Utah, USA: Special Publication 15 of the International Association of Sedimentologists, p. 21-56.

Shanley, K., and McCabe, P. J., 1994, Perspectives on the sequence stratigraphy of continental strata: AAPG bulletin, v. 4, no. 4, p. 544–568.

Shanley, K. W., and McCabe, P. J., 1995, Sequence stratigraphy of Turonian- Santonian strata, Kaiparowits Plateau, southern Utah, USA: implications for regional correlation and foreland basin evolution: American Association of Petroleum Geologists Memoir 64: p. 103-136.

Shanley, K. W., McCabe, P. J., Hettinger, R., 1992, Tidal influence in Cretaceous fluvial strata from Utah, USA: a key to sequence stratigraphic interpretation: Sedimentology, v. 39, no. 5, p. 905–930.

Smith, T.E., 2014, Notebook on spatial data analysis [online] http://www.seas.upenn.edu/~ese502/#notebook

Straub, K.M., Paola, C., Mohrig, D., Wolinsky, M.A., and George, T., 2009, Compensational stacking of channelized sedimentary deposits: Journal of Sedimentary Research, v. 79, p. 673–688.

Strong, N., Sheets, B. A., Hickson, T. A., and Paola, C., 2005, A mass-balance framework for quantifying downstream changes in fluvial architecture, in: M.

Blum, et al., eds., Fluvial Sedimentology VII: International Association of Sedimentologists, pp. 243–253,.

Szwarc, T. S., Johnson, C. L., Stright, L. E., McFarlane, C. M., 2014, Interactions between axial and transverse drainage systems in the Late Cretaceous Cordilleran foreland basin: evidence from detrital zircons in the Straight Cliffs Formation, southern Utah, USA: Geological Society of America Bulletin.

Tornqvist, T.E., 1994, Middle and late Holocene avulsion history of the River Rhine (Rhine-Meuse Delta, The Netherlands): Geology, v. 22, p. 711–714.

Turner, A., 2014, Temporal variability in fluvial deposition and the implications for static reservoir connectivity: John Henry Member, Straight Cliffs Formation, Master's thesis, University of Utah, Salt Lake City, USA.

van Gelder, A., van den Berg, J.H., Cheng, G., and Xue, C., 1994, Overbank and channel fill deposits of the modern Yellow River delta: Sedimentary Geology, v. 90, p. 293–305.

Wells, N. A., and Dorr, J. A., Jr., 1987, Shifting of the Kosi River, northern India: Geology, v. 15, p. 204–207.

Wang Y., Straub, K., and Hajek, E., 2011, Scale dependent compensational stacking: an estimate of autogenic timescales in sedimentary deposits: Geology, v. 39, p. 811-814.

Wright, V.P., and Marriott, S.B., 1993, The sequence stratigraphy of fluvial depositional systems: the role of floodplain sediment storage: Sedimentary Geology, v. 86, p. 203–210.